FINAL Report

Federal Agency and Organization: DOE EERE – Geothermal Technologies Program

Recipient Organization: Colorado school of Mines
DUNS Number: 010628170
Recipient Address: Department of Geophysics
1500 Illinois St.
Golden, Colorado 80401

Award Number: DE-EE0005513
Project Title: Time-lapse Joint Inversion of Geophysical Data and its Applications to Geothermal Prospecting - GEODE
Project Period: 01/01/2012-12/31/2015

Principal Investigator: André Revil
andre.revil@univ-smb.fr

Project Partners: Colorado School of Mines: A. Revil
ORMAT Nevada Inc (Ezra Zemach)

DOE Project Team: DOE Contracting Officer – Genevieve Wozniak
DOE Project Officer – Weathers, Michael [Michael.Weathers@ee.doe.gov]
Project Monitor – Sara Emmons (Sara.emmons@ee.doe.gov)

Outline

1. Phase 1

Our project was entitled " Time-lapse Joint Inversion of Geophysical Data and its Application to Geothermal Prospecting. Grant/Cooperative Agreement DE-EE0005513. ". The objectives of this project were to develop new algorithms to decrease the cost of drilling for geothermal targets during the exploration phase of a hydrothermal field and to improve the monitoring of a geothermal field to better understand its plumbing system and keep the resource renewable (i.e., not overtaping the existing heat sources). During Phase 1, we have developed a new set of algorithms to perform the inversion of geophysical data including DC resistivity, gravity, EM, and seismic data. ORMAT database has been used to decide of a strategy for the measurements at Jersey Valley (ORMAT has completed their obligations in terms of cost shares). Regarding the EM equipment, it has been purchased and we have done the preliminary tests (Metronix equipment).

An image-guided approach was developed to combine electromagnetic and seismic data. This approach has been validated through simulations with synthetic and a shallow application with DC resistivity data and ground penetrating radar (GPR). These completely new methodology was published in Geophysical Journal International (Zhou et al., 2014) and is a way to merge prior geological information with geophysical data to improve the resolution of the geophysical tomograms. A total of 8 peer-reviewed papers have been published from the work done Phase 1 and several softwares have been released in the public domain.

1.1. Datasets

Prior data collected both at Jersey Valley, Nevada, and at an analog volcano sites in Italy are gathered, assessed, and edited. This provided the initial data sets to begin building the inversion routines. The field work at Stromboli was done in January 2012 at no cost for DOE." An impressive database regarding 3D resistivity tomography and gravity data were obtained in collaboration with Anthony Finizola (university of la Réunion) and Niklas Linde (University of Lausanne, Switzerland). Figure 1.1 is showing some of the results of the inversion of the gravity data for which we used a very precise digital elevation map and bathymetry (Figure 1.2). The resistivity data shown in Figure 1.3. A 3D resistivity tomogram has been produce and we are presently finishing a paper for Nature Geosciences. In addition to resistivity and gravity data, we also gathered self-potential, temperature, and CO_2 flux data that were used for a 3D model of ground water flow circulations.

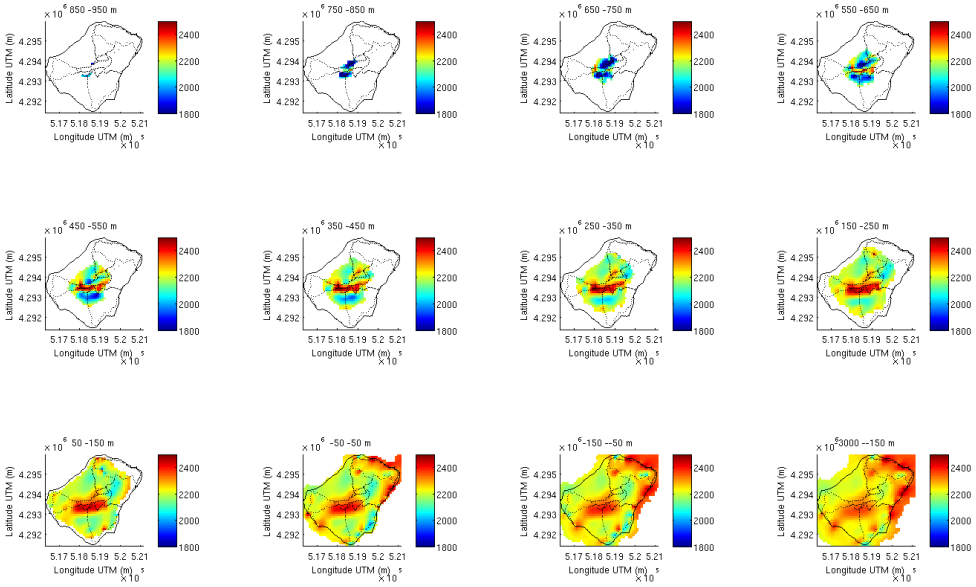

Figure 1.1. Inversion of the density of Stromboli (Italy) (Niklas Linde, data gathered during the field work done in January 2012).

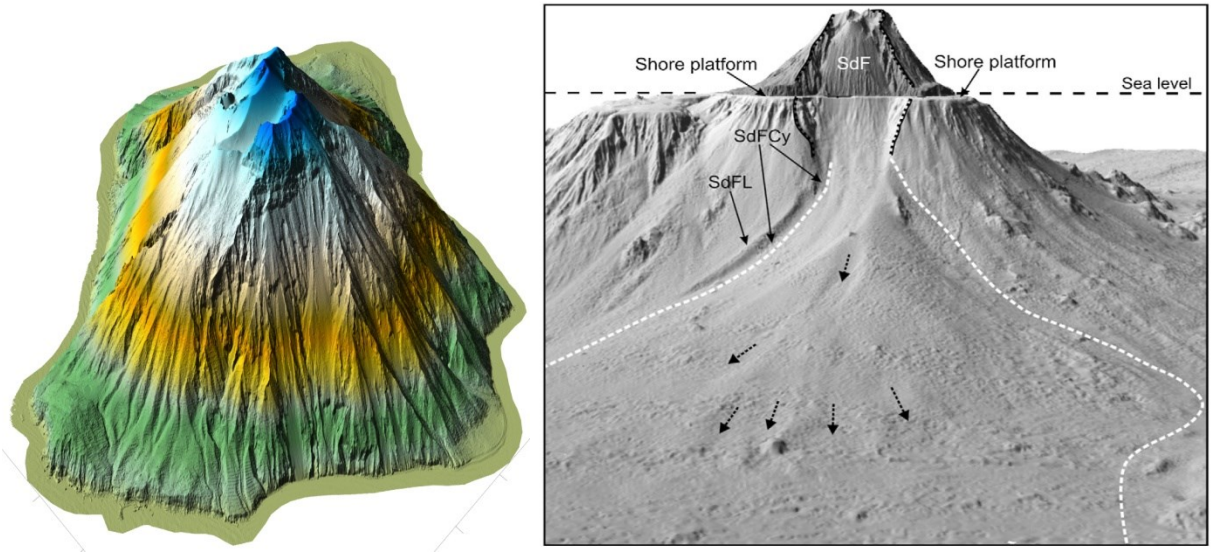

Figure 1.2. In order to invert the gravity data we use a very precise digital elevation map with a precision of 1m. We use also a very precise bathymetry and the data were detrended from the original gravity component.

A second part of this project was to couple ground water flow to the computation of the self-potential signal in a geothermal field. We have developed therefore some modeling with Comsol Multiphysics 3.4 of multiphase flow in geothermal systems associated with volcanoes to predict the distribution of the self-potential signals and the distribution of resistivity as shown for instance in Figure 4 (see Byrdina et al., 2013). The model includes the occurrence of self-potential signals associated with the infiltration of the rainwater, forced and free convection.

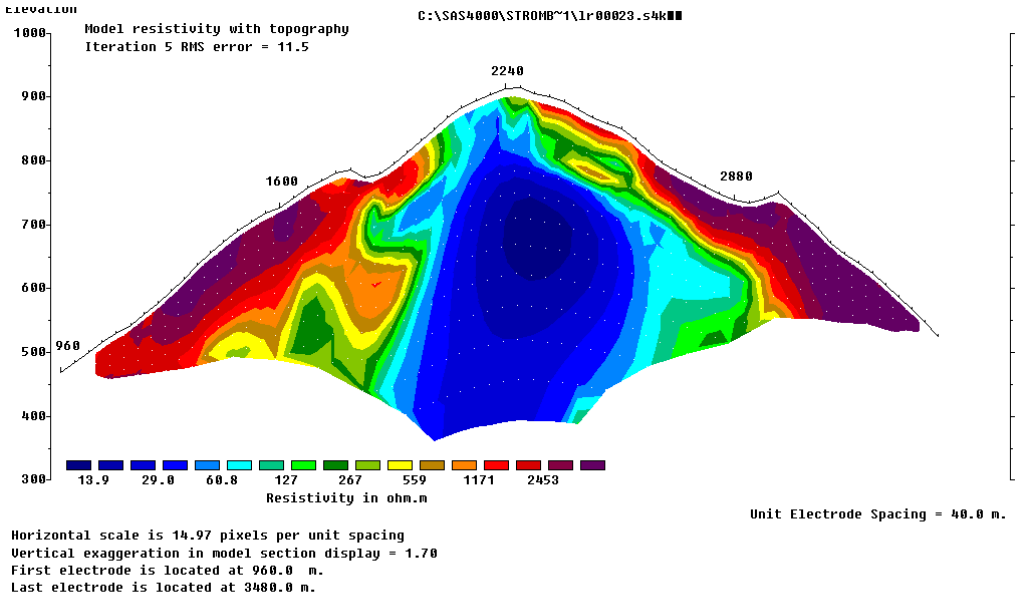

Figure 1.3. Example of large scale resistivity profiles of Stromboli volcano (Data gathered in January 2012, here inverted with RES2DINV).

In Byrdina et al. (EPSL, 2013), we studied the influence of the regional topography on the hydrothermal fluid flow pattern in the subsurface of a volcanic complex (Figure 1.4). We discussed how the advective transfer of heat from a magmatic source is controlled by the regional topography for different values of the averaged permeability. We used a 2-D numerical model of coupled mass and heat transport and new data sets acquired at Ticsani and Ubinas, two andesitic volcanoes in southern Peru which have typical topography, justifying this approach. A remarkable feature of these hydrothermal systems is their remote position not centered on the top of the edifice. It is evidenced by numerous hot springs located in more than 10 km distance from the top of each edifice. Upwelling of thermal water is also inferred from a positive self-potential anomaly at the summit of the both volcanoes, and by ground temperatures up to 37 degree C observed at Ticsani. Our model results suggest that the regional topographic gradient is able to significantly divert the thermal water flow and can lead to an asymmetric emplacement of the hydrothermal system even considering a homogeneous permeability of the edifice. Inside the

thermal flow, the hydraulic conductivity increases with the decrease of temperature-related viscosity, focusing the flow towards the surface and creating a hydrothermal zone at a large lateral distance from the heat source. The location and temperature of the hot springs together with the water table position given by self-potential data can be used to constrain the average permeability of the edifice, a key parameter influencing fluid flow and associated advective heat transfer in the direction opposite to the regional topographic gradient. Our study allows explaining the emplacement of the hydrothermal systems at volcanoes with asymmetric edifices or even the absence of a shallow hydrothermal system. These results can be generalized to the study of non-volcanic hydrothermal systems with a clear interest to DOE targets..

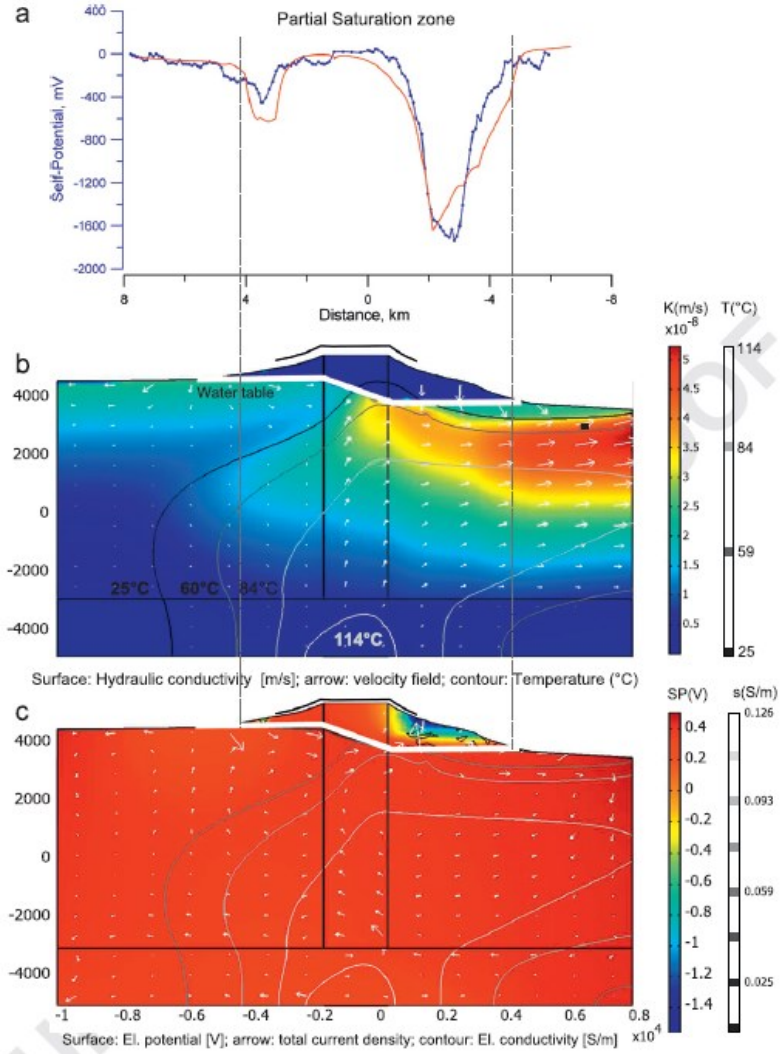

Figure 1.4. Finite element computation of ground water flow in the geothermal system associated with a volcano and the associated self-potential field at the ground surface, which is compared to the measured one.

1.2. Formulation of Joint Inversion Model

We have developed several algorithms to do the inversion of geophysical data and to use different source of information in the inverse problem of the geophysical data to reduce the non-uniqueness of the inverse problem. In the deterministic algorithms we have developed, we can use either a petrophysical-based joint inversion or a cross-gradient-based joint inversion. The idea of the cross-gradient approach is discussed in Figure 1.5.

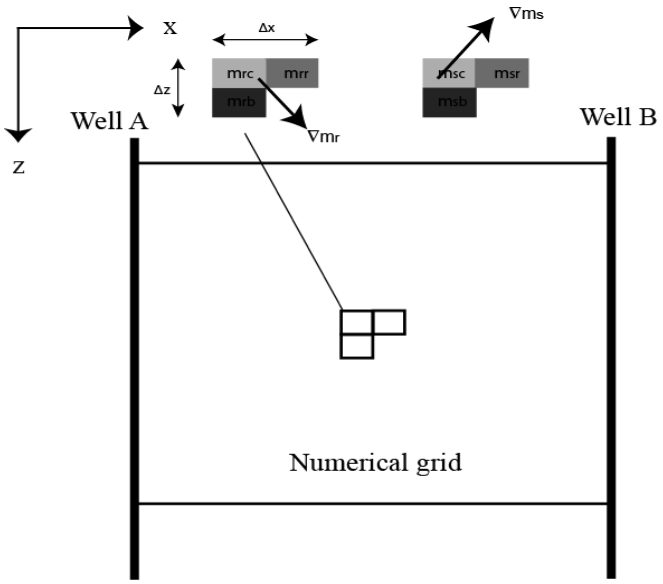

Figure 1.5. A 2.5 D grid used to model the resistivity and velocity of subsurface (*y* corresponds to the strike direction). The cross-gradient is defined with a three cell grid, at each position. The basic idea is that the target is characterized by a gradient in the physical properties along the same contours (in 2.5D) or surfaces (in 3D).

A paper was published in Computers & Geosciences regarding the publication of our resistivity code (Karaoulis M., A. Revil, D.D., Werkema, P. Tsourlos, , and B.J. Minsley, IP4DI SOFTWARE: A 2D/3D time lapse tomographic algorithm for DC resistivity, induced polarization, and frequency-domain induced polarization data, Computers and Geosciences, 2012). This paper was aligned with our initial goals to develop open-code softwares in this DOE project that is accessible to the community. One paper for the joint inversion was published in Geophysics: Karaoulis et al. (2012) (see reference list). A second paper was published in Computers & Geosciences (Soueid Ahmed, A., A. Jardani, A. Revil, and J.P. Dupont, SP2DINV: A 2D forward and inverse code for self-potential problems, Computers & Geosciences, 2012). The goal of this second paper is to release our self-potential code for geothermal applications to the community. This has been successful since we were approaches several times by researchers applying our codes to geothermal targets.

A new methodology was also developed to perform time lapse geophysical data in a Bayesian framework using a Gauss-Newton approach but incorporating some of the underlying

physics of reactive flow or two-phase flow in the inversion of the geophysical data. An example is given in Figure 1.6. This new approach is described in a manuscript published in Geophysical Journal International (Zhang et al., 2014).

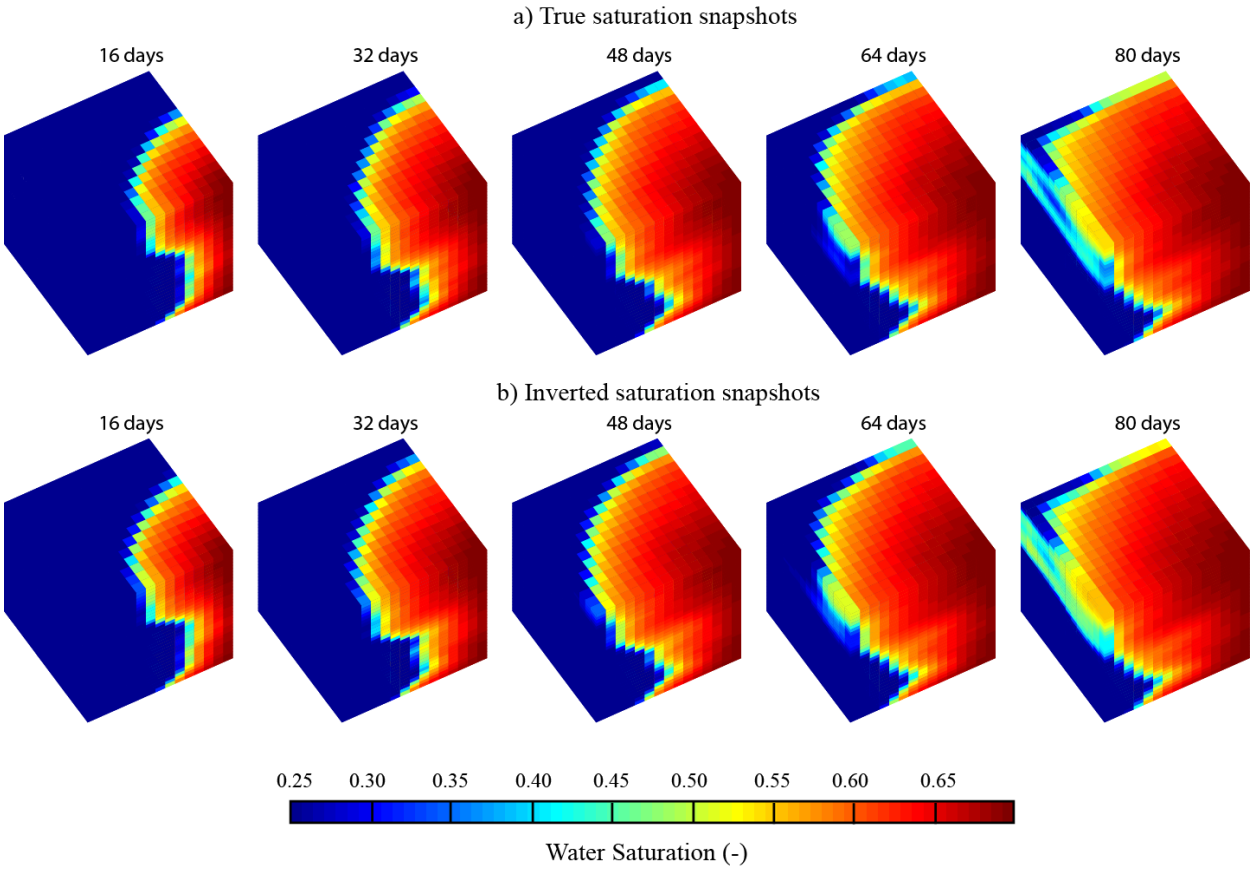

Figure 1.6. Comparison between the true saturation distribution and the inverted saturation distribution between two wells. Note that the position of the front is pretty well recovered through the inversion of the cross-well resistivity data. It is impossible to determine the position of this front with a conventional Gauss-Newton approach (from Zhang et al., Geophysical Journal international, 2014).

The migration of hydrothermal fluids can also influence self-potential, gravity, and electrical resistivity, since these quantities depend on fluid flow pattern, temperature, and phase saturation. To understand the dynamics between the change in the geophysical observables and the dynamics of a hydrothermal system, we first need to be able to simulate the evolution of the hydrothermal system and then compute the observables in a post-processed calculation. In Figure 1.7, a hydrothermal system is fed by fluids of magmatic origin and an unrest phase is simulated. Using a large scale simulation (10 km wide and 1.5 km deep), we can quantify and compare the evolution of the considered observable parameters after a period of increased hydrothermal activity. The simulations was performed with TOUGH2/EOS2.

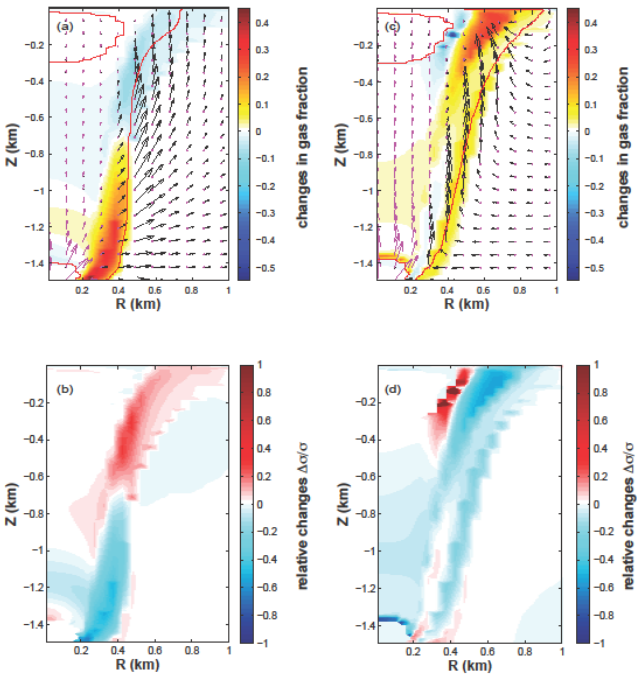

Figure 1.7. Change in gas content and electrical DC electrical conductivity associated with the activity of a hydrothermal system. Simulations performed with TOUGH2/EOS2.

Our 4D inversion algorithm for gravity was finished in Phase 1 of our DOE project. It has been benchmarked on synthetic data obtained with TOUGH2 (Figure 1.7). The 4D inversion algorithm for gravity is finished. It has been benchmarked on synthetic data obtained through the simulator TOUGH2. Figures 1.8 and 1.9 are showing some of the results of the inversion for a synthetic case study. The joint inversion code is also finished and has been benchmarked on simple geometries.

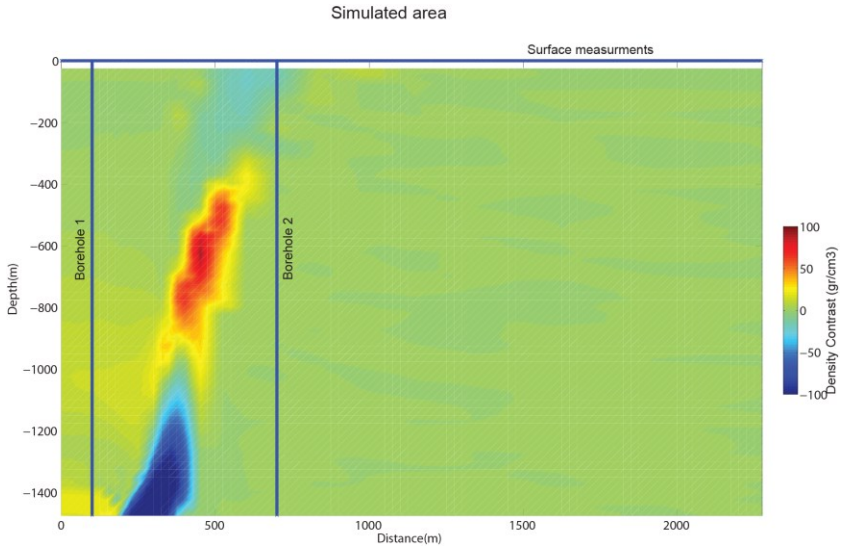

Figure 1.8. Cross-well gravity configuration. Two boreholes at 100 and 700 meters, measurements every 2 m. Surface measurements every 2 m. The colors represents the change in the density contrast of a hydrothermal system with a change in the temperature.

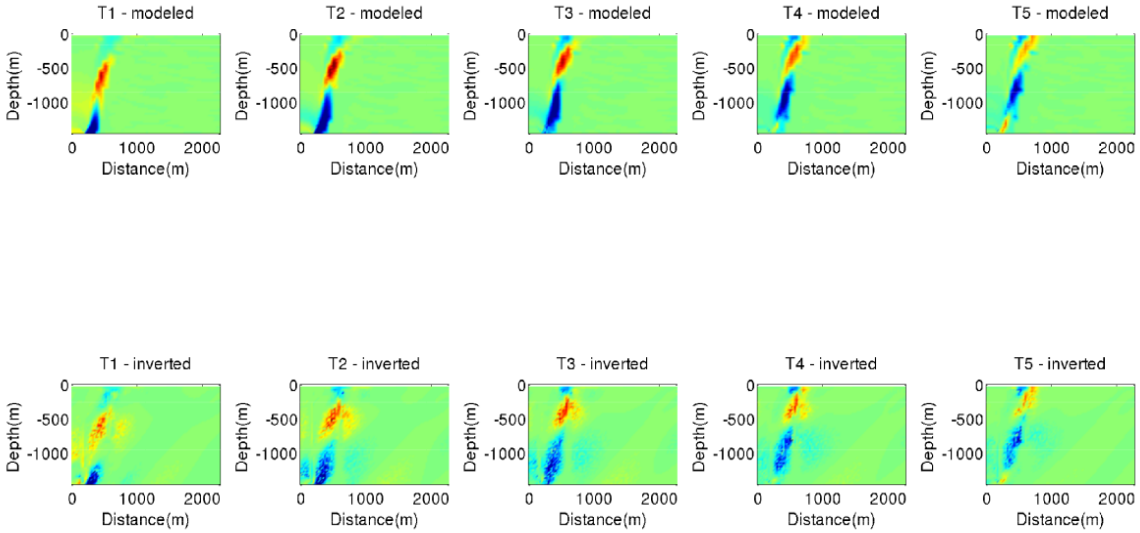

Figure 1.9. Time-lapse inversion of a 5 snapshot including gravity and well data.

We also wrote a paper on cross-well inversion of electromagnetic data including the effect of induced polarization. This paper was published in Geophysics (MacLennan, K., M. Karaoulis, and A. Revil, Geophysics, 2014). We have also developed new codes for the joint inversion of self-potential and resistivity data. In order to test this code, we have been working on a coal seam fire at Marshall, Colorado, which provides a heat source in the near ground surface (depth of 10-20 m). We have used this opportunity to understand through lab and field measurements how a heat source can generate a self-potential anomaly through the thermoelectric effect and a resistivity anomaly (Figures 1.10 and 1.11). A time lapse joint inversion algorithm was developed and applied to this case study (Figure 1.12). A paper was published in Geophysics as a result of this work (Revil et al., 2013) and a second one in Interntional Journal of coal geology (Karaoulis et al., 2014)..

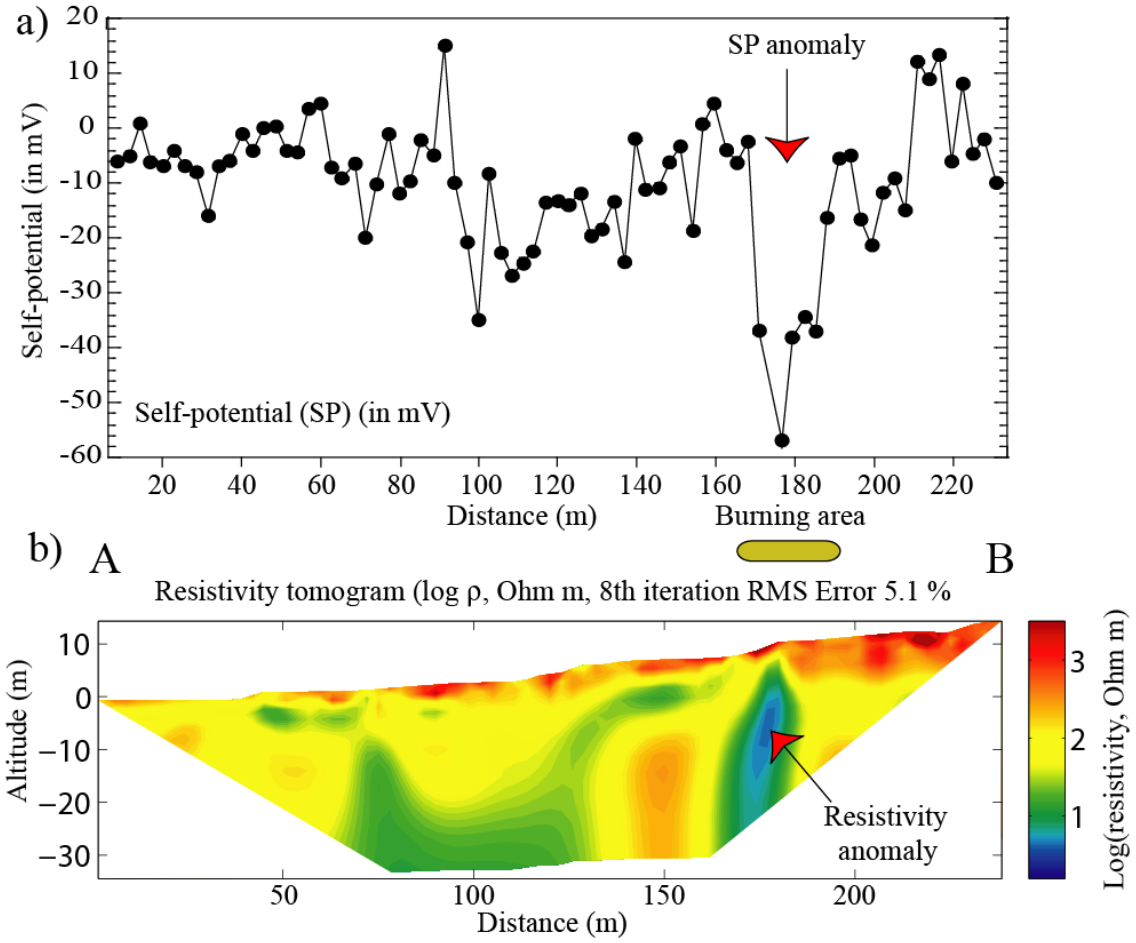

Figure 1.10. Self-potential data (79 stations) and electrical resistivity tomogram (714 apparent resistivity data, Wenner-α, 79 electrodes). The inversion of the self-potential data was done by accounting for the resistivity distribution. Note the low resistivity anomaly (2 Ohm m) below the negative self-potential anomaly (-5 mV). Both the self-potential and resistivity anomalies are related to the presence of a shallow heat source and could be used to determine the best "sweet spots" to drill in geothermal systems for DOE targets. Even of the depth of the target used for this depth is very shallow, there is no issues in using electrical resistivity tomography and self-potential tomography down to 4 km.

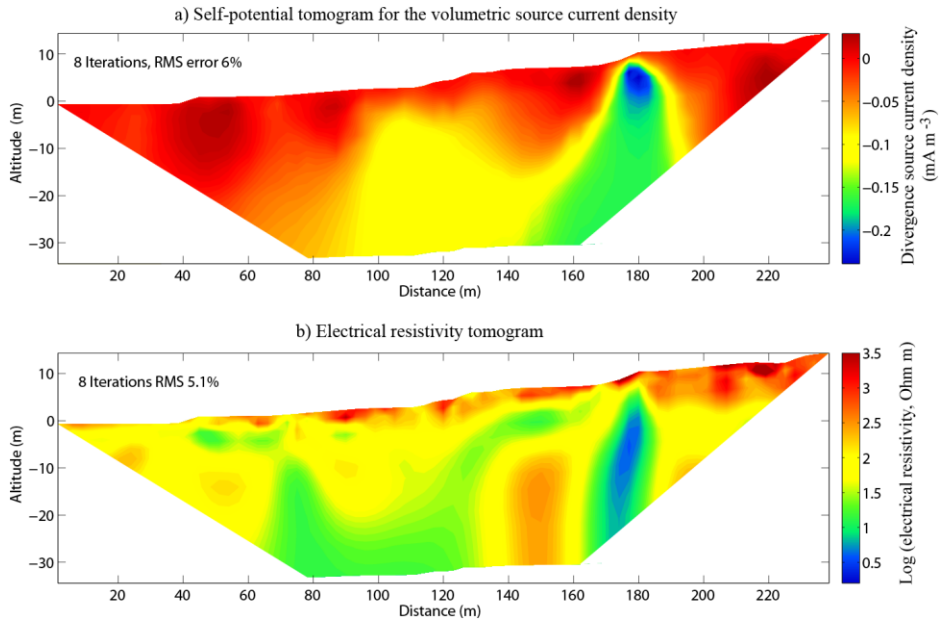

Figure 1.11. Joint inversion results of the self-potential and resistivity field data. **a.** Self-potential tomogram for the volumetric current density (in mA m^{-3}). **b.** Electrical resistivity tomogram (in Ohm m). Note that the source current density and the low resistivity anomaly are located more or less in the same area but the self-potential source seems shallower.

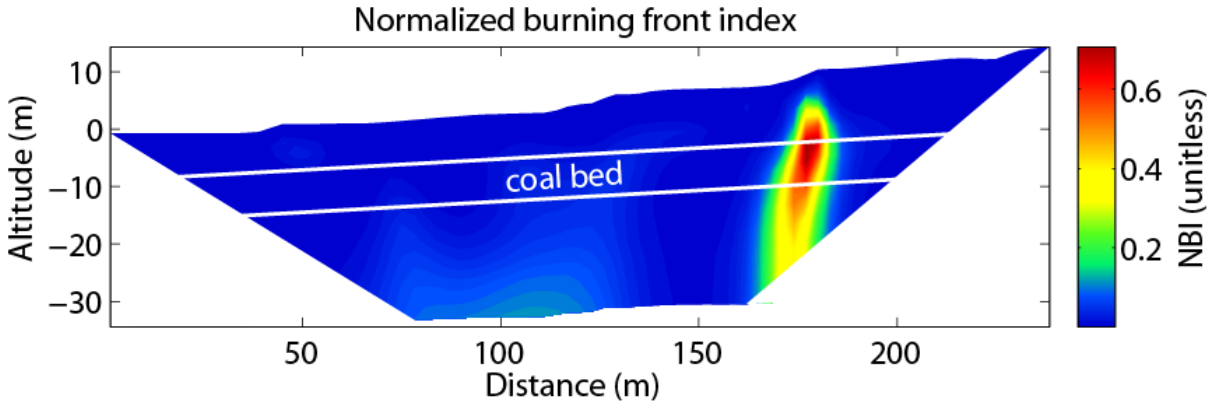

Figure 1.12. Determination of the Normalized Burning front Index (NBI) from the jointly inverted self-potential and DC resistivity data. High values corresponds to a high probability zone in terms of recovering the position of the heat source associated with the burning front in the coal bed. This type of joint inversion can be applied to geothermal systems as well.

We have also developed a new image-guided inversion which is described in the paper Zhou et al. (2014, published in Geophysical Journal International).

1.3. Database

ORMAT has assembled a database and the geology is discussed with Peter Drakos, the geologist of ORMAT. The database included the data collected over the last 4 years at Jersey Valley. This database includes: 1) Shallow gradient-hole drilling (drilling history, mud log, cutting analysis), 2) Ground magnetic survey, 3) Resistivity survey (IP), 4) Soil mercury geochemistry, 5) Radon-thoron soil gas survey, 6) Water chemistry, 7) Detailed geologic mapping, 8) Gravity survey, 9) 3 slim-holes data (drilling history, mud log, cutting analysis), 8) 9 full-sized wells (drilling history, mud log, cutting analysis), 9) Well-testing (flow/injection), 10) Conceptual reservoir modeling, 11) Tracers test, 12) Leapfrog 3D structural model, and 13) GIS database. This database has been used to organize a 3D conceptual system of the geology and plumbing system of Jersey Valley (e.g., Figure 1.13).

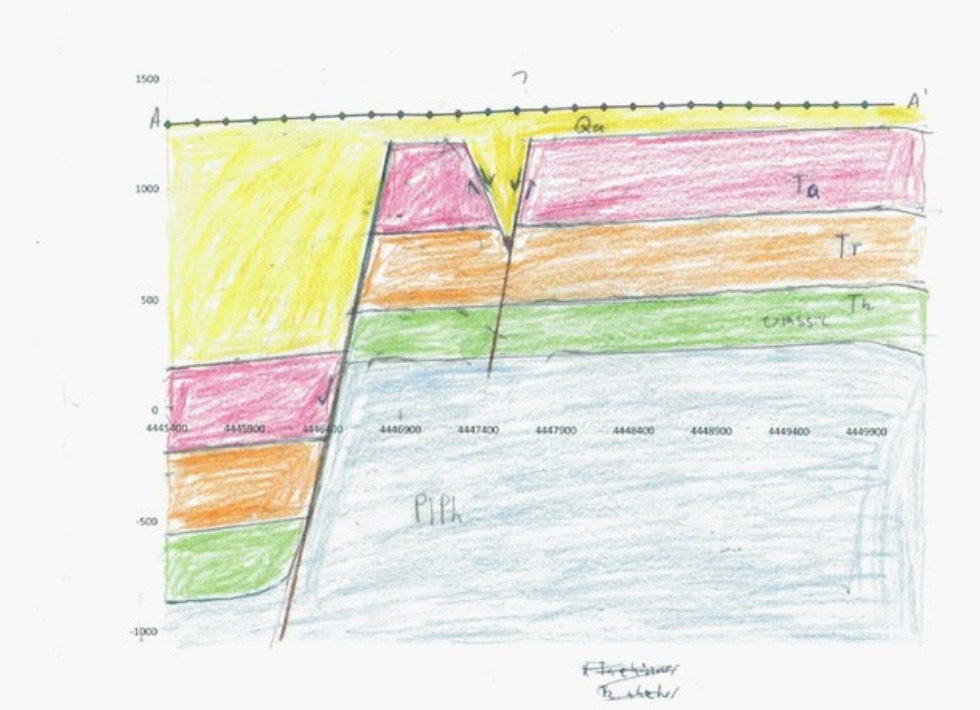

Figure 1.13. An example of cross-Section inferred from the database build by ORMAT.

1.4. Rock Samples Gathered from Jersey Valley

We have obtained the core samples in February 2013 (see Figure 1.14 during our last visit at Jersey Valley). We have started the measurements of the following properties: complex resistivity, density, porosity, permeability and ultrasonic compressional and shear velocities. Table 1 below reports the porosity and density data.

Figure 1.14. Core samples accessed from Jersey Valley.

Table 1. Porosity and grain density of the core samples

Well depth	Total volume	Pore Volume	Porosity	Dry density	Saturated density	Grain density
514.2-514.7	23.7414418	0.89273728	0.03760249	2.518802375	2.556149166	2.617216216
523.0-523.6	28.67834609	3.809236139	0.13282621	2.283023335	2.414946331	2.632717193
618.6-619	40.48194389	0.933850181	0.02306831	2.571763853	2.594675303	2.632490981
808.6 - 809	14.52543966	1.218284333	0.08387246	2.392010213	2.475312338	2.611001311
1813.4-1813.9	6.13840784	0.168646798	0.02747403	2.626495407	2.653782613	2.700694364
2057.2-2057.7	5.487313733	0.39770439	0.07247706	2.493023119	2.565007339	2.68782908
2637.2-2637.6	5.920257753	0.27184857	0.04591837	2.59152568	2.637131803	2.716251515
2949.7-2950	10.96791516	0.110753121	0.01009792	2.657752142	2.667781395	2.684863679
3812.6-3813	6.36830447	0.0973285	0.01528327	2.630736864	2.645916206	2.671567139
2057.2-2.57.7(2)	6.57806417	0.285273191	0.04336735	2.544314898	2.587387347	2.659657173
1813.4-1813.7(2)	40.55779299	0.559806685	0.01380269	2.656209622	2.669918455	2.693385591

Figure 1.15 is showing some data for the in-phase and quadrature electrical conductivity of a core sample from Jersey Valley. The data shows a strong surface conductivity associated with the alteration of the material.

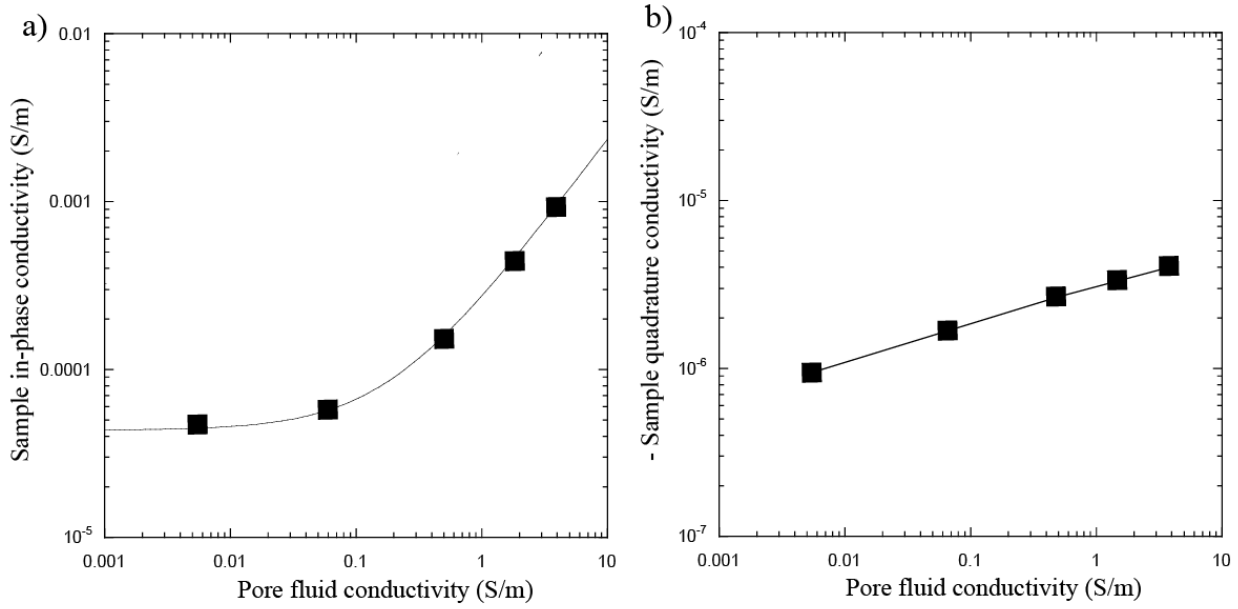

Figure 1.15. In phase and quadrature conductivity for a volcanic core sample from Jersey Valley.

1.5. Use of the Electromagnetic System

We also co-organized with Mike Batzle the field camp at Pagosa Springs (CO) to understand the plumbing system of this hot springs. This allowed us to test the systems of to companies looking at characteristics that were optimizing the following characteristics: (1) Source rental availability, (2) Ease of communication between the EM system and a laptop computer during the acquisition, (3) Maximum number of channel for the electrical field, , (4) friendly user interface DOS/WIN, (5) automatic quality control (QC) during the acquisition, (6) Time synchronisation method (e.g., GPS). An EM equipement was purchased was tested. We just got 24,000 dollars from our dept to buy a second station to increase the sensitivity of our measurements. A test was performed in the Upper Arkansas Valley. We also developed the joint inversion software to perform the joint inversion of the resistivity and seismic data along a profile using an image guided approach. The shallow resistivity was obtained through galvanometric measurements with a 2.5 km cable allowing imaging the resistivity down to 500 m. We also developed an algorithm to perform the joint inversion of the DC resistivity and EM resistivity data.

1.6. Data review and acquisition strategies

A number of papers are also being reviewed regarding the geologic controls of the great basin and its geothermal systems to help us to better understand the system at Jersey Valley.

Also papers that relate geophysics to the geothermal systems in the Great Basin were collected to help in survey planning: specifically the nearby Dixie Valley Geothermal Field has been extensively studied. In addition DEM and satellite imagery were gathered helping in our survey design (see Figure 1.16 to 1.23).

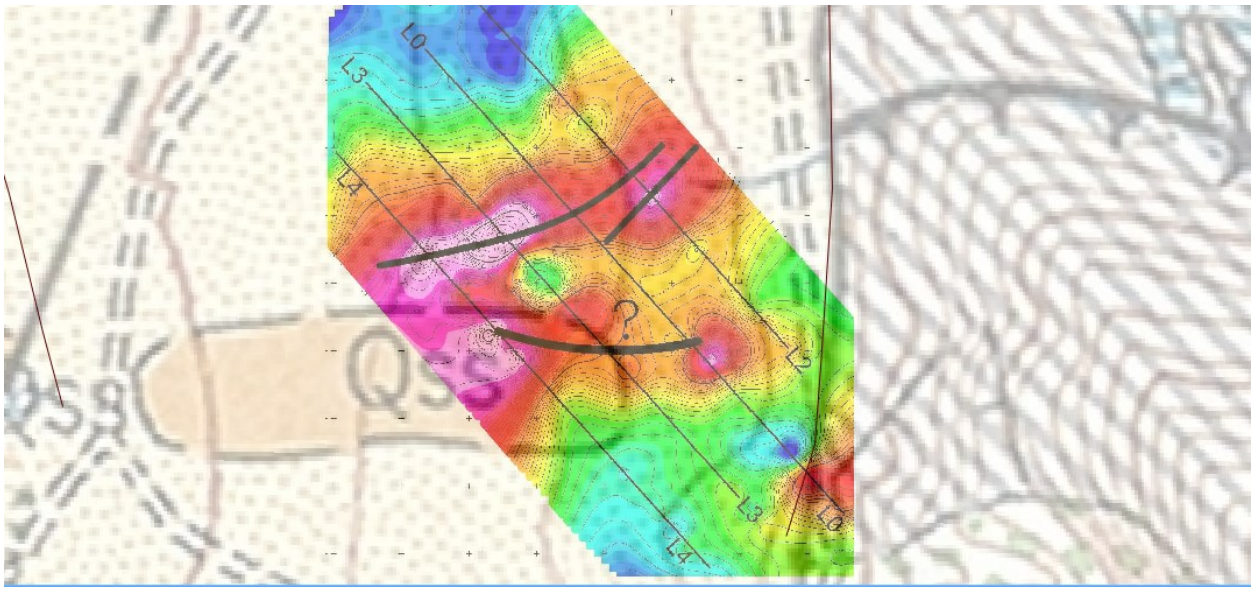

Figure 1.16. IP data over geologic map, data from ORMAT. The North trending fault on east side of survey is from the USGS GIS database. The thick black lines denote IP trends from IP plot. The Northern trend appears to align with the fault to the east and approaches the hot springs.

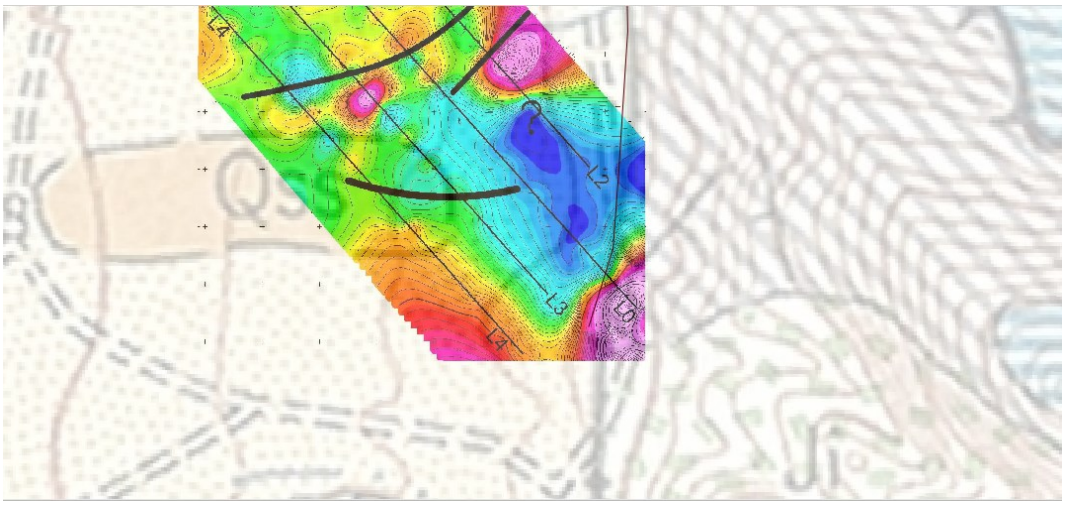

Figure 1.17. Resistivity map laid over geology map, from ORMAT. The North trending fault on east side of survey is from the USGS GIS data, the thick black lines west to east are IP trends from IP plots. They appear to be conductive areas along north trending fault, perhaps denoting a pathway for fluid flow into the system.

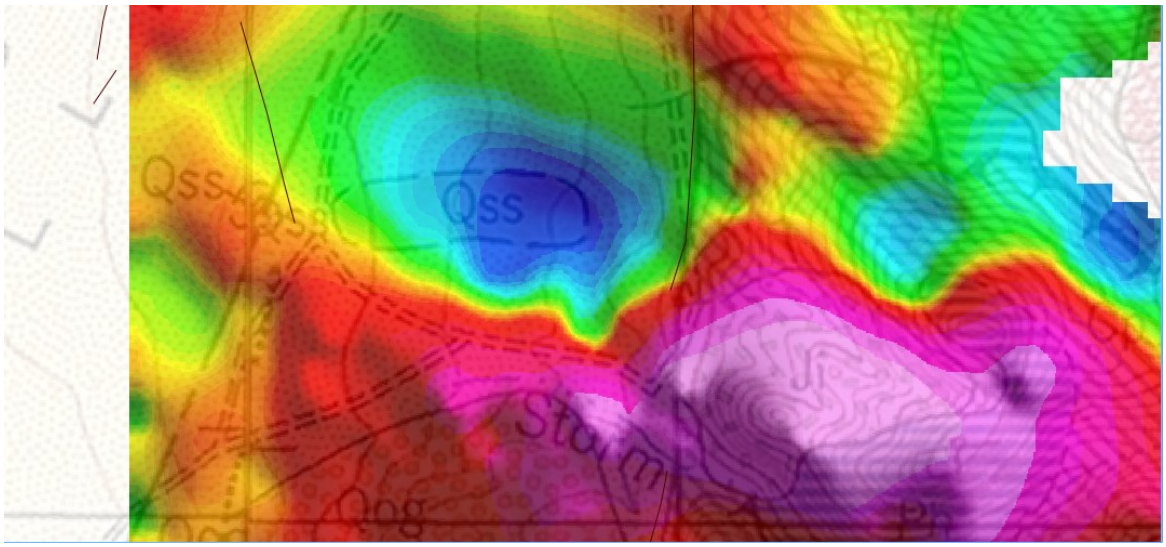

Figure 1.18. Aeromagnetic map over the geological map. Data from ORMAT. The magnetic high to the Southeast is caused from Granodiorite intrusions (Ji) around Jurassic age. Note the magnetic low directly over the hot springs, perhaps caused by thicker sediments associated with the east-west trending fault as interpreted in the leapfrog section.

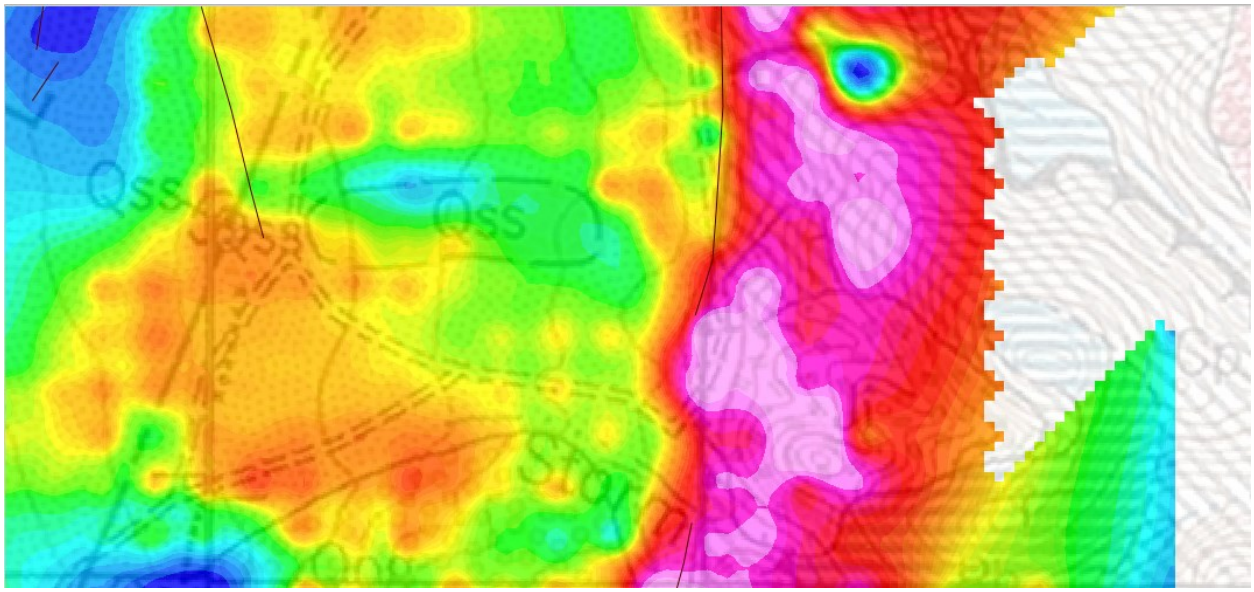

Figure 1.19. First vertical derivative of gravity over geology. Data from ORMAT. Clearly see a high gradient where the north trending fault on the east side of the gravity section is. We can also observe an East West trending high just south of the hot springs related to the interpreted fault.

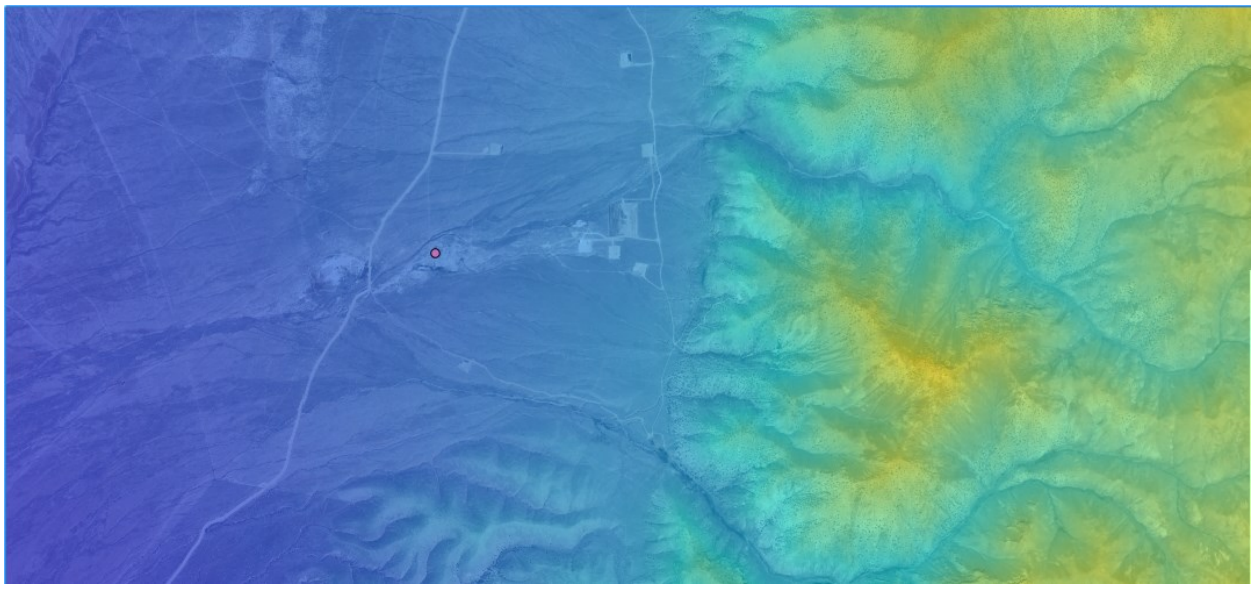

Figure 1.20. DEM overlaying Satellite imagery from USGS. The Satellite imagery allows us to view roads and other detailed features that helped plan our surveys; in addition the DEM allowed prepare our survey planning.

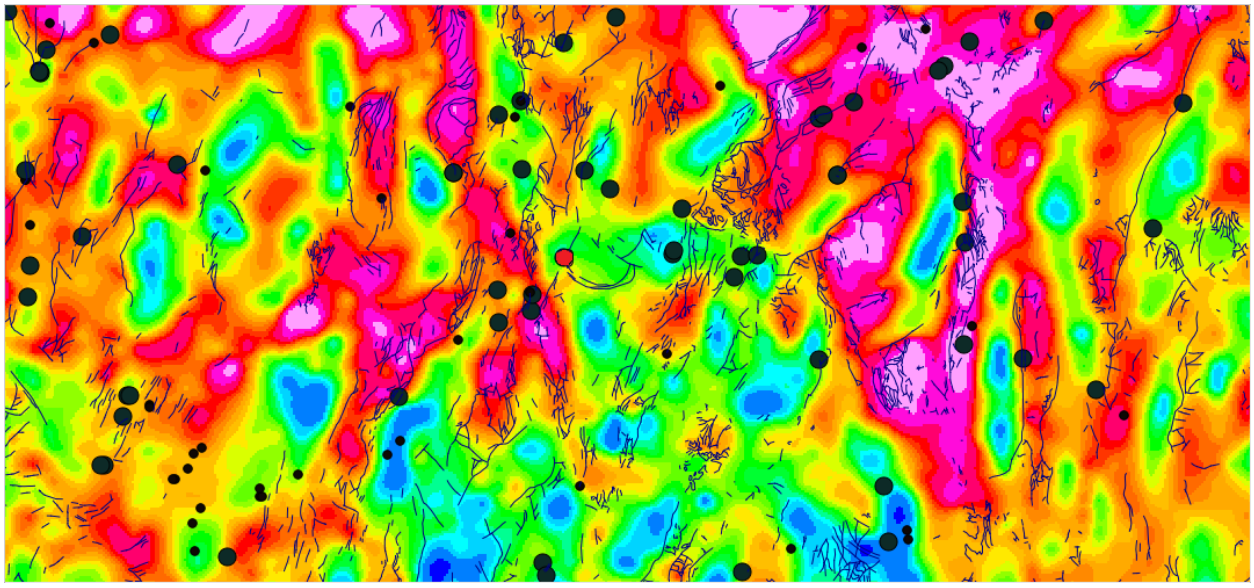

Figure 1.21. Isostatic gravity map with faults lines, from USGS. Dots represent geothermal springs and wells, Jersey Valley hot spring represented by large red dot, from Great Basin Geothermal Center. The hot springs occur in areas of where there is recent faulting and tend to be near areas of high gravity gradients.

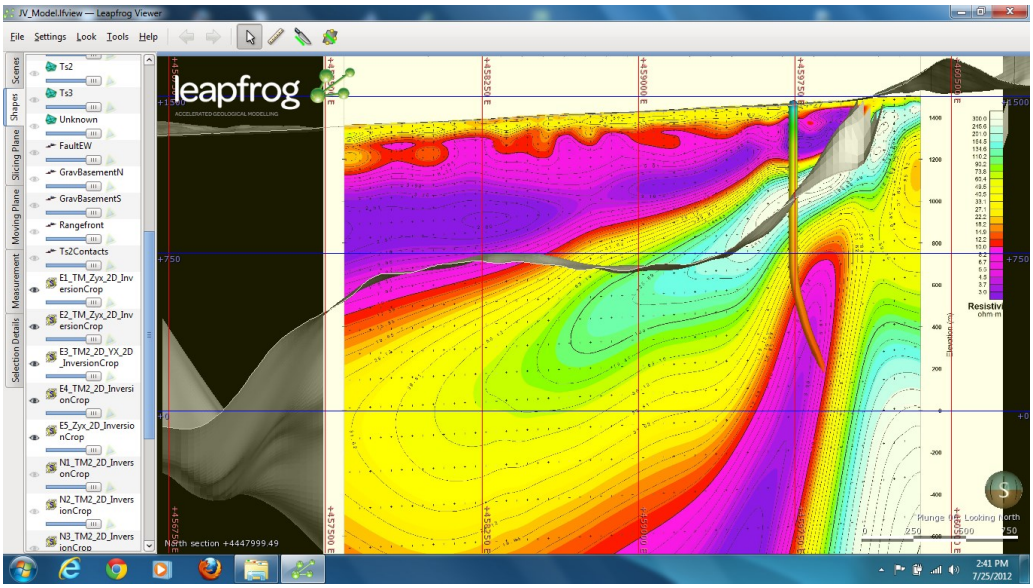

Figure 1.22. Leapfrog section with gravity basement, an MT section, topography, and temperature data from one of the wells. The resistivity is from 3 to 300 Ohm m. The thickness of the section is 1800 m. The well is one of Ormat's wells, the colors are temperature (the lines are isotherms). This well exhibits pretty high temperatures close to the surface.

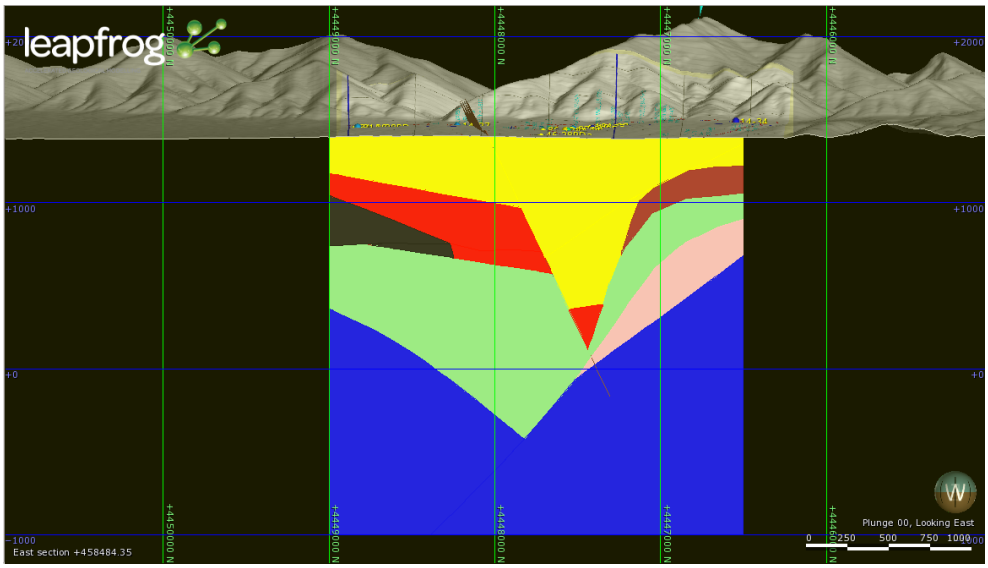

Figure 1.23. Leapfrog model geologic units with topography. An east-west trending normal fault, the blue denotes the Pennsylvanian-Permian Havallah sequence, the yellow denotes Quaternary sediments; the red, maroon, pink denote tertiary rhyolites, and the green color denotes tertiary sediment.

2. Phase 2

The objectives of Phase 2 were: 1. to demonstrate the value of geophysical data in testing the models at Jersey Valley; 2. To show how geophysical data sets based on different physical properties can give information on the Jersey Valley models that is both complimentary and supplementary; 3. To test the currently available models at Jersey Valley. We have clearly achieved objective 1, by showing structures from our models (models 2 and 3 below) are consistent with geophysical data whereas structures. Objective 2 was demonstrated through the use of magnetotelluric and gravity data sets. Magnetotellurics is sensitive to conductivity distribution and gravity to density distribution. Significant displacement of the Valley Fault shown through gravity maps and profile modelling was backed up by the one dimensional magnetotelluric modelling. Objective 3 was demonstrated by the fact that models 2 and 3 are consistent with all the existing data.

2. 1. Dataset and Interpretation tools

An extensive set of information exists within Jersey Valley. In this section, this information is introduced and we discuss what information we have been focused on in this quarter. In addition, we give below a brief description of how and why the information has been used in our project.

2.1.1. Dataset

Jersey Valley is rich with geological and geophysical data sets. Ormat Technologies Inc. has provided, for this DOE project, an extensive data set including geological and geophysical data gathered at Jersey Valley. The data from Ormat includes: 1. Extensive magnetotelluric data sets. 2. Data and reports from two gravity surveys, 3. Data from two magnetic surveys, 4. Maps created from an airborne magnetic survey, 5. Profile and map depth slice maps from an induced polarization survey, 6. Geochemical data, 7. A 1981 thesis on the geology of Jersey Valley, 8. Well operation information and well logs, 9. Detailed geologic mapping within Jersey Valley, 10. Two regional geological maps, 11. A paper describing the geology of the Tobin range, which bounds Jersey Valley to the west (Gonsior and Dilles, 2008), 12. A three dimensional geologic model of the area near Jersey Valley power plant made with Leapfrog®software, v13. A 5 meter resolution digital elevation map, and 14. A conceptual model developed by Hulen and described in Drakos et al. (2011).

The Leapfrog® model and conceptual model is described in more detail below. The Leapfrog® model does an excellent job of combining the well information, geology, and some

geophysics information, but is highly limited in its extent. The conceptual model has a much larger extent, but lacks greatly in its structural details.

In addition to the data provided by Ormat Technologies Inc. members of the Colorado School of Mines Geophysics Department (CSMGP) gathered geophysical data on three different trips. The first trip was performed during spring break of 2013 and consisted of a team of 6 people. Acquired data included two electrical resistivity lines and a number of gravity points. The electrical resistivity lines were gathered in order to better image the resistivity structure of the shallow subsurface within a larger area than the previous surveys. Line locations were placed in the region covered by the pre-existing magnetotelluric and gravity data sets. For this project the electrical resistivity data provided some constraints for the magnetotelluric interpretation and modelling. Gravity data from this survey was concentrated to the west of the previous surveys in order to get better coverage over possible areas of structural interest.

The second survey occurred on spring break of 2014 and consisted of 4 team members. The main objective of this survey was to gather magnetotelluric data to the west and south of the previous magnetotelluric data. Nine sites were collected, but poor data quality only allowed for six of these to be used in interpretation. This poor data quality can be attributed to the fact that the equipment was fairly new and the kinks in its operation were not worked out yet.

A third trip was performed during fall break of 2014 and consisted of 6 team members. Nine more magnetotelluric stations were collected on this trip. The intent of this survey was to extend the data set along three lines of the existing magnetotelluric data. These data were used for testing the joint inversion program. The three lines were thought to represent areas of geologic structure which were still uncertain. Gravity stations were also collected along two of the three lines to extend them further west. This gravity data is intended to be used later in a joint inversion with the magnetotelluric data. An additional north south gravity line was collected 500m west of the previous data in order to further improve the image of the western part of the valley.

The magnetotelluric data, the geological information, and the gravity data sets were primarily used in this project. The magnetic data were chosen not to be further examined because a strong magnetic signal from an intrusive body dominated the signal. Well logs were used to constrain geology for gravity and magnetotelluric modelling. The induced polarization survey was not used due to its limited depth of investigation. Geochemical data was not used as it is beyond my area of knowledge. Gravity surveys are sensitive to density. In the Jersey Valley area mountain ranges surround the valley. These ranges are composed of generally denser rocks than the basin fill that is present on the valley floor. These denser rocks are also present in the valley beneath the less dense basin fill therefore density distribution helped determining the structure of the

valleys subsurface. Magnetotelluric (MT) measurements give information about the conductivity (reciprocal of resistivity) of the subsurface. Conductivity is based on rock properties and is highly sensitive to fluid content. In Jersey Valley the basin fill should generally be more conductive compared to the other rock units. The information from magnetotellurics may also help determine some fluid locations. Compared to other conductivity based geophysical methods MT has the benefit of high depth of investigation. MT can give us information for a depth range of many meters to hundreds of kilometers. Since the system within Jersey Valley most likely extends kilometers deep this method is appropriate.

2.1.2. Magnetotelluric (MT) data

The data from Ormat includes 206 densely spaced magnetotelluric sites. In addition, 15 more sparsely sampled sites were obtained during the course of this project. In this section, we first show the location of the magnetotelluric data and briefly cover how some of the data were acquired and processed. We also discuss some of the interpretation tools used in this project.

2.1.2.1. Magnetotelluric data

Figure 2.1 shows locations for the magnetotelluric sites in Jersey Valley. The surveys provided by Ormat are concentrated to an area of about 3 km by 3 km around the power station. Although dense this data set misses a lot of interesting geology that might be pertinent to the geothermal system. The additional sites are much more sparsely spaced, but hope to capture some areas of interest. Figure 2.1 and further maps are presented in UTM coordinates, NAD_27 datum, zone 11N.

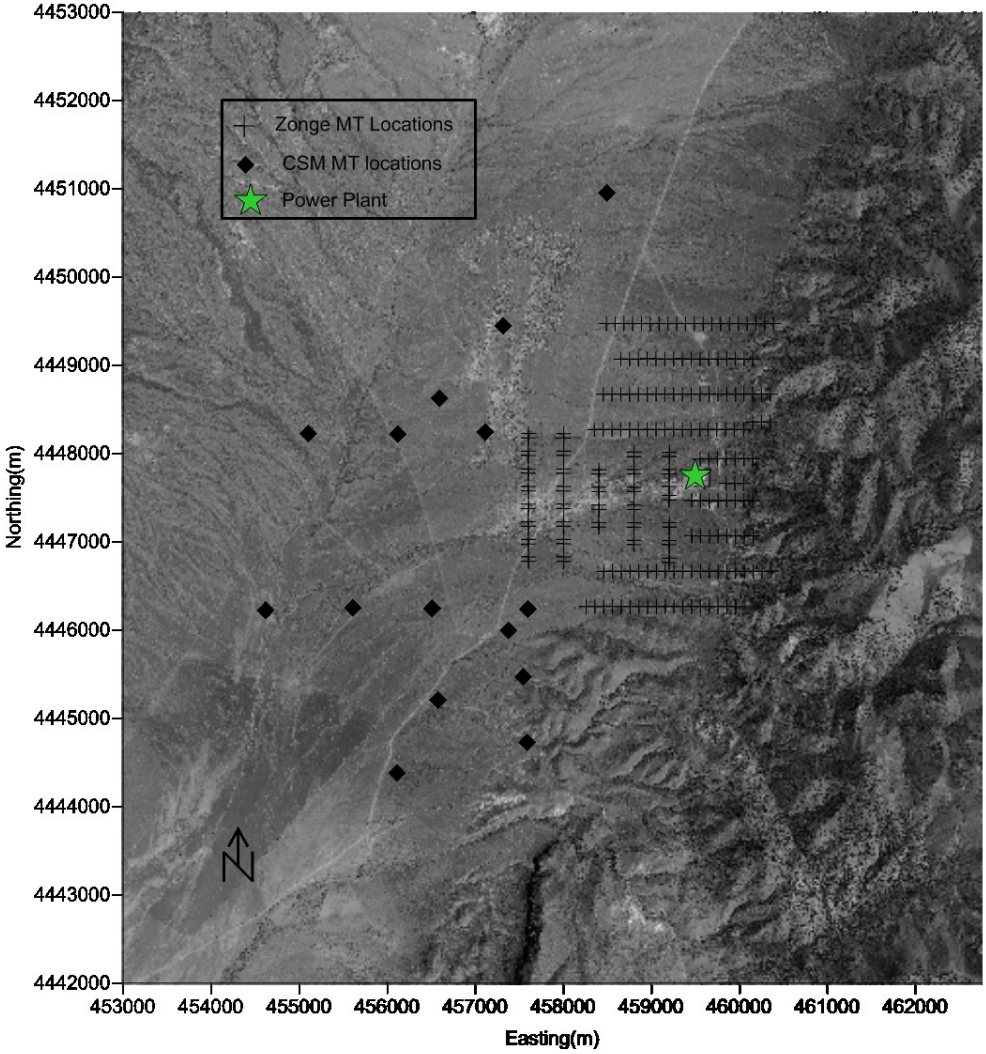

Figure 2.1. A map of magnetotelluric sites in Jersey Valley plotted on satellite imagery, the power plant location is plotted for referencing purposes. CSM stands for Colorado School of Mines.

The magnetotelluric data gathered by the Colorado School of Mines for this project were recorded using a Metronix ADU-07, MFS-06E magnetometers, and lead/lead chloride or silver/silver chloride non-polarizing electrodes. A typical field set up is shown in Figure 2.2, two orthogonal E and H fields are laid out and attached to an acquisition unit. Data was collected at 512 Hz. During data collection the horizontal magnetometers were buried approximately 15 to 30 cm deep to ensure stability against movement from the wind and signal fluctuations with temperature. A compass was used to line up electrodes and magnetometers. This compass was set to local declination so measurements were related to true north. The vertical magnetometer

was used throughout most of the stations. This magnetometer was buried anywhere between two thirds of its length to its whole length deep. Unfortunately the results from the vertical magnetometer were extremely noisy and were not used in this project. Electrodes were placed in small permeable bags in which there were a bentonite mud mix to decrease the contact resistance between the electrodes and the ground. The electrodes were also buried 15 to 30 cm deep to avoid fluctuations caused by temperature changes and wind noise. On particularly windy days or when grazing animals were nearby the electrode and magnetometer cables were buried to protect them and avoid wind noise. Errors in the data gathering process include improper alignment of electrodes and magnetometers, and improper levelling of magnetometers.

For the CSM-GP magnetotelluric data gathered in this phase of the project processing was performed using Mapros software which was provided by Metronix who also sell the ADU 07. The first step in use of Mapros is importing the data into the program. This data is then digitally down-sampled multiple times. Down-sampling is necessary because Mapros only process data from a given sampling frequency through a limited range of frequencies. The next step is to process the data.. The general idea of processing is to obtain values for the impedance tensor elements for a set of discrete frequencies. The software offers multiple processing schemes, we run the default parameters first. If the results provide smooth apparent resistivity curves throughout the set of frequencies of interest and show reasonable coherencies, it is not necessary to perform further processing. Obtaining good results with the first run of processing rarely occurs. Poor results are usually signified by changes that are too abrupt in the apparent resistivity curve. In frequencies with poor results it is necessary to perform further investigation. The first step in further investigation involves examination of the time series data. An example of this data is shown in Figure 2.3. Places where there is a large signal in one channel which is not present in other channels are areas of concern. Usually any signal, including cultural noise is not perfectly polarized with the geometry of the MT setup. Therefore a large signal in one channel should also be somewhat visible in all other channels. Also, even if signals are not apparent in all other channels, because of the physics of induction they should be apparent in the opposing component of the opposing field, i.e., a signal in Ex should be seen in Hy. Areas in the time series that break this principal can be marked and removed from further processing. An examination of the raw and stacked spectra is of value to examine the overall noise level in each channel. If there is a lot of noise in one of the magnetic field channels it is useful to use the remote reference processing method which helps separate noise vs. signal. Often it takes a few attempts to remove the noisy part of the signal and obtain good results. In good conditions various processing results give similar results, but where there is high noise, especially coherent noise, the different methods can yield highly different results.

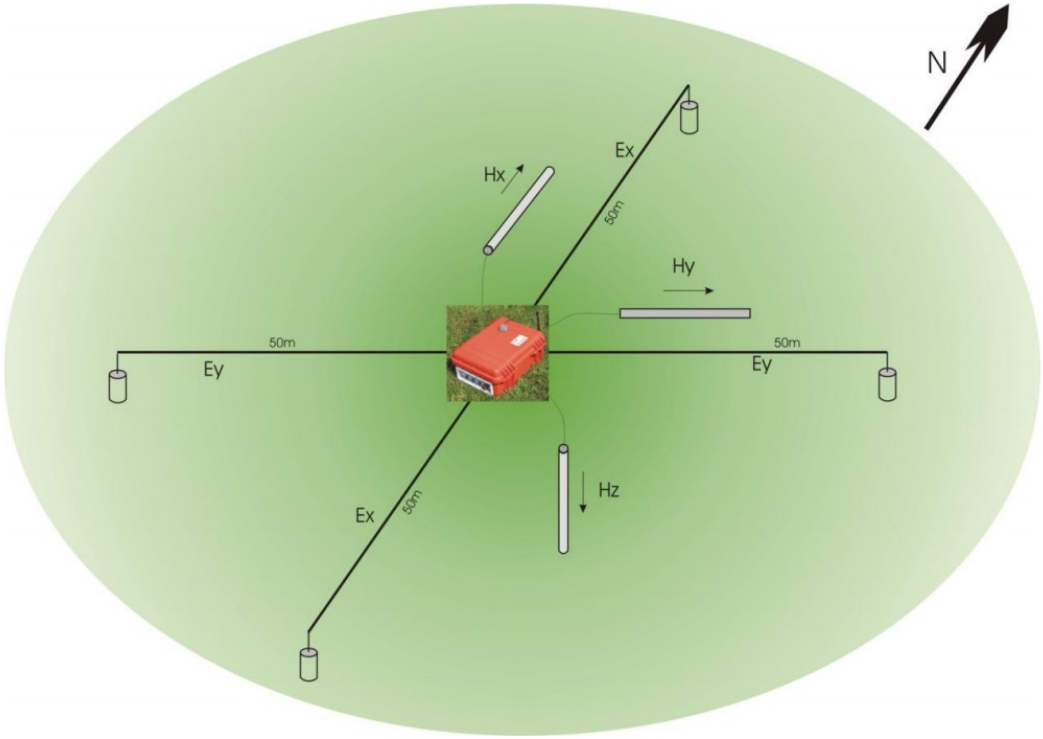

Figure 2.2. Typical field set up of magnetotelluric equipment from Metronix ADU-07 (adapted from Matzander and Wilde, 2007)

Once the data have been processed and an acceptable result received, data can be exported to be further used by other programs. We exported the data to be used in Microsoft Excel. We designed Excel spreadsheets to create polar diagrams, calculate some dimensionality and directionality parameters, and allow for rotation of the impedance tensor and apparent resistivity curves. In general results from the second magnetotelluric survey are much better than from the first. This is likely due to improved technique of the operating crew and more stable electrodes. Results from remote reference processing were often far improved over other processing techniques, suggesting high cultural noise. This noise is likely from the proximity of the geothermal power plant belonging to ORMAT. Future work should include filtering of the time series data from the first magnetotelluric survey to improve results.

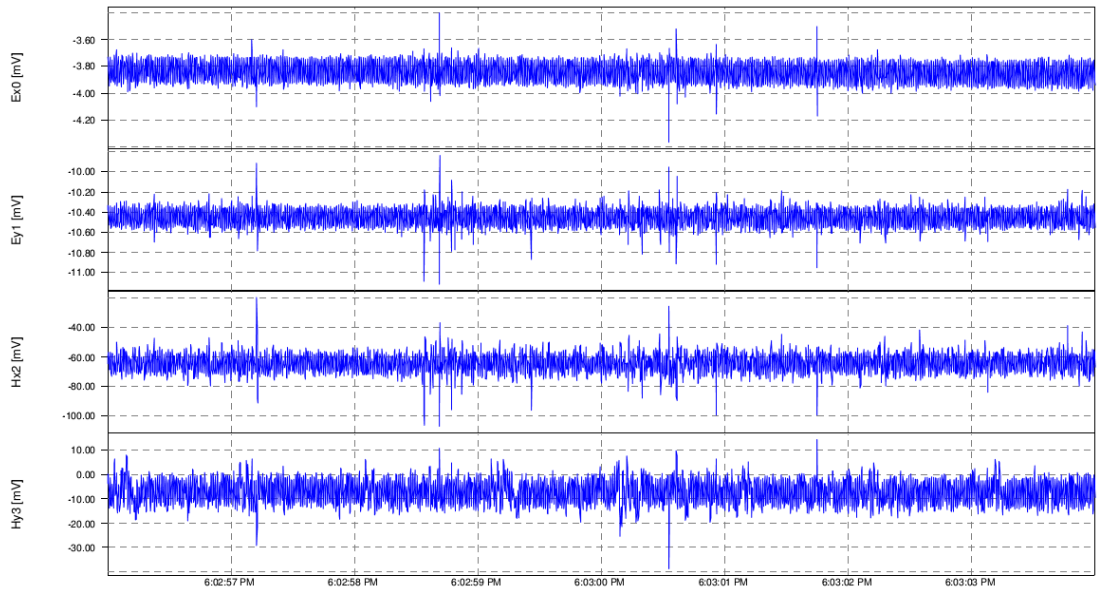

Figure 2.3. Time series data as viewed in Mapros software for the horizontal electric (E) and magnetic (H) fields.

Because of the way Mapros processes data there are multiple impedance tensor values for most of the calculated frequencies. For interpretation, a method for deciding on a single value per frequency needed to be developed. A couple of approaches we tried included averaging and weighted averaging based on variance. So far the best method for noisy data appears to be based on the interpreter picking the best set of values based on coherency, and curve smoothness. Sometimes these are individual values, but usually they are averaged from multiple input values. For less noisy data the best method appears to be a simple averaging, after the removal of any outlier data.

2.1.2.2 Magnetotelluric interpretation

Once the data has been processed to achieve impedance tensor information for a set of frequencies at a site, or multiple sites, a number of tools and principals can be used to help interpret the data. These include interpreting of apparent resistivity and phase curves, as well as apparent resistivity profiles along a line at a given frequency. In addition, properties of the impedance tensor can help determine geoelectric dimensionality and directionality. Although geology is often complex and one dimensional interpretation of magnetotelluric data is insufficient, there is still some information that can be gained from this relatively easy type of interpretation. In the one dimensional case, apparent resistivity can be thought of as an average resistivity over the volume the EM wave is sampling (Unsworth, 2014). Apparent resistivity curves for two 2 layer systems are presented in Figure 2.4. Along curve A at higher frequencies

the apparent resistivity is equal to the resistivity of the shallow layer. As the frequencies decrease skin depth increases and the effect of layer two plays a larger role in the EM induction. At low enough frequencies the shallow layer has little effect and the apparent resistivity becomes equal to that of the deeper layer. Figure 2.4 shows that model B has a thicker first layer than model A. This shifts the curve. One of the problems with one dimensional curve interpretation is the issue caused by conductance, which is the product of conductivity and thickness. When a layer becomes thin compared to its depth it becomes impossible to distinguish different combinations that produce the same conductance (Unsworth, 2014). An additional problem occurs where more than two layers exist and the thickness of some layers are not enough to cause the apparent resistivity to reach close to that layers value before being affected by a deeper layer.

In addition to apparent resistivity, interpreters use the information from the phase values. The Kramers – Kroenig relationship which relates resistivity and phase is shown in equation 2.1 (Bahr and Simpson, 2005). This equation shows that in a constant layer the second part of the equation reduces to zero and the phase is 45 degrees. An increase in resistivity with depth causes phases to increase and vice versa. The nice thing about phase vs. apparent resistivity, is that phase is not affected by static shift, which is discussed shortly below. The phase is given by

$$\phi(\omega) = \frac{\pi}{4} - \frac{\omega}{\pi} \int_0^\infty log \frac{\rho_a(x)}{\rho_0} \frac{dx}{x^2 - \omega^2} \quad (2.1)$$

where ω the frequency, and ρ the resistivity. Often structures are more complex than a one dimensional system and although some information can be gained from one dimensional interpretation it is necessary to expand to 2D-interpretation. 2D interpretation becomes more difficult because of the two modes. One mode is strictly based on induction while the other mode is also affected by an additional E field occurring at vertical conductivity boundaries.

These data can be viewed in profile form by linking stations across a section at the same frequency. It should be noted that this is more complex than representation of the same depth, because shallow features affects the depth of investigation at each site. The effect of 2D structure on a single station can also be taken into account. Figure 2.5 shows the apparent resistivity in profile form as well as apparent resistivity and phase curves for a series of stations across a vertical boundary. As can be seen in the TE mode, where the electric field is parallel to strike, the transition of apparent resistivity is a smooth variation as we approach the contact and cross it. At longer periods the transition becomes even more gradual. On the more resistive side the apparent resistivity starts changing from a one layer value further from the boundary than on the conductive side, this is because the penetration depth of the field is greater on the resistive side off the contact. In the TM mode, where the electric field runs across the boundary, the profile shows how the additional E field at the boundary causes a sharp shift in apparent resistivity. The apparent resistivity curves also show that the TM and TE modes demonstrate very different behavior both relative to each other and on different sides of the contact.

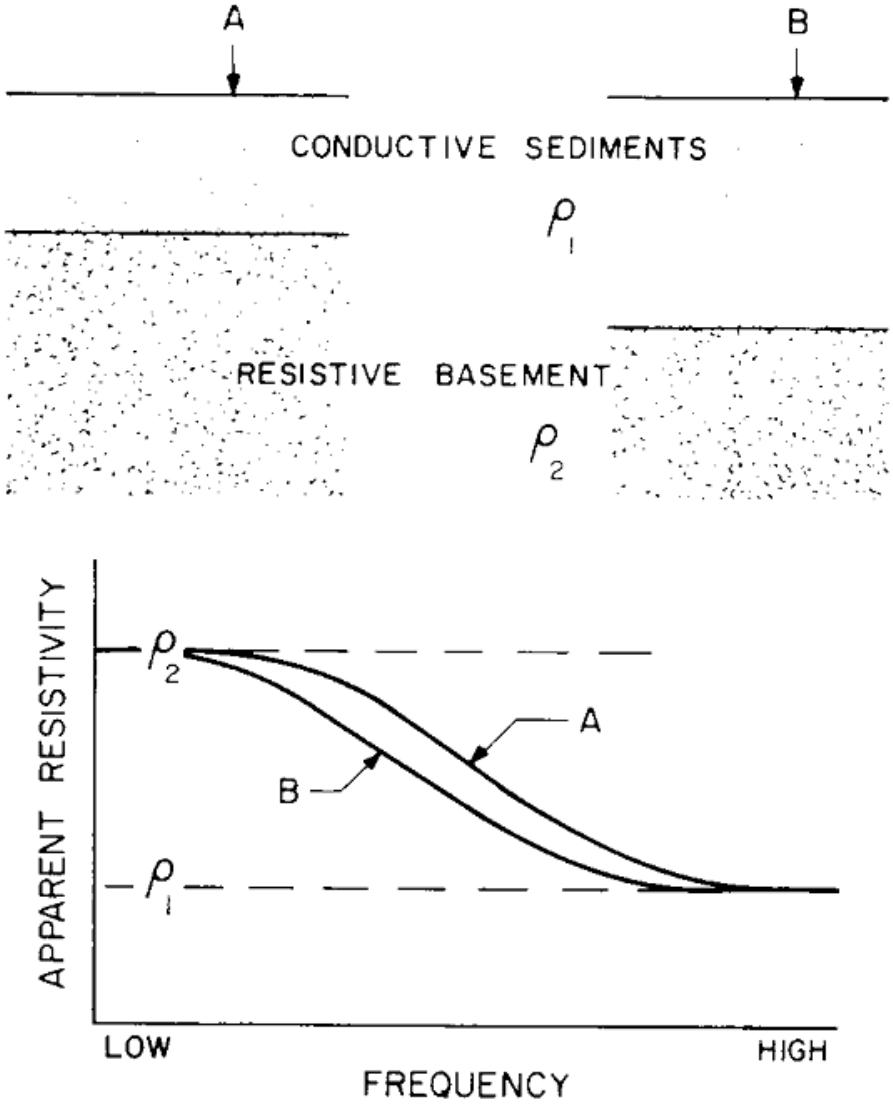

Figure 2.4. Two simple one dimensional two layer resistivity models and there computed apparent resistivity curves (Vozoff, 1972).

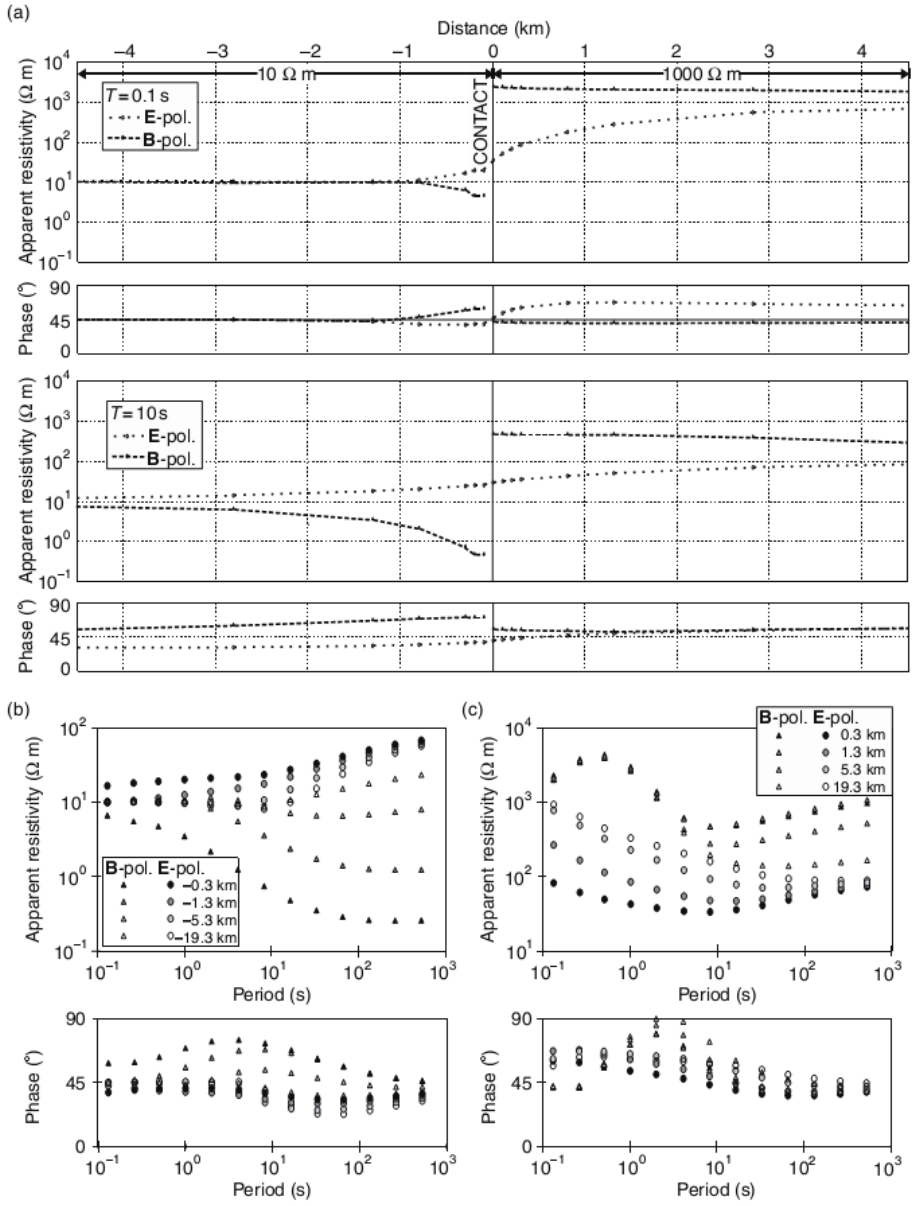

Figure 2.5. Apparent resistivity and phase profiles and single station apparent resistivity and phase curves for stations distributed across a vertical conductivity contrast (Bahr and Simpson, 2005).

Areas with complicated geology often lead to magnetotelluric impedances that are highly representative of three dimensional situations. Three dimensional interpretation is far more difficult than two dimensional and really requires modelling or inversion. Luckily there are some principles that can be applied to three dimensional data to obtain useful information about any large scale two or one dimensional background features. Figure 2.6 shows how a three

dimensional body effects the induction process at various frequencies. At frequencies too high for the fields to sample the 3D body induction remains as if the body were not present. As frequency decreases the body is sampled along a single edge and induction and galvanic shift is that of a 2 dimensional structure. As the field samples more of the body three dimensional induction dominates the signal. As the wavelength of the field further increases induction of the body becomes negligible, but galvanic effects remains through all frequencies.

In addition to interpreting one dimensional curves and two dimensional sections, often knowing the dimensionality and direction of features helps determine appropriate interpretation methods, and in itself can be of great value. Polar diagrams offer a pictorial representation of geoelectric dimensionality and directionality at a single frequency. The impedance tensor is often collected in north-south and east-west orientations, but once the information is gained the tensor can be rotated to any orientation. To rotate the tensor equation 2.2 is applied.

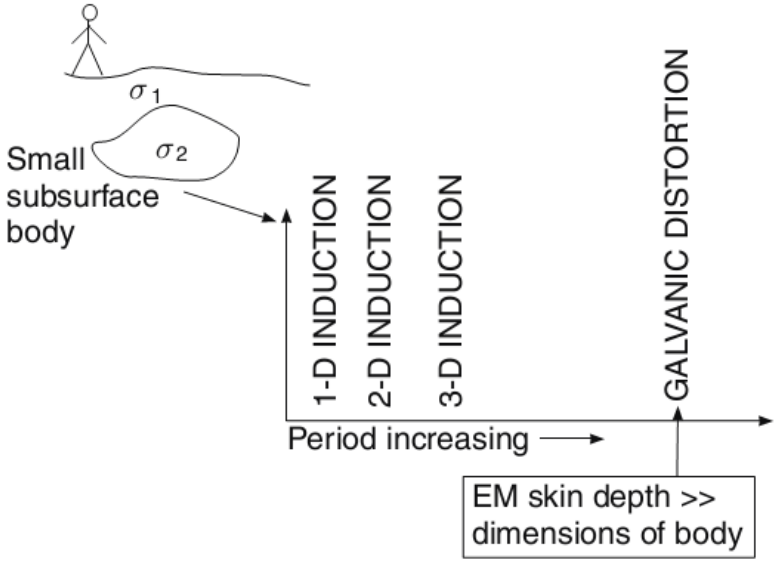

Figure 2.6. Three dimensional bodies effect on magnetotelluric induction at a range of periods (Bahr and Simpson, 2005).

$$[Z(\alpha)] = [R(\alpha)][Z][R(\alpha)]^{-1} \tag{2.2}$$

where $[Z]$ denotes the impedance tensor, and

$$[R(\alpha)] = \begin{bmatrix} \cos(\alpha) & \sin(\alpha) \\ -\sin(\alpha) & \cos(\alpha) \end{bmatrix} \text{ is a rotation matrix}$$

This leads to

$$Z_{xx}(\alpha) = Z_{xx}\cos^2\alpha + Z_{yy}\sin^2\alpha + (Z_{xy} + Z_{yx})\sin\alpha\cos\alpha \quad (2.3a)$$

$$Z_{yy}(\alpha) = Z_{yy}\cos^2\alpha + Z_{xx}\sin^2\alpha - (Z_{xy} + Z_{yx})\sin\alpha\cos\alpha \quad (2.3b)$$

$$Z_{xy}(\alpha) = Z_{xy}\cos^2\alpha - Z_{yx}\sin^2\alpha - (Z_{xx} - Z_{yy})\sin\alpha\cos\alpha \quad (2.3c)$$

$$Z_{yx}(\alpha) = Z_{yx}\cos^2\alpha - Z_{xy}\sin^2\alpha - (Z_{xx} - Z_{yy})\sin\alpha\cos\alpha \quad (2.3d)$$

Rotating the elements of the impedance tensor through three hundred and sixty degrees and plotting them as polar diagrams it is possible to get some dimensionality and directionality information. The radii of each component represent the magnitude of that component at the rotation angle. So for one dimensionality we should see the same magnitude for the off diagonal elements no matter what direction since $Z_{xy} = -Z_{yx}$. Also in the one dimensional case $Z_{xx} = Z_{yy} = 0$ so the polar diagrams for the diagonal elements stay near zero, with some magnitude due to noise. The two dimensional case is shown in Figure 2.7 from Vozoff (1991). In a two dimensional situation the off diagonal elements are represented by a figure eight or oval shape with the maximum and minimum axes aligning with or orthogonal to the structure as shown in Figure 2.8b. In the two dimensional case there is a ninety degree ambiguity. This ambiguity can be resolved with other data and/or multiple sites. For the two dimensional case the diagonal elements of the tensor are represented by shapes like a four leave clover as seen in Figure 2.8b where they reduce to near zero at directions parallel and perpendicular to electromagnetic strike. In a three dimensional situation because none of the impedance tensor elements are equal the polar diagram start to take on odd shapes and all elements are represented by oblique figure eights (Berdichevsky, 2008). In certain cases where the bulk structure is two dimensional with three dimensional bodies present the diagrams may still give valuable information.

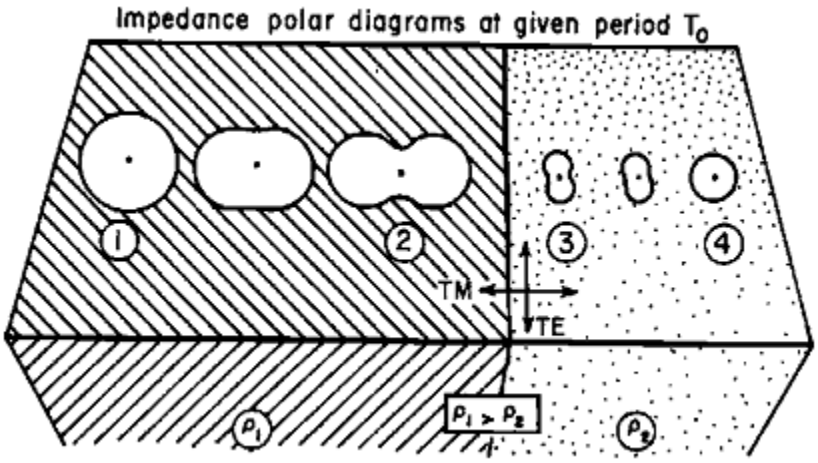

Figure 2.7. Impedance polar diagrams across a conductivity contrast for the off diagonal component of the impedance tensor in which the electric field is measured perpendicular to strike (Vozoff, 1991).

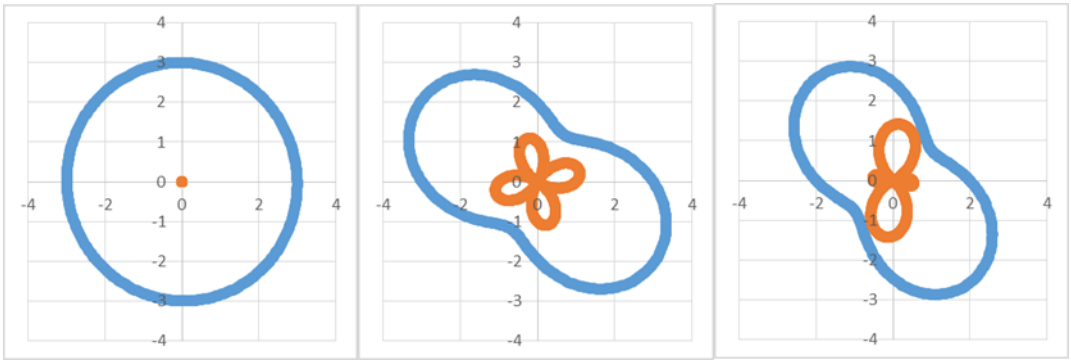

Figure 2.8. Impedance diagram for one dimensional (a), two dimensional (b), and three dimensional(c) geoelectric structures. The blue line represents an off diagonal element of the tensor, and the orange a diagonal element.

A freeware one dimensional modelling/inversion software for magnetotellurics is available online from Bobatchev (2013). This software allows for input of apparent resistivity and phase curves. A relative error can be input which plots the data as error bars instead of curves. The data values and computed model curve are plotted, along with a model containing depth and resistivity values. Inversion parameters such as minimum number of layers and weighting between phases vs. apparent resistivity can be easily entered. Once a curve has been created the user can manipulate the model relatively easy by clicking the model layer and adjusting the extent or resistivity of each layer. The calculated curve responds immediately. Alternatively the model can be adjusted by entering given values into the table. This is particularly useful when the user wants to constrain either depth or resistivity based on previous

information. In the work presented here the inversion feature was only used to help come up with initial model parameters, then these were adjusted appropriately and used as a starting point for further models. Because the transverse magnetic mode is least sensitive to two dimensional effects, it was used more often. This proved somewhat successful, but did not provide for great fits to all curves. Issues may have been caused by the effect of parallel layers away from the site causing a difference in the average resistivity, static shifts from east west features, varying permeability of layers due to the presence of increased fracture zones, and hydrothermally altered materials which have higher conductivities.

2.1.3. Gravity

A dense set of gravity data exists near the power plant and a less dense set exists for a large remainder of the valley. The location of the data is shown in Figure 2.9. In this section, we cover the gravity data set, some basics of acquisition and processing, and some basic interpretation tools.

2.1.3.1 Gravity data

Gravity data for the Colorado School of Mines was collected using a Scintrex CG-5 gravimeter. Two sets of measurements were performed at each station with measurement times of 30 to 45 seconds, and data collected each second. This allows for many data points to be collected and averaged. The difference between the two measurement sets were small. Three points from each of the two surveys were coincident with points from the data given by Ormat. This allowed for the gravity data to be tied to previous surveys. To account for gravity field changes caused by groundwater level fluctuations the repeat gravity stations were located in the hills.

Since gravity data processing cannot be performed effectively without accurate location information, in addition to collecting gravity data accurate location data was collected using a Trimble Global Positioning System (GPS). This system was used in real time kinematic configuration, which allows for atmospheric corrections to be performed while data is being gathered and provides data with relative accuracies to within a centimeter. A drawback to this way of collecting data is that line of sight communication between a base station antenna and roving antenna is necessary for point collection. The system has great relative accuracy, but unless the base station is positioned at a known location the absolute accuracy is limited. For this reason during each survey a single base station location was maintained and measurements were taken on three points that are coincident with points from the Ormat data set. This allowed me to tie location information to the previous data.

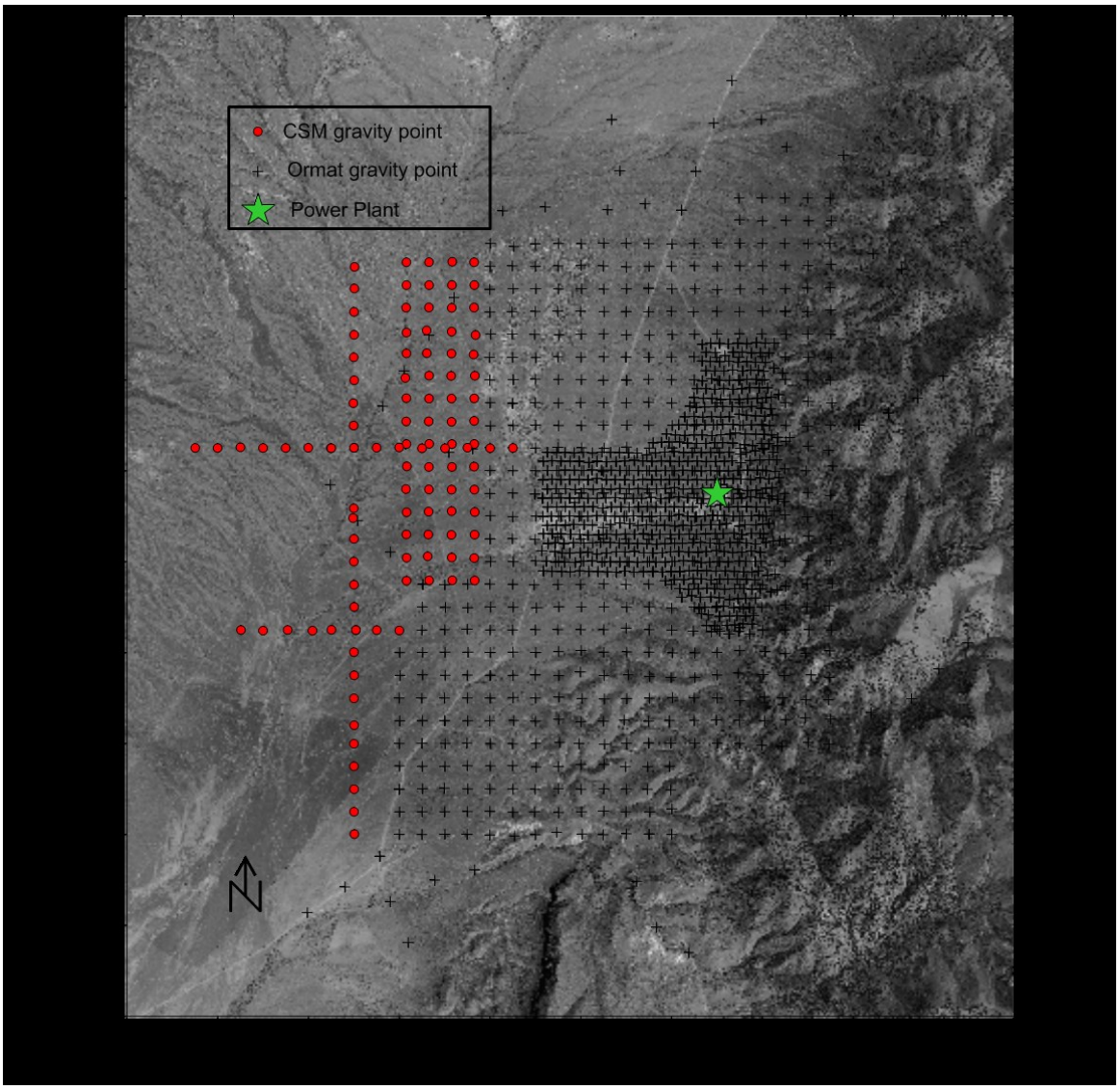

Figure 2.9. Map of gravity sites within Jersey Valley, plotted on satellite imagery, the power plant location is plotted for referencing purposes.

Because data from previous surveys was processed using software not available to me, in order to tie data from all surveys together all data were processed together. Unfortunately height information from the two previous surveys was inconsistent and it was necessary to extract vertical location information by reversing it out of the free air corrected values. Luckily the equations necessary to do this were provided in the reports.

Standard corrections were performed following the method from Bauer (2013), the method to correct for a Bouger gravity anomaly is given in equation 2.4. A background density value of 2.35 g/cm^3 was used based on gravity reports. The terrain correction was performed with use of a program from http://www.cas.umt.edu/geosciences/faculty/sheriff/438-Gravity_Electromagnetics/TerrainCorrections.htm. This program uses hammer charts; to implement the program a DEM of 5 meter resolution was used for inner hammer zones, a 30 meter grid was used for mid-range hammer zones, and this grid was down sampled to 100 meter resolution for outer hammer zone corrections.

$$g_c = g_{obs} - lat + Fa + Bouger + TC \tag{2.4}$$

where g_c is the final corrected gravity value, g_{obs} is the observed gravity value, lat is the latitude correction, Fa is the free air correction, $Bouger$ is the Bouger slab correction, and TC is the terrain correction.

2.1.3.2. Gravity Interpretation

Gravity data can be plotted as profiles or maps, but often the gravity anomalies of interest are difficult to see. This is because often the anomalies of interest are superimposed on large background features. Several techniques can be used to enhance anomalies of interest. Nabighian (2012) mentions the use of derivatives in emphasizing shallow targets. These derivatives can also be used to try to find the edge of targets (Shandini, 2012). In order to implement the horizontal first derivative in two dimensions the total horizontal gradient is used, shown in equation 2.5 (Nabighian, 2012). Because the method is good for identifying edges it can be very useful in locating fault zones. A drawback to using this method is that it only gives magnitude of the derivative so positive versus negative anomalies are not separated, but this information can be found using other data.

$$THG = \sqrt{\frac{\partial M^2}{\partial x} + \frac{\partial M^2}{\partial x}} \tag{2.5}$$

where THG is the total horizontal gradient, M is the potential field, in this case the gravitational field, x and y are two orthogonal directions across the surface. Another technique to enhance anomalies of interest is regional residual separation. Long wavelength gravity signals reflect deeper large scale features. Since the anomalies of interest are often shallower or smaller scale these lead to short wavelength anomalies. Removal of long wavelength signal may reveal these shorter wavelength anomalies. There are multiple methods to perform regional residual separation, Thurston and Brown (1992) discuss the use of low order least squares polynomial fitting to the data as the regional. This makes intuitive sense because long wavelength features should be smooth.

Another method that can be used for regional residual separation is the finite element method. For this technique gravity values from the edges of a rectangular shaped region are picked and a quadratic or cubic surface is fit to nodal values on these edges (Mallick and Sharma, 1997). Following the information from Mallick and Sharma (1997), we wrote an Excel program that when given the nodal values for eight points in a rectangular grid (the four corners and four midpoints) a quadratic element is calculated over the area. This area is then gridded and subtracted from the gravity to arrive at a residual. One drawback to this method is that if the nodal values are not a good representation of the average gravity in that area it might cause a surface that is not appropriate. Another drawback is that it can only be applied to a rectangular area.

Profile modeling is appropriate where the density contrast is two dimensional and the profiles are perpendicular to the structure. Even when there are three dimensional effects, if the bulk background is two dimensional information can be obtained. In order to perform profile modelling we downloaded a 2.5 dimensional profile modelling program from Talwani (2012). To create a model, a background density needs to be defined then bodies are defined that are descriptive of the geology. Bodies are defined by a closed geometry from a number of points and a given density value. An input file with gravity points including survey location, elevation, and Bouger corrected gravity is created as well. The program displays a model consisting of the closed bodies, and a plot displaying the data, and calculated gravity data based on the model. The user can change the model by moving body vertices or changing density values. The calculated values change immediately in accordance to the adjusted model. The program is considered two and a half dimensional as the bodies orthogonal length can also be input. For use in this project bodies were kept two dimensional by defining large orthogonal lengths. Attempts to input models and gravity values at Nad27 easting or northing and elevation were not successful so all the models were created using the start of the profile as zero distance and the highest point along the profile as zero elevation.

2.1.4. Conclusion

An extensive data set and a couple of models exist, including the Leapfrog® model which was created using some of the geophysical data. Unfortunately the Leapfrog® model is limited in extent and we have seen no written justification of the model. A valley sized conceptual model and report from Drakos et al. (2011) exists. Although the report claims that the gravity data was used against this model, the report fails to produce any real justification of the use of geophysical data, such as descriptions of gravity maps compared to the hypothesized model. The extensive magnetotelluric data was collected after the aforementioned report and this data was used in the Leapfrog® model, but we have found no mention of this data in testing the larger conceptual model. In addition to the poor justification of the current model, data were

clearly lacking in the western part of the valley, CSMGP surveys attempted to get further data in this region. The next section elaborates more on the initial conceptual model and the Leapfrog® model as well as introduce another conceptual model.

2.2. Starting Models

We have introduced the idea of a conceptual model and shown that it should address a number of elements. In this section, we introduce some starting conceptual models and their key structural elements. In addition, we address some aspects of the Jersey Valley geothermal system not present in the starting models.

2.2.1. Starting models

Three conceptual models of Jersey Valley structure which we believe are appropriate for testing are examined. Testing of the models uses the geologic, gravity, and magnetotelluric data that were mentioned above with the geophysical data sets. Testing of these models helps in developing future models, which then can then be tested against the data. The models are referred to as model 1, model 2, and model 3. Table 1-1 summarizes the three models, and they are further described in this section.

Table 1-1: Summary of structural models and their key elements

Model	Key Elements
1	Relay ramp between Fish Creek Range-front Fault and Augusta Mountain Range-front Fault
2	Valley fault/faults with significant displacement
3	An east west fault, near the power plant

Model 1 covers the extent of Jersey Valley Ormat, this model is shown in Figure 2.10. Along with the picture of the conceptual model Drakos et al. (2011) provides the following details: 1) A north-south range fault system, 2) A basinward north-south fault system, 3) An east-northeast striking fault system which functions as a relay ramp between the aforementioned north-south fault systems. The key aspect of this model is a relay ramp that provides accommodation for the shift in displacement along the range-front faults. Displacement shifts west along the Augusta Mountains relative to the Fish Creek Mountains. This model is referred to as model 1 in the remainder of this report.

Figure 2.10 shows the second model which is from Schwering and Karlin (2012). This conceptual model is from Dixie Valley, but since Jersey Valley is the northern extension of Dixie Valley there are possible similarities. In Jersey Valley this model would be flipped. The range-

front fault is to the east with the valley fault to the west. Nosker (1981) also suggests a similar possible structure in his project on Jersey Valley. The main structural element of this model is that significant displacement does not only occur along the range-front fault, but also among faults within the valley. This model is referred to as model 2 in the remainder of this report.

Figure 2.11 shows the final starting structural model of the valley, this model only covers a very small section of the valley. The main structural aspect of this model is an east trending graben not present in the other two models. The location of this proposed graben is under surface sinter material and is in line with Jersey Hot Spring. This suggests the hypothesized structure might play some role in the system. This model was presented using the Leapfrog® Viewer software, which is freely available. This model is referred to as Model 3. We have presented three models that can be tested using the geological and geophysical data. For this project the focus was on testing of structure.

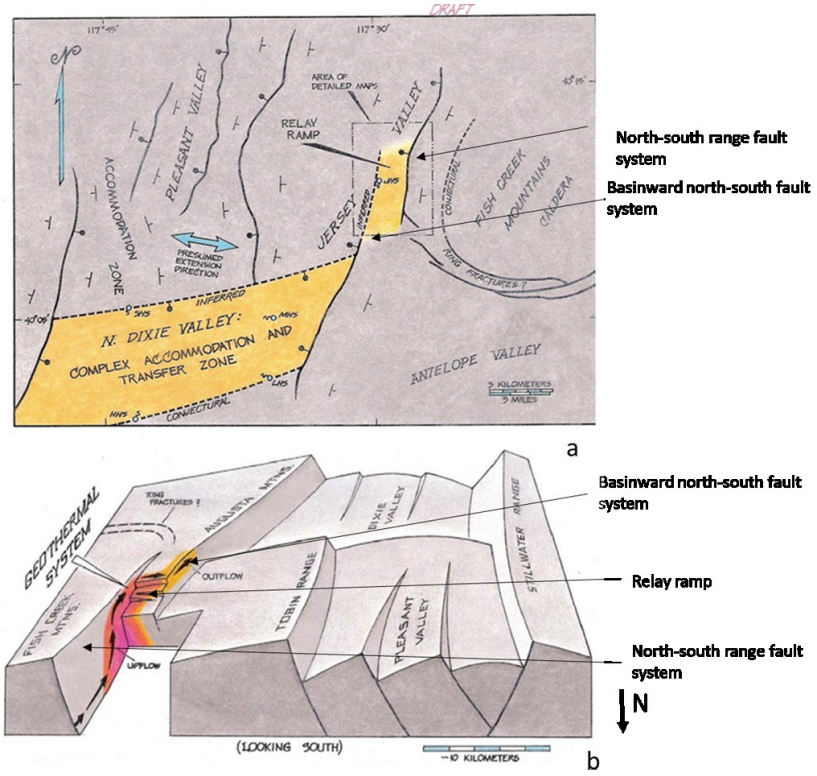

Figure 2.10. This sketch presents a conceptual model of bulk structure and fluid flow given to us by Ormat Technologies Inc. and described by Drakos et al. (2011).

Although models 1 and 2 conflict with each other, model 3 may exist in conjunction with model 1 or 2. These 3 models do not address the issues of size or heat source of the system, and for a better understanding of the system we briefly address these issues.

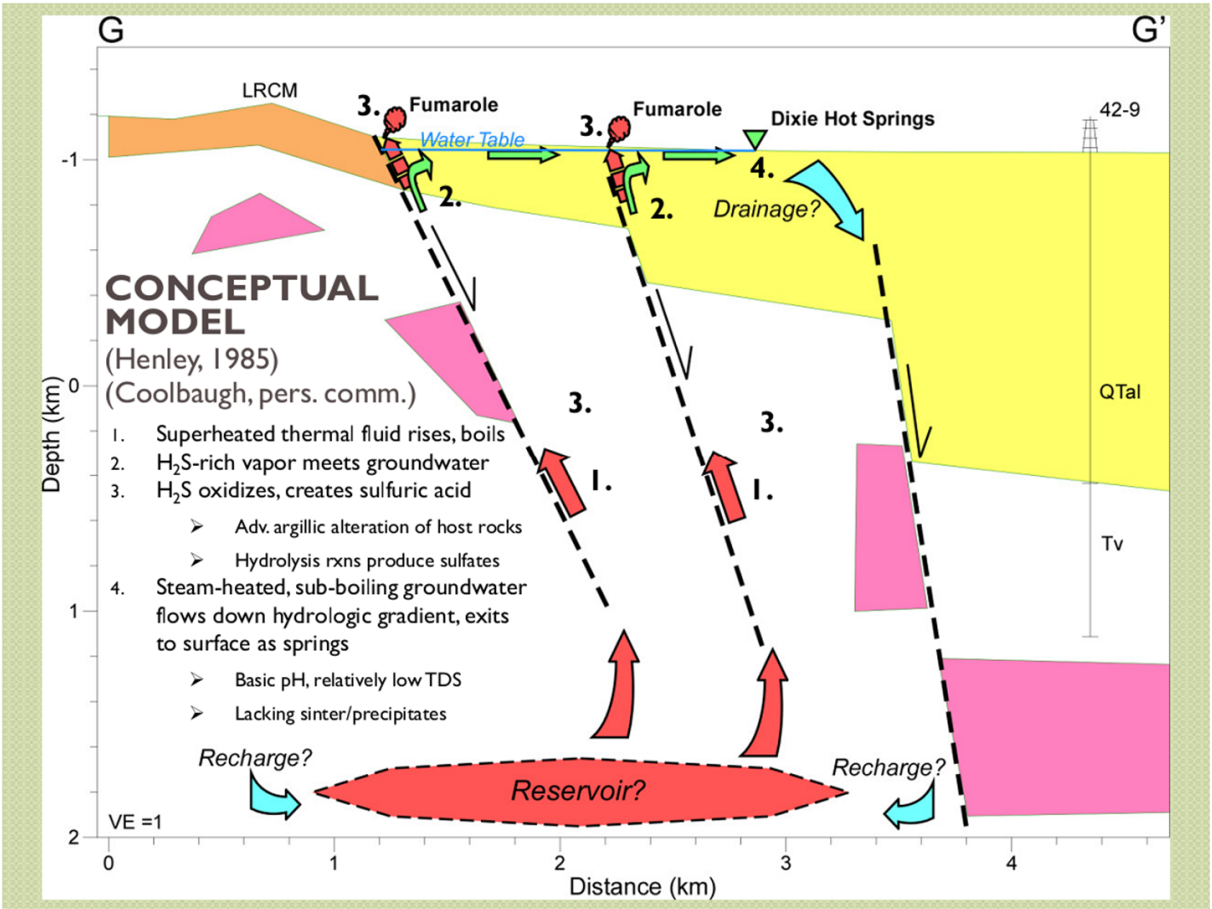

Figure 2.11. Model 2: Conceptual model of Dixie Valley from Schwering and Karlin (2012).

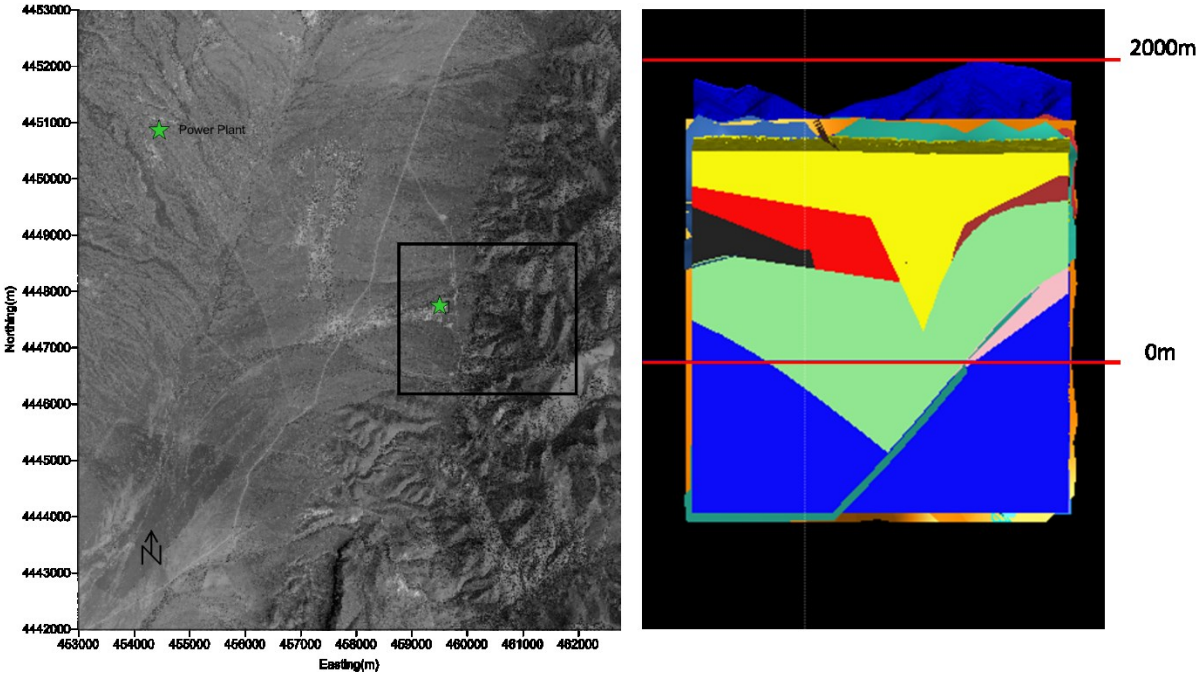

Figure 2.12. Model 3: On the right side of the image is the Leapfrog® model from the Ormat data set. The view of the model is looking from the west towards the east. The left side of the figure shows the location of the area covered by model, location of the power plant is included for reference.

2.2.2. Size of the system

A look at the regional structure of Jersey valley might give information on the extent of the geothermal system. We present regional gravity to address the subject of regional structure. Figure 2.13 shows a regional gravity map of data obtained from the USGS for the region around Jersey Valley. The data was gridded using Golden Software's Surfer program. A clear gravity high exists between Jersey and Dixie Valley. In addition, a relative gravity high is also present between Jersey and Buffalo Valley. These gravity highs suggest that the less dense valley fill material decreases in thickness between the valleys. Since we are looking for deep circulation of fluids, it is likely the system at Jersey Valley is isolated unless fluids are linked between the valleys through fractures.

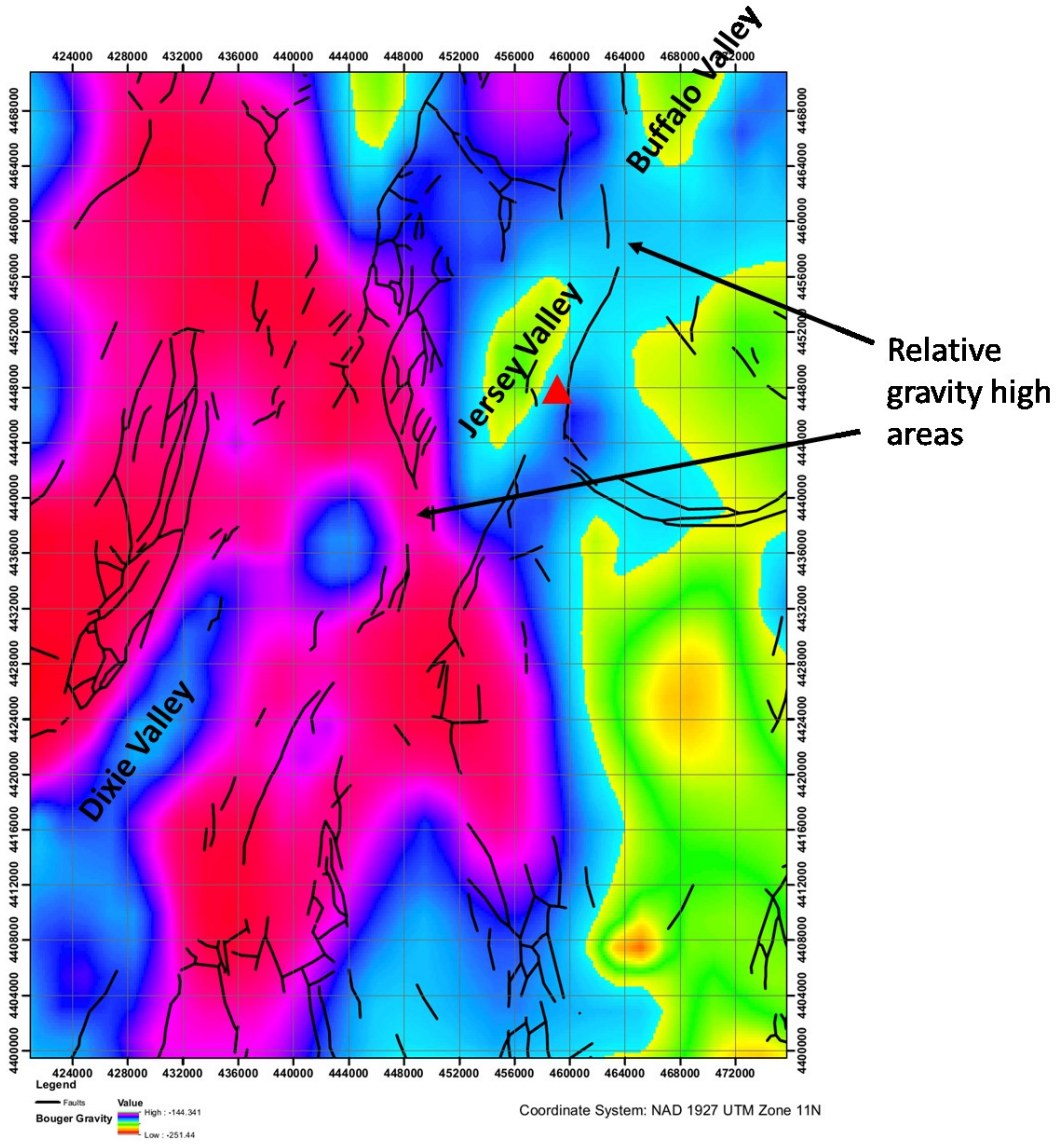

Figure 2.13. Regional Bouger gravity map of the region surrounding Jersey Valley, approximate location of the power plant is designated by the red triangle.

2.2.3. Type and heat source of system at Jersey Valley

To address what the heat source is, we investigate the regional tectonics and other geothermal systems in the Basin and Range region. Nevada has a relatively high concentration of geothermal fields. This is in part due to the regional extension in this area. Faulds (2004) mentions that the movement of the Walker Lane right lateral strike-slip fault causes a northwest

extension in the Great Basin. This together with regional extension provides for thin highly fractured crust. The thin crust allows upwelling of mantle material and the high fracturing allows for deep fluid circulation (Faulds, 2004). Faulds (2011) characterized the structural settings of more than 200 geothermal fields in the Great Basin and concluded that most systems occur where multiple faults interact. This suggests that the increased fracturing which occurs in these regions is an important factor, probably because it allows for deep fluid transport. Going back to the parts of a geothermal system, the upwelling of deeper warmer materials likely provides the heat source and the highly fractured rock likely acts as the reservoir and supply of water. These are most likely convective fracture zone systems. Runoff from the mountainous regions that feeds the groundwater system likely provides the recharge mechanism.

2.2.4. Geology

In order make use of the geophysical data obtained at Jersey Valley a brief background in geology of the area is valuable. A geologic map is presented in Figure 2.15. The geologic units in the map are from data available through the USGS. The faults shown are those common to multiple fault maps which were examined. The earliest rocks present, which are considered the bedrock were deposited when this area was a deep marine environment during the Carboniferous and Permian periods. In Jersey Valley these rocks comprise the Havallah sequence and are mainly chert and quartzite with some slate and limestone (Nosker, 1981). In the geologic map these rocks are labelled PMh. After this deposition the area underwent subduction. Transgression and regression of the ocean controlled the depositional environment. During this time environments like river deltas, beaches, and lagoons were present. Rocks deposited in this time are conglomerates, sandstones, and dolostone (Nosker, 1981). These are represented on the geologic map by units labelled TRc. This was followed by thrusting which produced andesite flows and intrusive rocks in the region. These rocks are represented by units labelled Ta2 and Ta3 on the geologic map. In the Jersey Valley region this was followed by the eruption of the Fish Creek Mountains during the Miocene, which produced the Fish Creek Mountain Tuff.

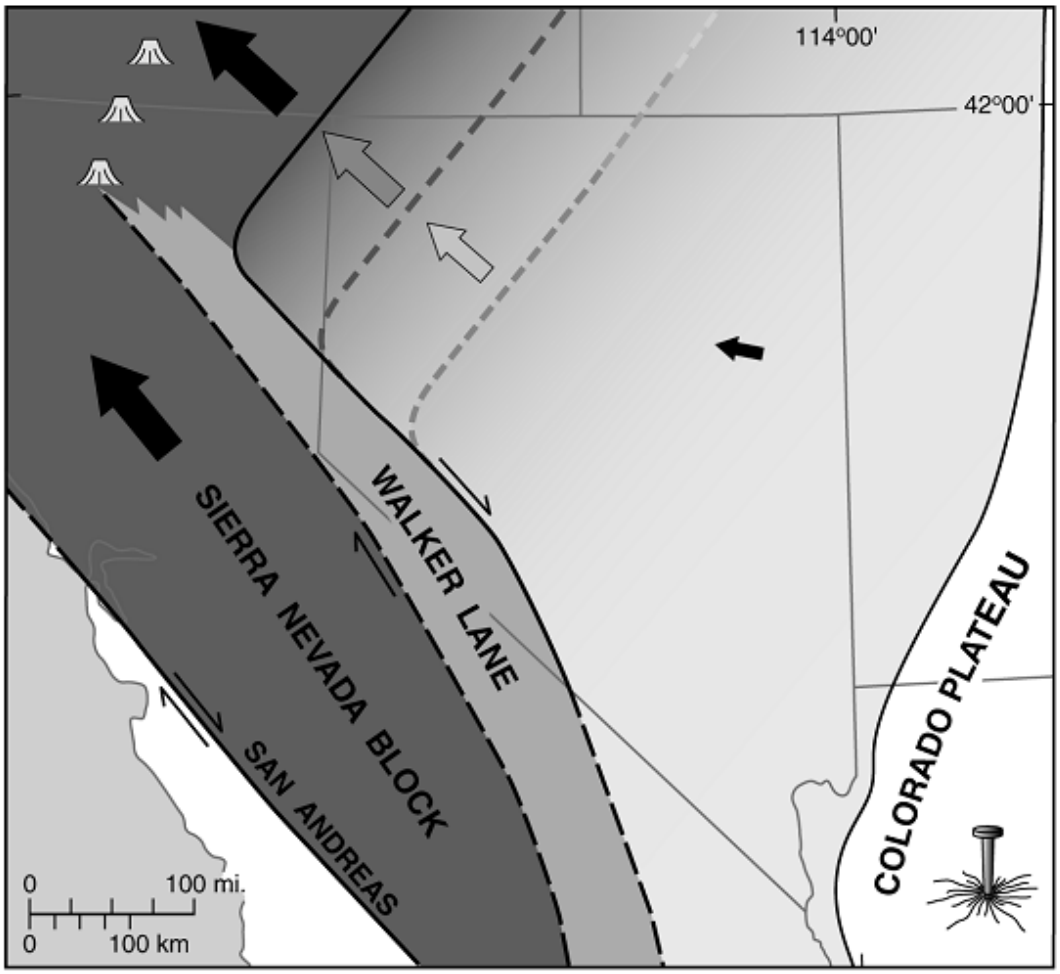

Figure 2.14. Movement along the Walker lane causes a northwest extension in the Nevada region. This leads to the Basin and Range topography with north to northeast trending normal faults (Faulds, 2004).

According to McKee the eruption produced an ashflow covering an area of sixteen miles in diameter, ranging in thickness form 3000' to 100' thick near the edges. This is a rhyolitic tuff and on the geologic map is represented by units labelled Tt2. Two curved faults that are present to the south of the Fish Creek Mountains are determined to have been produced at some point between the ashflow and basin and range extension. According to McKee (1970) the next geologic record present in the Jersey Valley rocks are tertiary lacustrine sediments. These rocks suggest that basin and range extension had started (McKee, 1970). Rocks from this period are represented by the Ts3 labelled units on the geologic map. Extension continued and is still continuing today. This extension allowed for the uplift of the mountains bounding Jersey Valley and the down-dropping of the valley. The extension has caused thinning of the crust and high fracturing. Rocks deposited in the Jersey Valley during the Quarternary mostly consist of

alluviums, and hot springs deposits. The alluvial material is represented by the Qa label on the geologic map. Sinter deposits from hot springs are not shown on this map. More detailed geologic maps show the sinter deposits, in particular there is an east west trend of sinter deposits near the power plant.

Figure 2.15 shows three main faults in the area of interest; we have labeled them as the Fish Creek Range-front Fault, the Augusta Mountain Range-front Fault, and a fault within the valley that is referred to as the Valley Fault in this project. The Valley Fault is the one of most interest to study with the geophysical data, because it gives us the most information regarding the starting models. The Valley Fault can be consistent with models 1 and 2. In the case of the model 1 the Valley Fault and Augusta mountain fault are connected. Also displacement decreases to the north along the Valley Fault. In the case of model 2 the Valley Fault has significant displacement. Faults consistent with model 3 are not seen on the fault map.

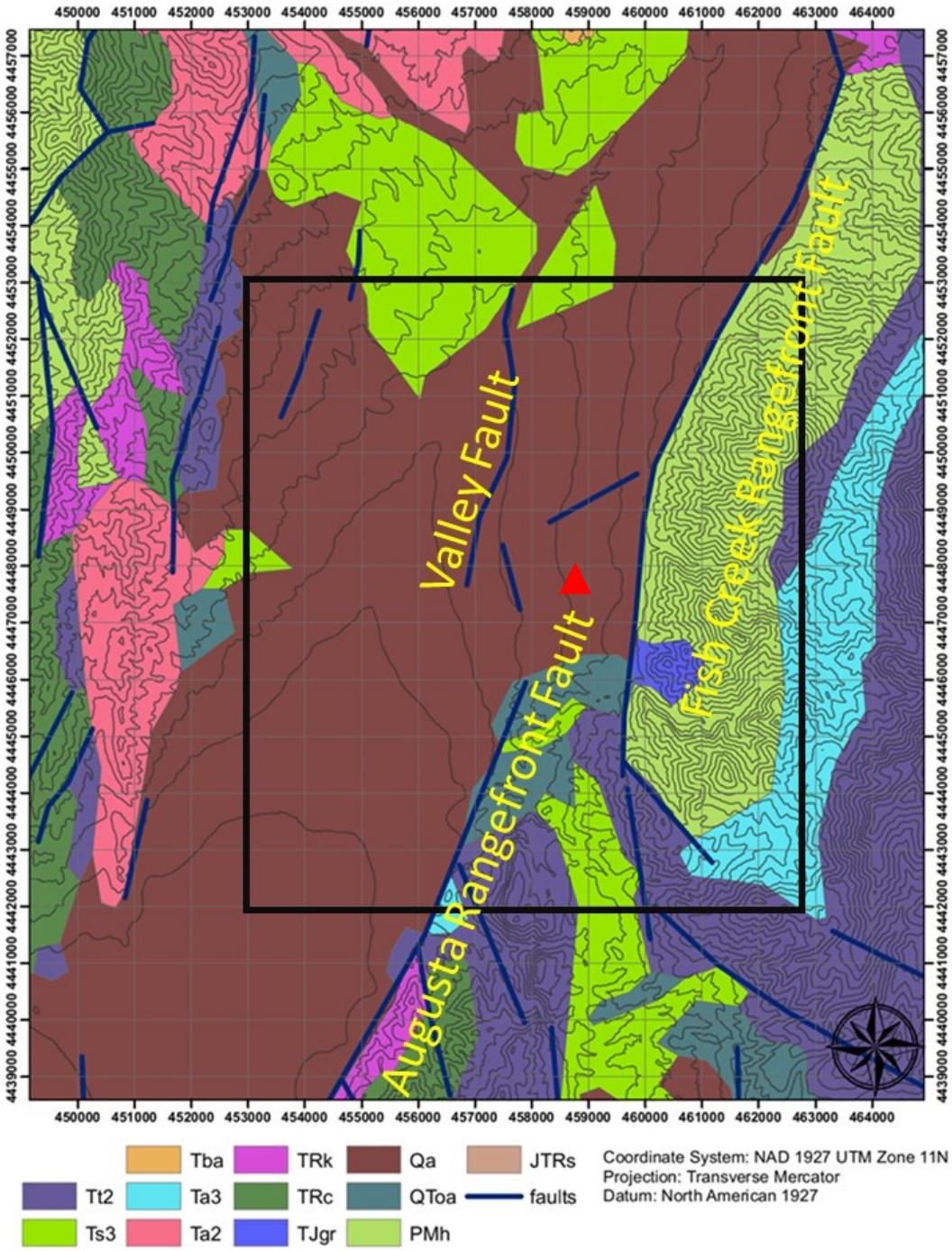

Figure 2.15. Geologic map of Jersey Valley with geologic units and faults. The orange triangle shows the approximate location of the power plant. The black outlined rectangle shows the approximate location the data maps which are used in this project.

2.2.5. Digital elevation model

Before presenting the geophysical data, we discuss simple geomorphology which might provide some information regarding structure of Jersey Valley. A digital elevation model with 30 meter resolution was trimmed to the area of interest and projected to UTM Nad_27 datum. The model is presented in Figure 2.16. This model shows a shift in displacement that occurs from the northern part of the valley to the south. The topography between the two mountain ranges is consistent with what might be expected of a relay ramp. It is easy to see why the relay ramp model was chosen. No information regarding the models 2 and 3 can be concluded from this figure.

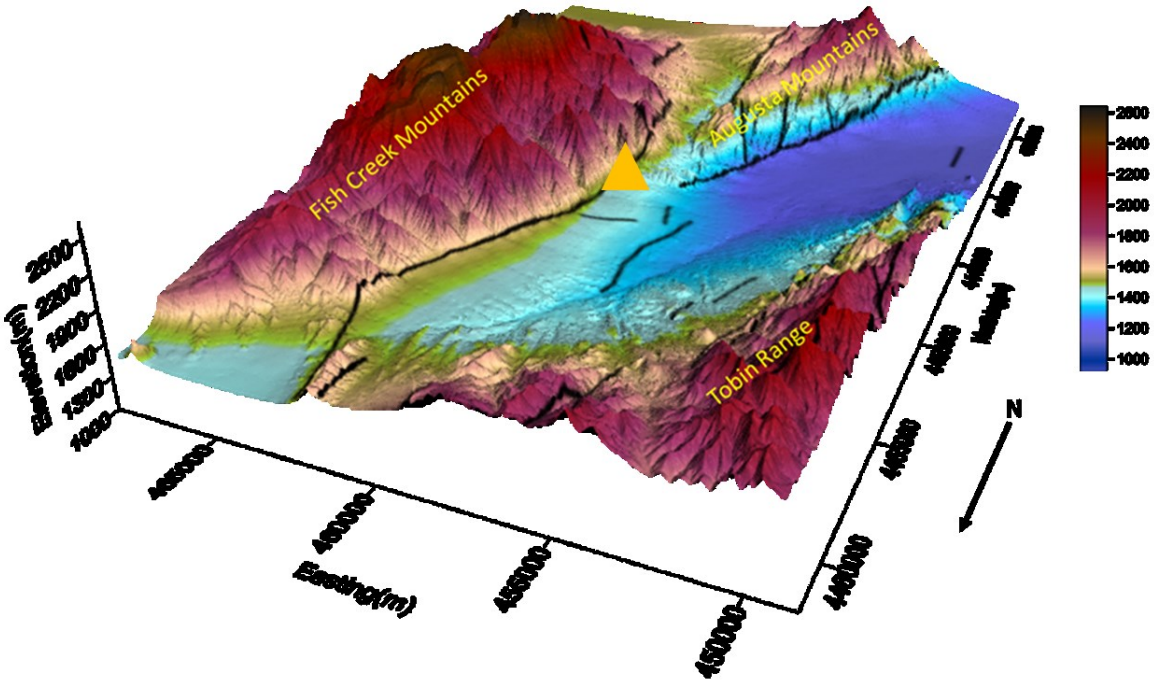

Figure 2.16. Digital elevation model of the Jersey Valley region. The three mountain ranges bounding the valley are labelled. The orange triangle marks the approximate location of the power plant.

2.2.6. Conclusions

In this section, the size and type of the geothermal system have been addressed, and a series of structural models for the valley have been presented. In addition a geologic map with fault locations and DEM was shown. The geomorphology appears consistent with the relay ramp model, but what does the geophysical data tell us. This is the focus of the remaining sections. Table 2.2 summarizes the current structural models and their supporting data.

Table 2-2. Starting structural models, the main elements, current supporting data, and notes.

Model	Key Elements	Supporting data	Notes
1	Relay ramp between Fish Creek Range-front Fault and Augusta Mountain Range-front Fault	Fault map DEM	Competing against model 2
2	Valley fault/faults with significant displacement	Fault map	Competing against model 1
3	An east west fault, near the power plant	Surface sinter deposits	Can exist in conjunction with models 1 or 2

2.3. Gravity Interpretation

In this section, we present a series of gravity maps along with interpretation. Much of this interpretation is focused on what information the data reveals about the starting structural models.

2.3.1. Gravity maps

A number of maps were created using the gravity data. Bouger maps were created using interpolation methods. Interpolation creates data between existing data points by fitting a surface. we chose the kriging method to do interpolation. Kriging has the benefit over other interpolation methods because it uses trends in the data. Issues with interpolation come from under sampling of data. In the gravity method a datum is affected by a sum of all effects on that point. Small scale nearby bodies can cause shifts to a datum that are not related to larger features. This can skew the interpolated values.

2.3.1.1. Bouger gravity

A map of the corrected gravity data using a Bouger background density of 2.35 was created in Golden Software Surfer using kriging interpolation. Data west of 456500 easting was not used in interpolation, due to its sparse sampling which may lead to spurious results. Figure 2.17 shows the interpolated corrected gravity data of Jersey Valley plotted on the imagery. For this and further maps of gravity data station spacing in the north 1.5 km is sparse. Because of this there should be little trust put in interpolation in this region and conclusions in this region should be made with much reservation! The main apparent feature in the Bouger gravity map is a large-scale gravity low in the northwest of the survey area, and a general decrease in gravity to the west of the valley. One feature that does stand out over the background is as an anomalous area of low gravity marked with the blue ellipse in Figure 2.17.

The Bouger map gives little conclusive information regarding the starting models. This is because the long wavelength trend dominates the signal. Gravity contour lines do follow the shift in displacement as would be consistent with model 1, but the southern anomalous low area contradicts model 1. A small eastward shift in gravity contours around 4447500 northing from 457500 to 459000 easting shows a gravity low consistent with model 3, but this is too small to make conclusions. Because the large scale trend dominates many of the features of interest further analysis is needed to make valid interpretations from the gravity data. In the next few sections the interpretation tools discussed earlier in this project are used to accentuate features of interest.

2.3.1.2 Regional gravity

Figure 2.18 shows the regional gravity trend as calculated by a quadratic polynomial fitting of the gravity data. A best fitting linear map was also calculated, but in my opinion does not show the regional trend as well as the quadratic fitting. The main feature of the regional map is the gravity low to the northwest. The more than 30 mGal variation in regional gravity shows it dominates the signal.

2. 3.1.3. Total horizontal gradient of gravity

A total horizontal gradient map was created using the gradient function in Golden Software's Surfer program. The calculation is consistent with equation 2.5. The total horizontal gradient map is presented in Figure 2.19 with the data locations plotted. The data locations are plotted to show areas where data is sparse and conclusions are to be considered less trustworthy. Figure 2.20 presents the total horizontal gravity map without the data points. The range-front faults are characterized by high gradients as expected, and an area of high gradient exists near the mapped valley fault.

The total horizontal gradient map gives us valuable information about our models. For model 1, the Augusta Range-front Fault and Valley Fault would be connected which should lead to a continuous high gradient between the two faults. From the map there is a clear discontinuity between the two high gradient trends. In addition, if model 1 is correct at the north of the Valley Fault displacement decreases and the fault is covered deeper under fill material. Both these effects would lead to less of an effect on gravitational acceleration and thus lead to a lower gradient. This did not occurred which puts further doubt on model 1. Instead the continued high gradient to the north of the Valley Fault suggests significant displacement consistent with model 2. A small east west high gradient is located at the location of the hypothesized graben from model 3. This is not well pronounced as it is subdued by the high gradients from the north striking faults which have large displacements and large lateral extent.

There are some other notable features in the total horizontal gradient map. The extent of high gradient associated with the Augusta Range-front Fault suggests this fault's northern limit was mapped correctly. The high gradient associated with the Valley Fault contradicts the fault map, and shows a more northeasterly trend. The map shows no strong indication of the two unnamed faults mapped between the Fish Creek Range-front fault and the Valley Fault.

2.3.1.4. Residual gravity

Figure 2.21 shows the residual map created from quadratic polynomial fitting. The map was calculated by subtracting the regional gravity from the total gravity. The maps shows many of the same features that are visible on the gradient map. There is a clear discontinuity between the gravity lows associated with the Augusta Range-front Fault and the Valley Fault. This suggests model 1 is incorrect. The large residual low at the north of the Valley Fault also contradicts model 1 because displacement should decrease to the north, instead this low is consistent with model 2. A small residual gravity low does exist in the region where model 3 suggests an east west fault. Similar to the gradient map, the residual low associated with the Valley Fault suggests a more northeasterly trend than was mapped. Figure 2.22 shows the residual map created using the finite element approach. This approach leads to similar results as the polynomial method. Both residual maps show no evidence about the unnamed short north trending fault within the valley, but do show some indication of the unnamed east northeast trending fault.

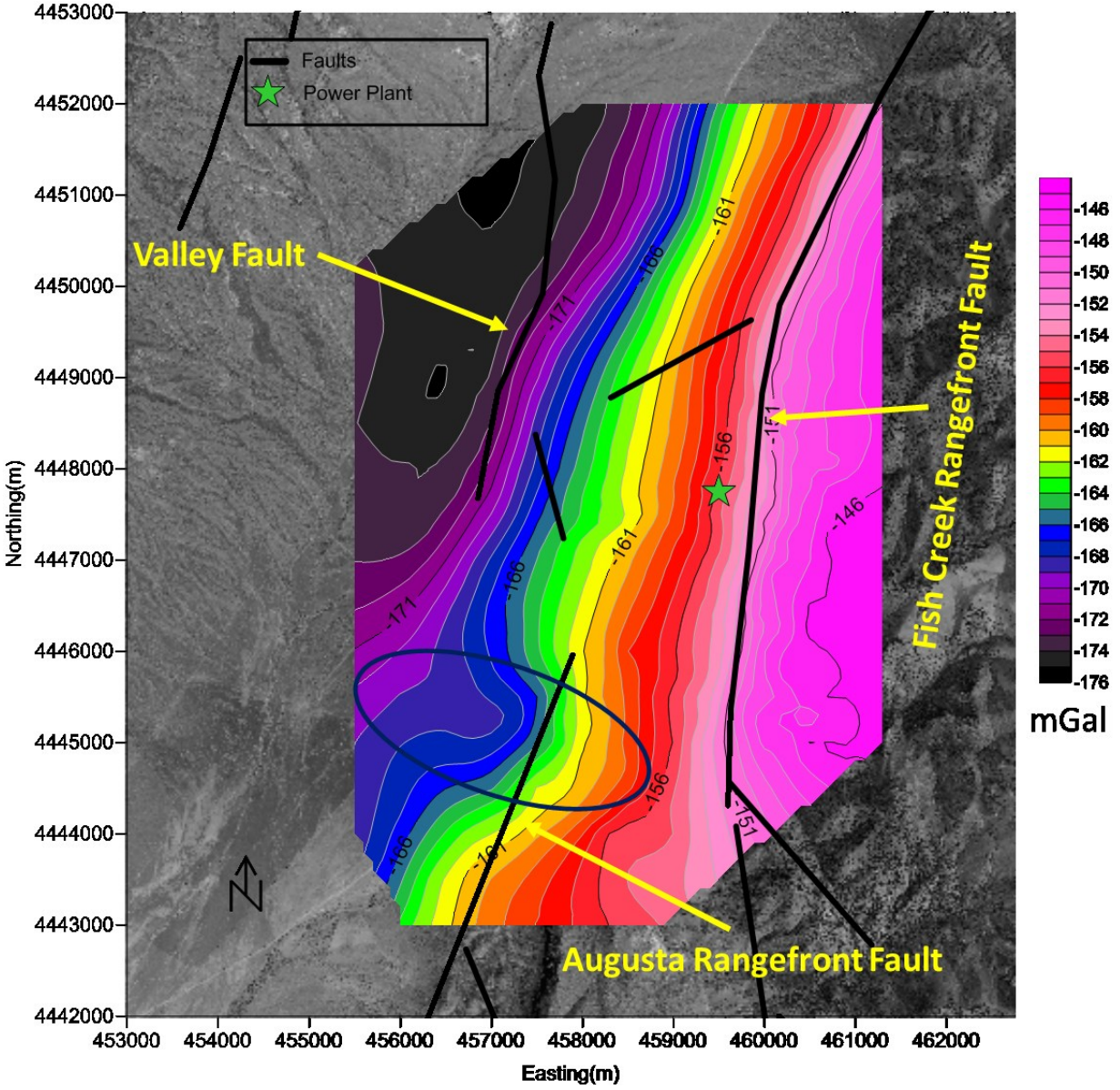

Figure 2.17. Bouger corrected gravity map of Jersey Valley data plotted over satellite imagery. A background density of 2.35 used to calculate terrain corrections. Faults and fault names from Figure 2.15 are included for interpretation purposes. The blue ellipse shows an anomalous area of low gravity.

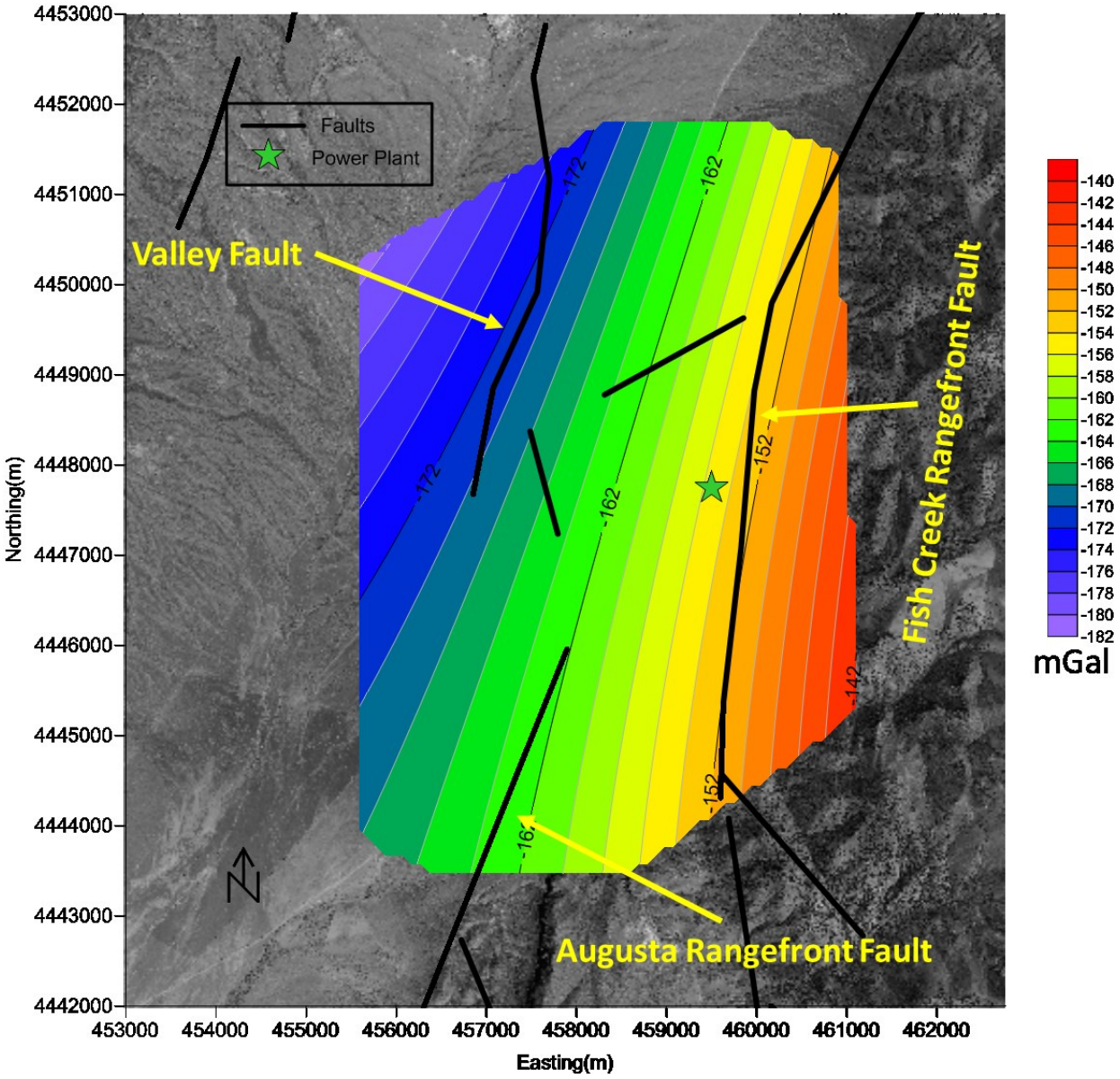

Figure 2.18. Regional map of the gravity data using the polynomial method within Jersey Valley. The map is plotted on satellite imagery. Mapped and named faults are included for interpretation purposes.

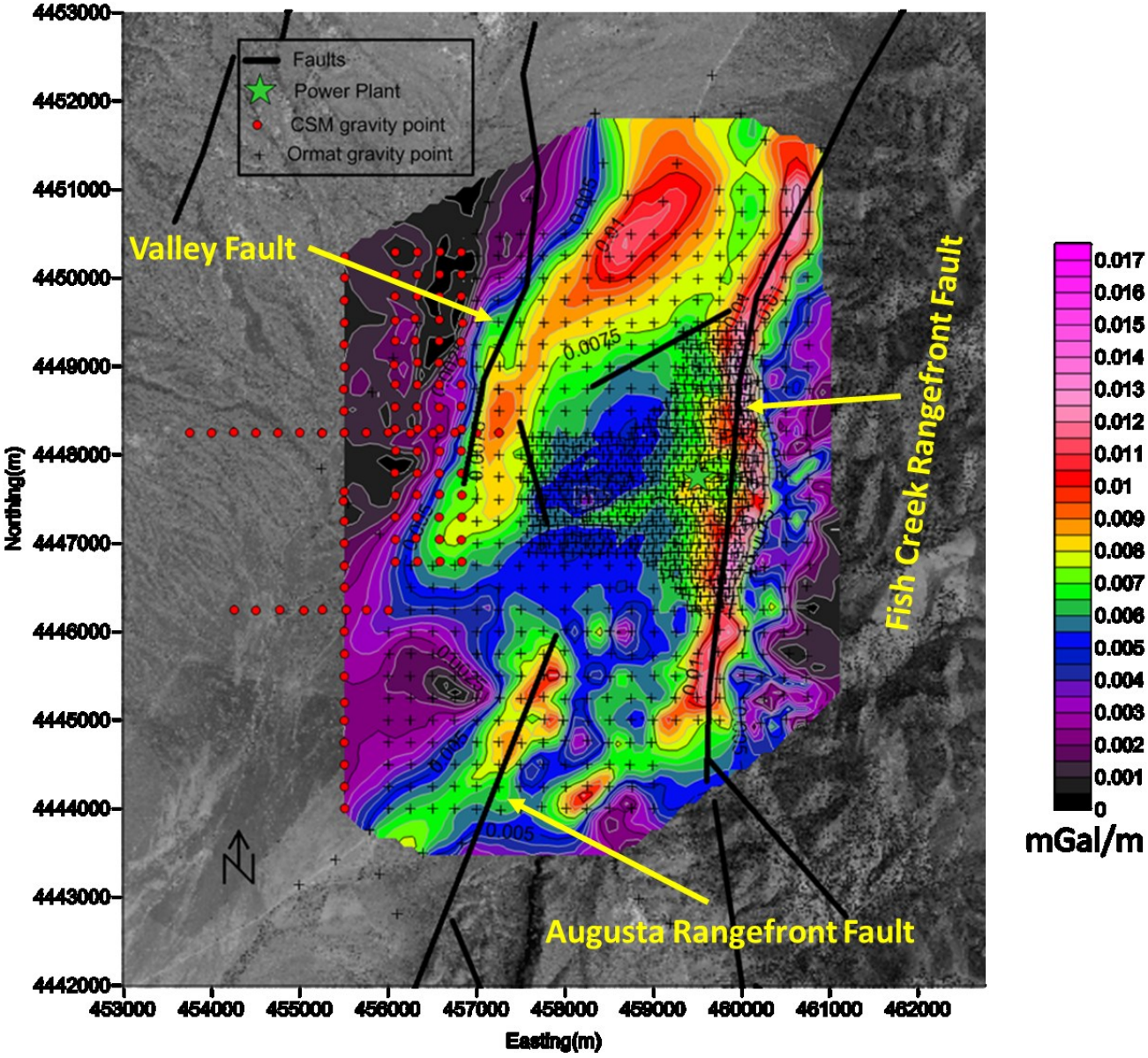

Figure 2.19. Total horizontal gradient map of the gravity data within Jersey Valley, plotted on satellite imagery. Data points included, mapped and named faults are included for interpretation purposes.

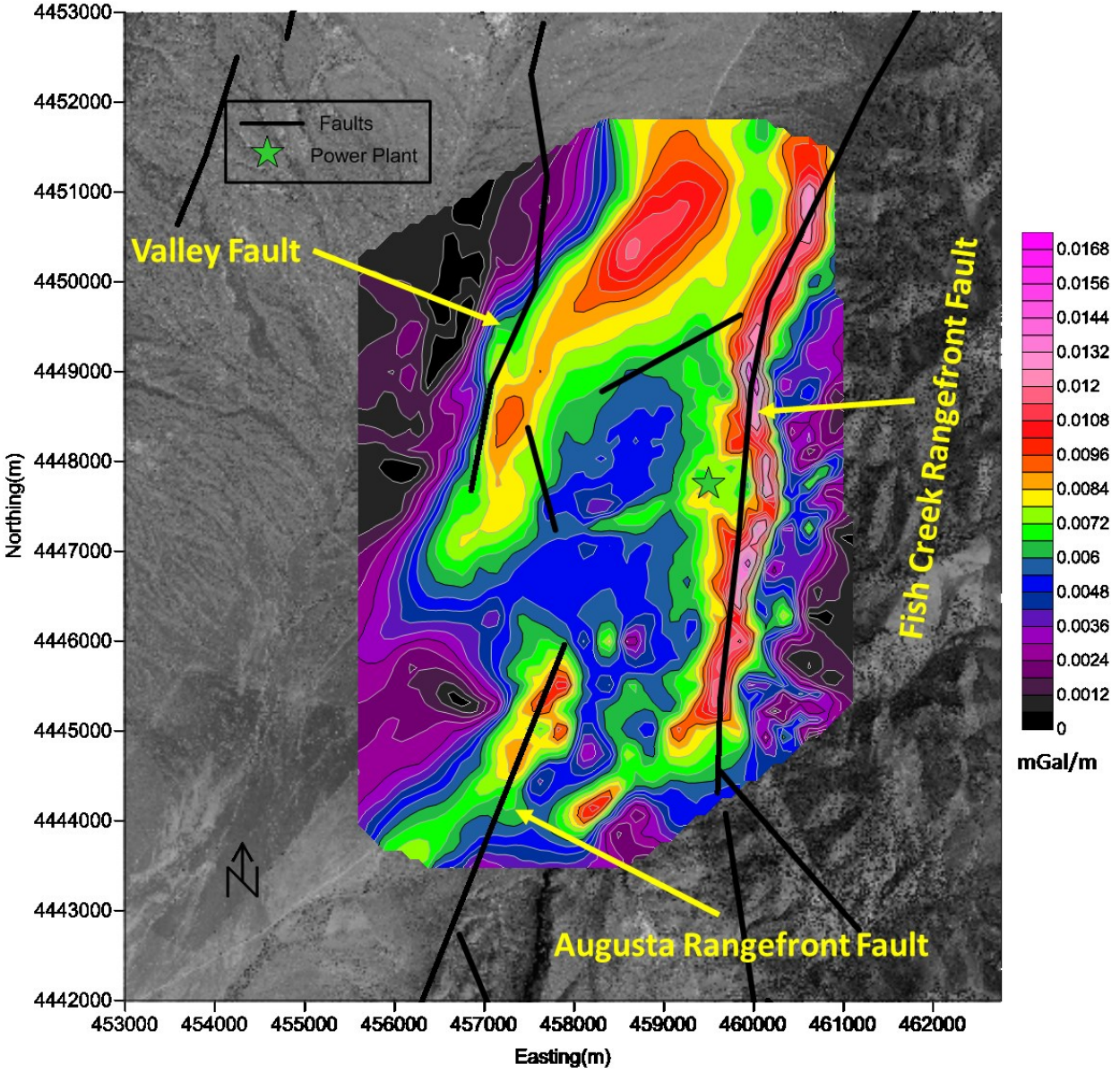

Figure 2.20. Total horizontal gradient map of the gravity data within Jersey Valley, plotted on satellite imagery. Mapped faults are included for interpretation purposes.

2.3.2. Gravity profile modelling

To gain further insight from the gravity data, models for two transects were created. The model transects are oriented east west, which is approximately perpendicular to the orientation of the range-front and valley faults. Data were placed into the available the 2.5D modelling program and a simple model created. The results and locations are seen in Figure 2.23 along with interpreted faulting. The starting model was created using geologic knowledge, gravity maps, and well information. The total horizontal gradient and residual gravity maps along with the profile data were used to approximate the location of the valley fault. Well information was used to determine the initial layer thickness.

The true geology is more complex than the model used but due to limited knowledge of layer thickness within the valley a simple model was preferred. Modelling was performed for one transect with additional constant thickness layers, which is more consistent with the real geology. Results of this modelling produced variations in the thickness of layers, but the relative change between the range-front fault and valley fault remained similar. The simple two layer model was decided sufficient to answer the questions presented here. Schwering and Karlin (2012), present densities for geologic units in Dixie Valley, the valley fill density is 2.07 g/cm^3 and pre-Tertiary rocks are 2.67 g/cm^3. These values were used for the models in Jersey Valley. Because the real geology is three dimensional, it is important to look at where the two dimensional modelling assumption fails. The gradient and residual map show east west features near the modelled locations, also the overall trend of the Valley Fault is not perfectly north south. These effects may affect the profile models, but the north south faulting systems dominate the gravity signal. Because these features dominate the signal the two dimensional modelling should be valid.

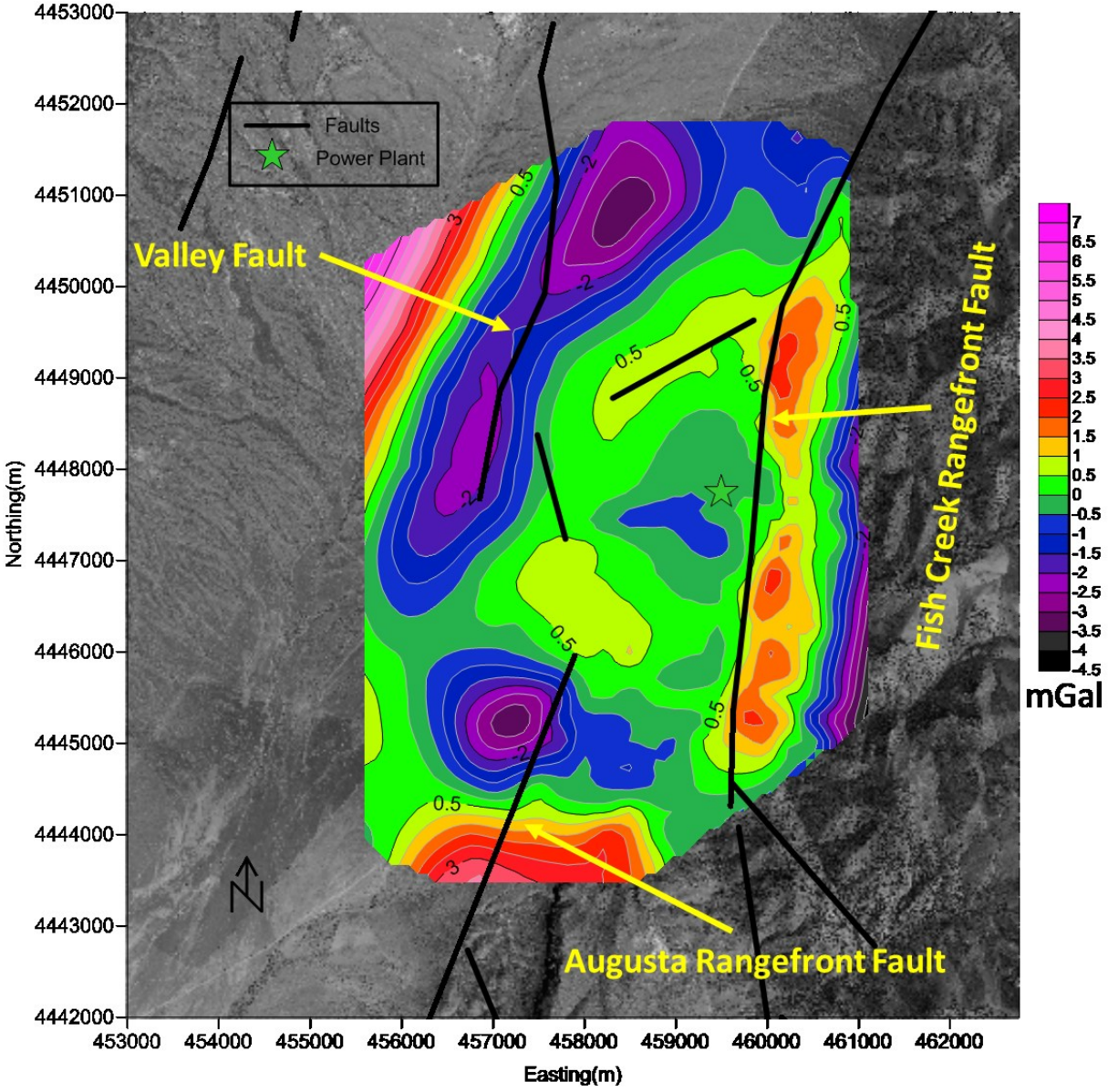

Figure 2.21. Residual map of the gravity data using polynomial method within Jersey Valley. The map is plotted on satellite imagery. Mapped and named faults are included for interpretation purposes.

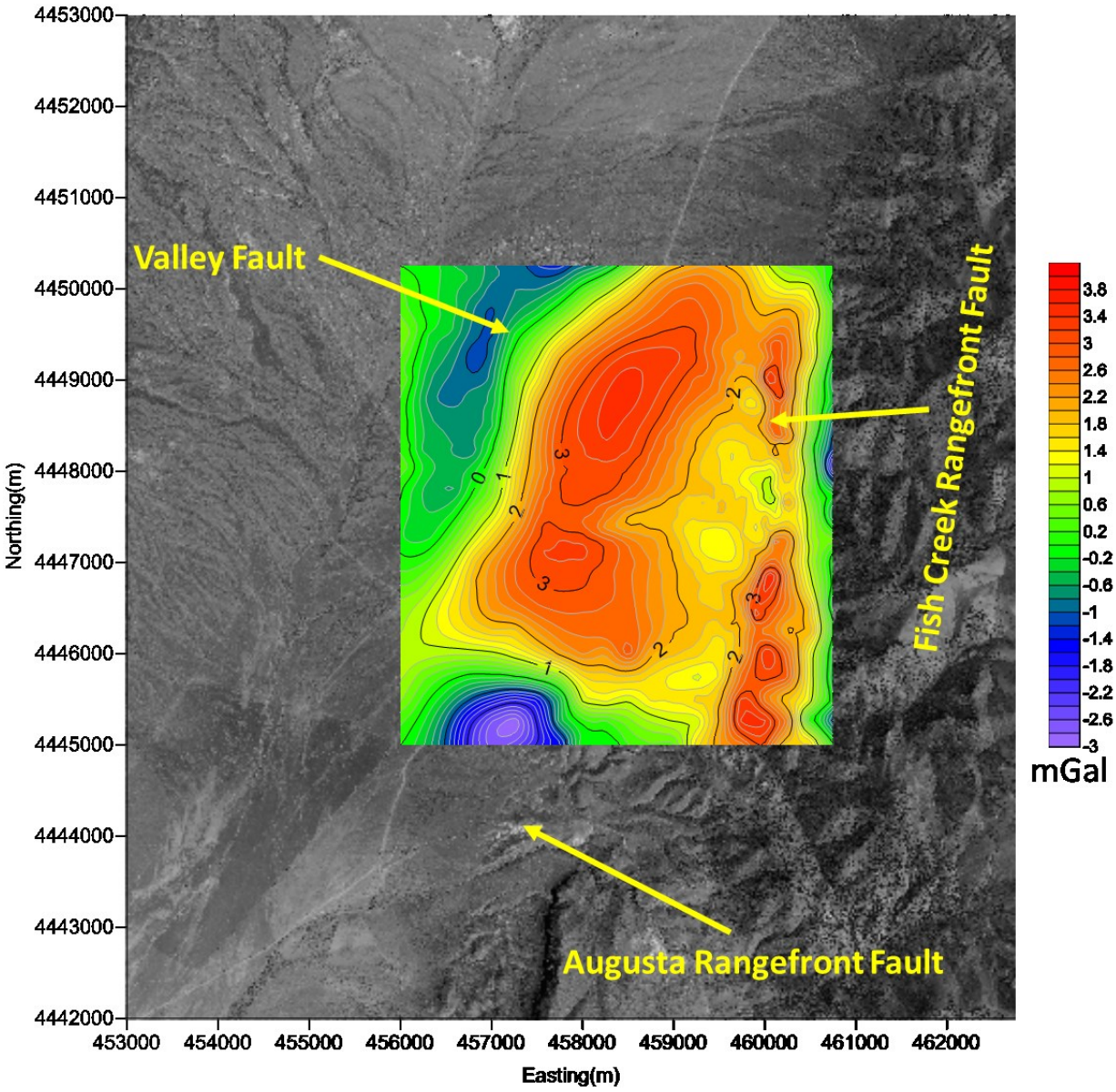

Figure 2.22. Residual map of the gravity data using finite element method within Jersey Valley. The map is plotted on satellite imagery. Mapped and named faults are included for interpretation purposes.

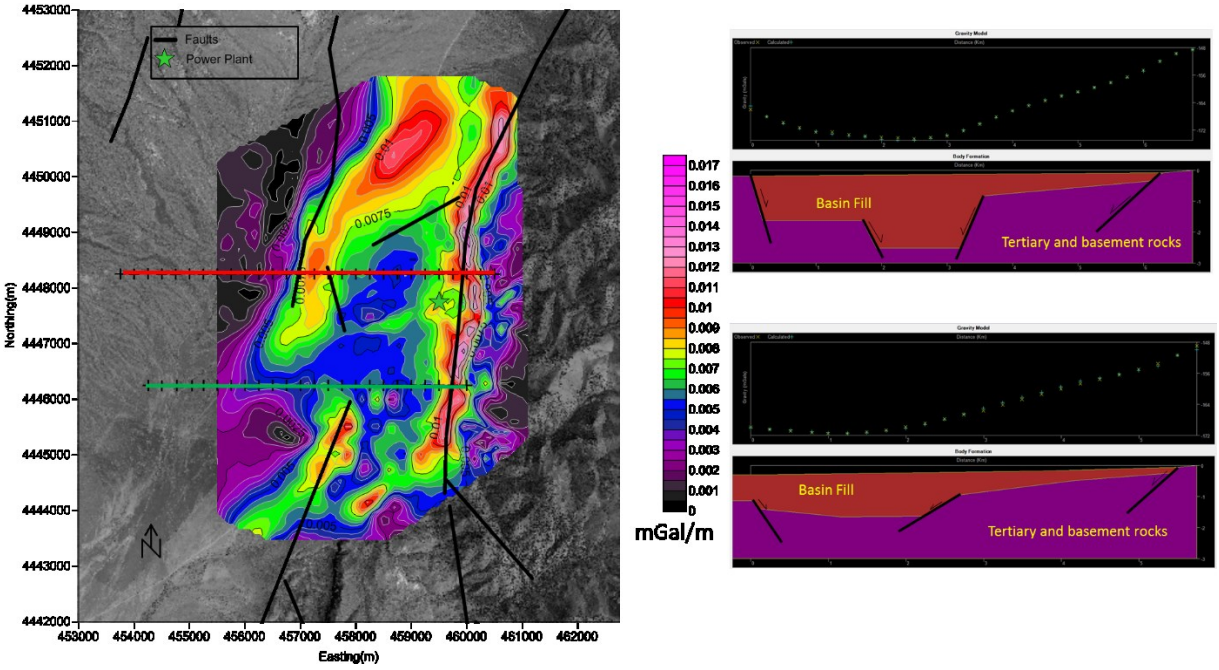

Figure 2.23. Map of locations of 2 gravity profile models on the left and the corresponding models on the right. The top model corresponds to the gravity data located along the locations designated by the red line, and the bottom model is associated with the green line. Total horizontal gradient map included.

Results of the modelling clearly show the range-front and valley faults. The model for the north line is consistent with model 2 showing that the Valley Fault has a throw of more than 1.5 km. modelling of the southern line shows that the steepness and height of displacement towards the center of the valley decreases significantly relative to the north model. The relative displacement between the two models is a strong piece of data against model 1, because displacement along valley faults would decrease to the north.

2.3.3. Conclusion

A lot of interpretation has come in this section. To sum up what was discovered about the starting models, table 3.1 is updated with the new information. The updated table is presented as Table 3.1. Additional interpretation suggest the Valley Fault trends north northeast at its northern extent and that there is an east west feature towards the south of the survey area.

Table 3-3. Table of models and their supporting data, updated with gravity data.

Models	Key Elements	Supporting data	Notes	Supporting gravity data
1	Relay ramp between Fish Creek Range-front Fault and Augusta Mountain Range-front Fault	Fault map DEM	Competing against model 2	
2	Valley fault/faults with significant displacement	Fault map	Competing against model 1	Residual gravity maps Total horizontal gradient Map Profile modelling
3	An east west fault, near power plant	Surface sinter deposits	Can exist in conjunction with models 1 or 2	Total horizontal gradient and residual maps

2.4. Magnetotelluric interpretation

In this section, we analyze the magnetotelluric data. Due the extensive data set not all data are presented, but instead only data that may give information on testing the structural models, or data which relates to areas of particular interest. Simple apparent resistivity and phase curves are examined, as well as profiles, polar diagrams, and results from the one dimensional modelling program. Before examining the data further we note that in the CSMGP surveys x corresponds the north direction and y the east. The data obtained from Ormat Technologies Inc. have the opposite convention.

2.4.1. Apparent resistivity and phase curves

In order to test model 1, apparent resistivity and phase curves for sites along a line perpendicular to the supposed relay ramp structure were compared. Figure 2.24 shows the locations of 3 magnetotelluric sites provided by Ormat Technologies Inc. and their associated apparent resistivity and phase curves for the yx component. Data was chosen along this line as it is located away from the Valley Fault and range-front fault, and except at low frequencies should see little effect from these structures. The site locations were chosen to represent variation from north to south. If model 1 were correct than as we move south the thickness of the alluvium. should decrease. This decrease would lead to a shift in the apparent resistivity curves at the rise

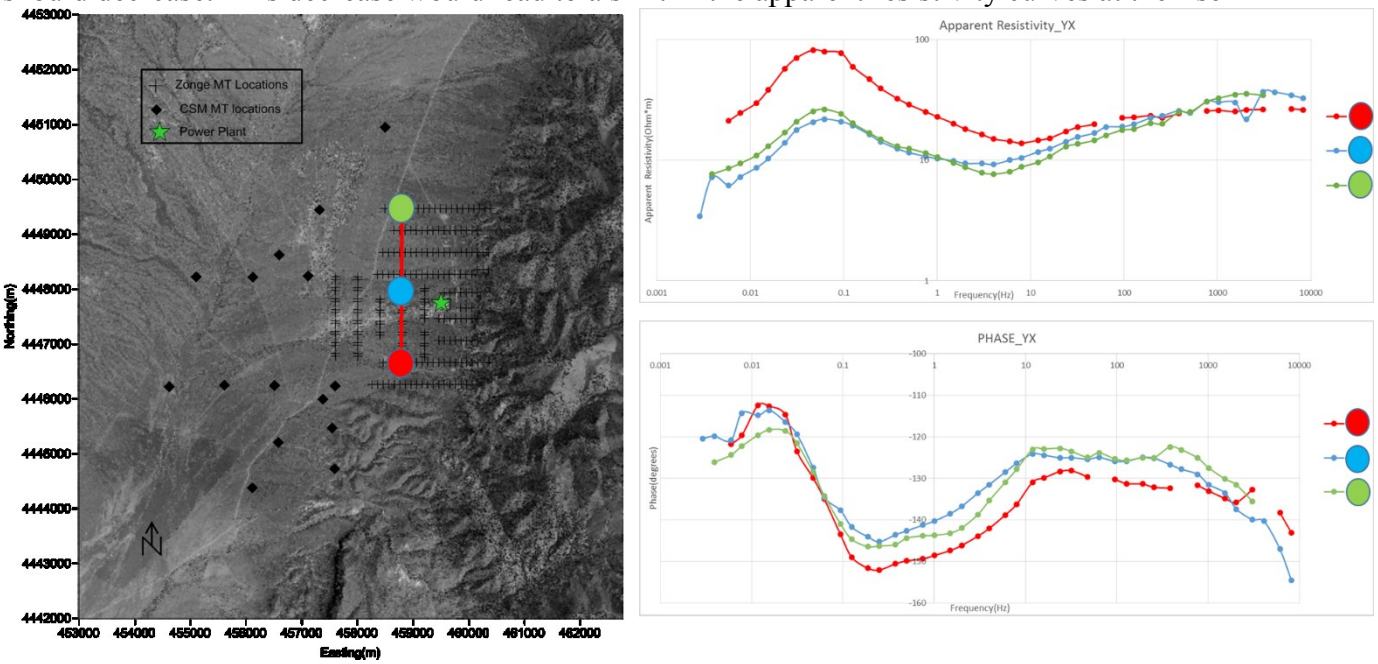

Figure 2.24. On the left hand side of the image satellite imagery of Jersey Valley with magnetotelluric sites plotted. The location of three sites correlating to the three yx apparent resistivity and phase curves shown on the right hand side of the image.

occurring between 2 and 10 Hz. The data does not show this shift. The yx component of resistivity was chosen because it is parallel to the bulk structure of the area and should see the least effect from this structure. Some shift still occurs for the curve associated with the southernmost site. This shift is likely related to the tertiary units which reach the surface near this area. Because of this shift the phase curves are also examined as they show no effect from static shift. Phase curve examination again shows the change associated with the more resistive layers occurs at a frequency of about 10 Hz throughout the north to south sites, this suggests the depth to the resistive layers is consistent through the sites.

Figure 2.25 shows the location and station numbering for magnetotelluric sites gathered on the CSMGP magnetotelluric surveys and for a couple of sites from the Ormat Technologies Inc. data set. This map was used to associate site locations through the remainder of this section. Figures 2.26 and 2.27 show the apparent resistivity and phase curves of sites labelled 2000 through 2002. For the data gathered by CSMGP surveys a measure of the quality of the data is obtained through coherency values. According to Friedrichs (2007), the coherency displayed in the Mapros data window represents a correlation between the E and H fields. Real signal should be correlated between the E and H fields, but noise may not be. In Figures 2.25 and 2.27 frequencies where coherencies in x direction are considered poor are highlighted in yellow and highlighted in blue for poor y coherency. Error bars plotted on the curves represent standard deviations.

The xy curves of the 2000 sites show an increasing resistivity occurring around 20Hz. The increase around 20Hz could be caused by a resistive body, but the yx curves deviate towards a more conductive trend. This suggests a geoelectric structure of at least two dimensions. Because the increasing resistivity occurs at approximately the same frequency for all the 2000 sites the associated geologic feature is likely oriented approximately east west. This feature is likely more conductive than the region under the 2000 sites. Unfortunately the shift makes it difficult to determine much about our starting models from these curves. Some modelling reveals further information and we present the modelling later in this section.

Figure 2.28 and 2.29 show the apparent resistivity and phase curves across the sites numbered in the 1000s. The xy components of data indicate a geology with at least four layers of different resistivity. All the xy curves are similar suggesting there is either little structure in the east west direction, or that any such structure is parallel to the line of acquisition. The yx component of the apparent resistivity and phase curves show a more complicated behavior. The difference between the xy and yx curves shows the geology is at least two dimensional, and because these differences occur at frequencies above 10Hz structures are fairly shallow. Yx curves for sites 1000, 1002, and 1003 show similar behavior to each other, whereas the site 1001

curve displays a very different behavior. Without other information it is difficult to make many conclusions based on these curves. Neither component shows a significant shift in the thickness of layers to the west.

2.4.2. Profiles

To test model 3, profiles of the magnetotelluric apparent resistivity along a couple north trending transects are plotted. Figure 2.31 shows the apparent resistivity profiles of two south to north lines at 24Hz. This corresponds to skin depths between the 1 and 2 km range. The most prominent feature in these profiles is the more conductive region located at a northing of approximately 4447500. Both yx and xy profiles show this feature. The yx component of the profiles exhibits a sharp change, suggesting it is the TM component. The xy component is also affected, but more gradually suggesting this is the TE component. The conductive region shown in the profiles is consistent with model 3 of an east trending graben in this location.

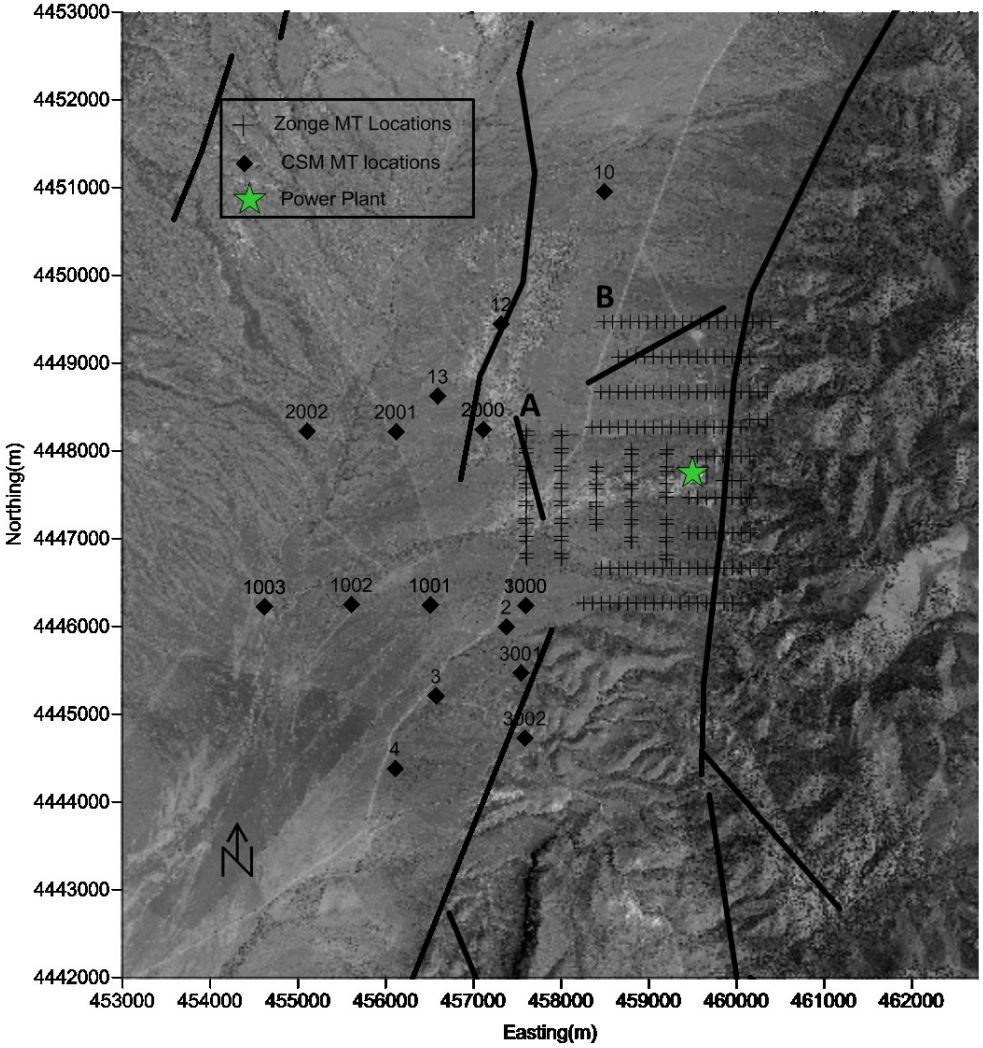

Figure 2.25. Location of the magnetotelluric sites in Jersey Valley with labels corresponding to sites that are further examined.

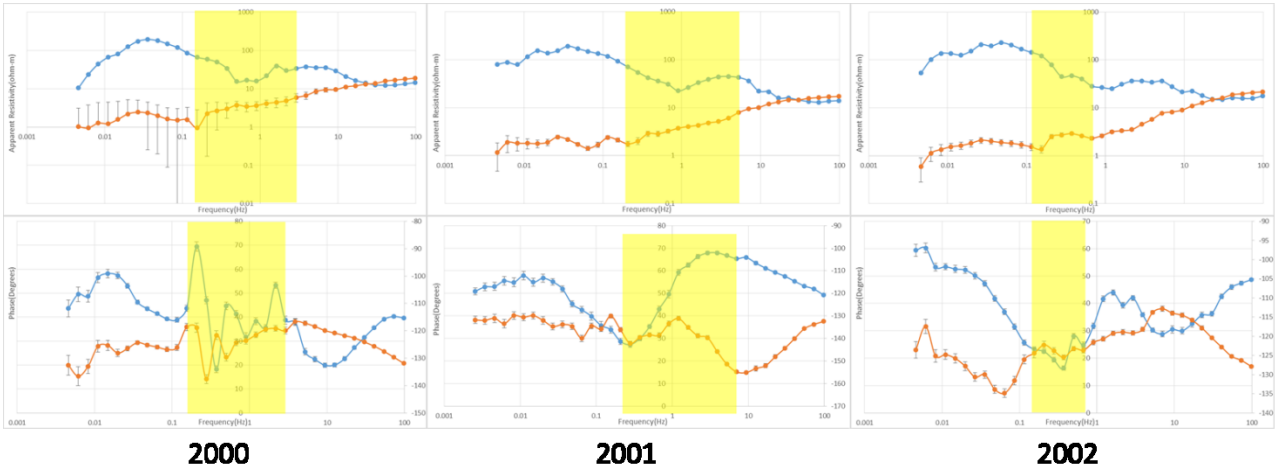

Figure 2.26. Apparent resistivity and phase curves for sites 2000, 2001, and 2002. Highlighted areas correspond to areas of poor coherency, error bars are standard deviations. Blue curves are xy components and red curves are the yx component.

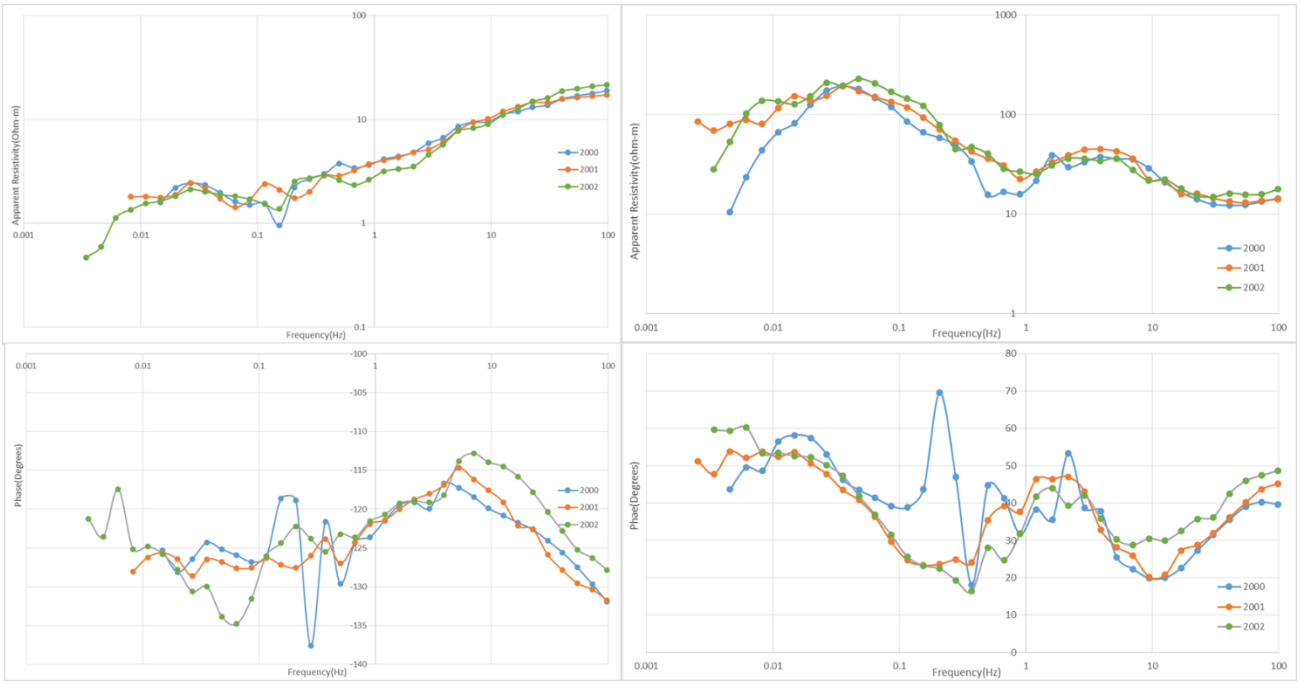

Figure 2.27. Apparent resistivity and phase curves for sites 2000, 2001, and 2002. Values for sites plotted together for comparison. The left hand side of the image is the yx components and the right hand side of the image is the xy components.

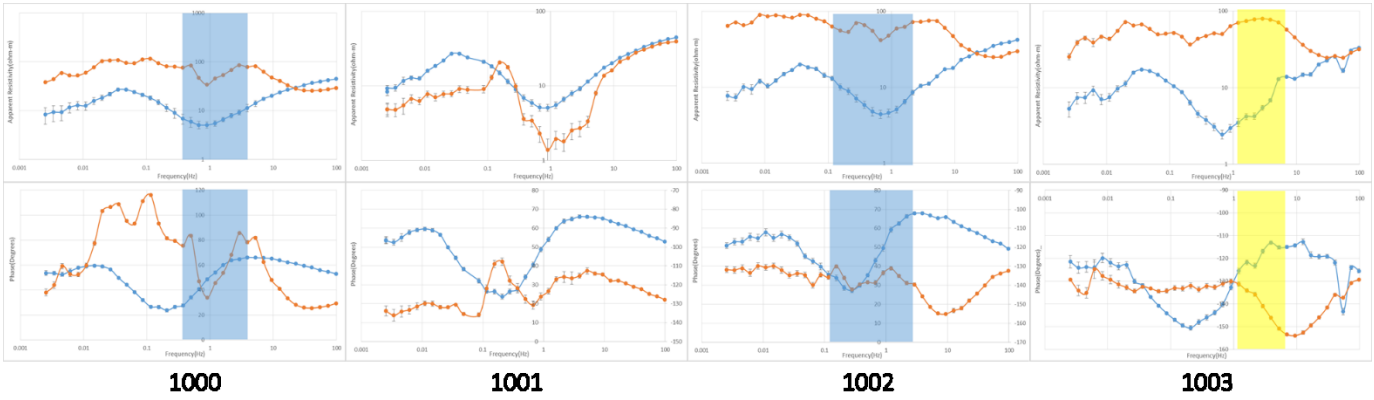

Figure 2.28. Apparent resistivity and phase curves for sites 1000, 1001, 1002, and 1003. Highlighted areas correspond to areas of poor coherency, error bars are standard deviations. Blue curves are xy components and red curves are the yx component.

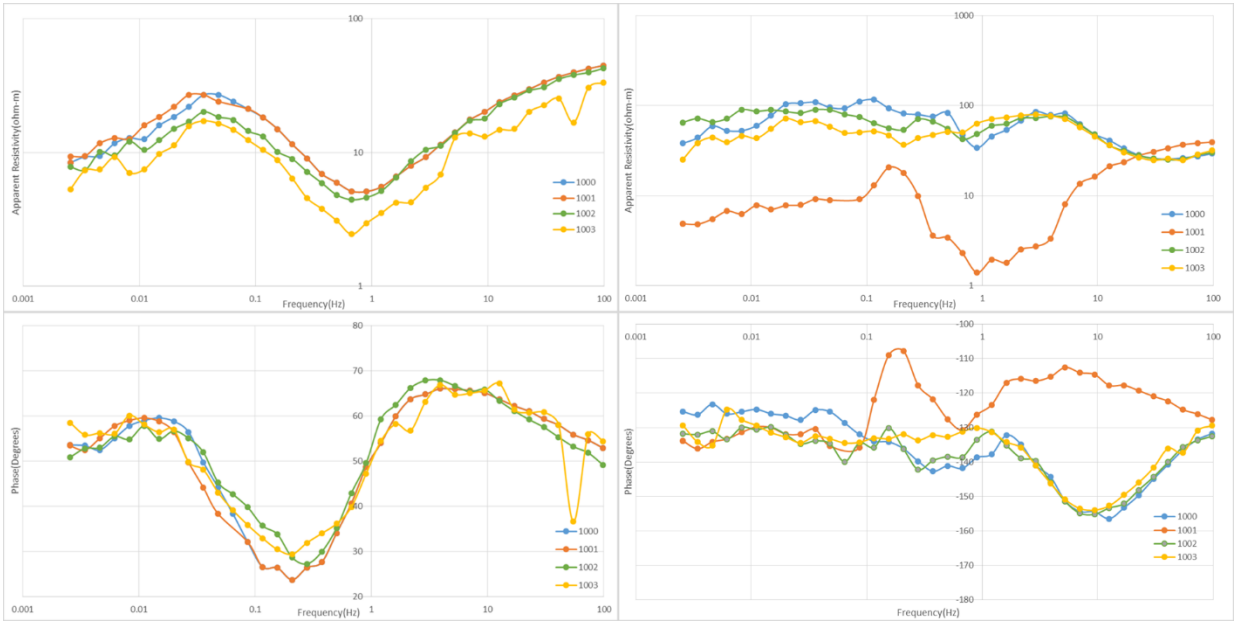

Figure 2.29. Apparent resistivity and phase curves for sites 1000, 1001, 1002, and 1003. Values for sites plotted together for comparison. The left hand side of the image is the yx components and the right hand side of the image is the xy component.

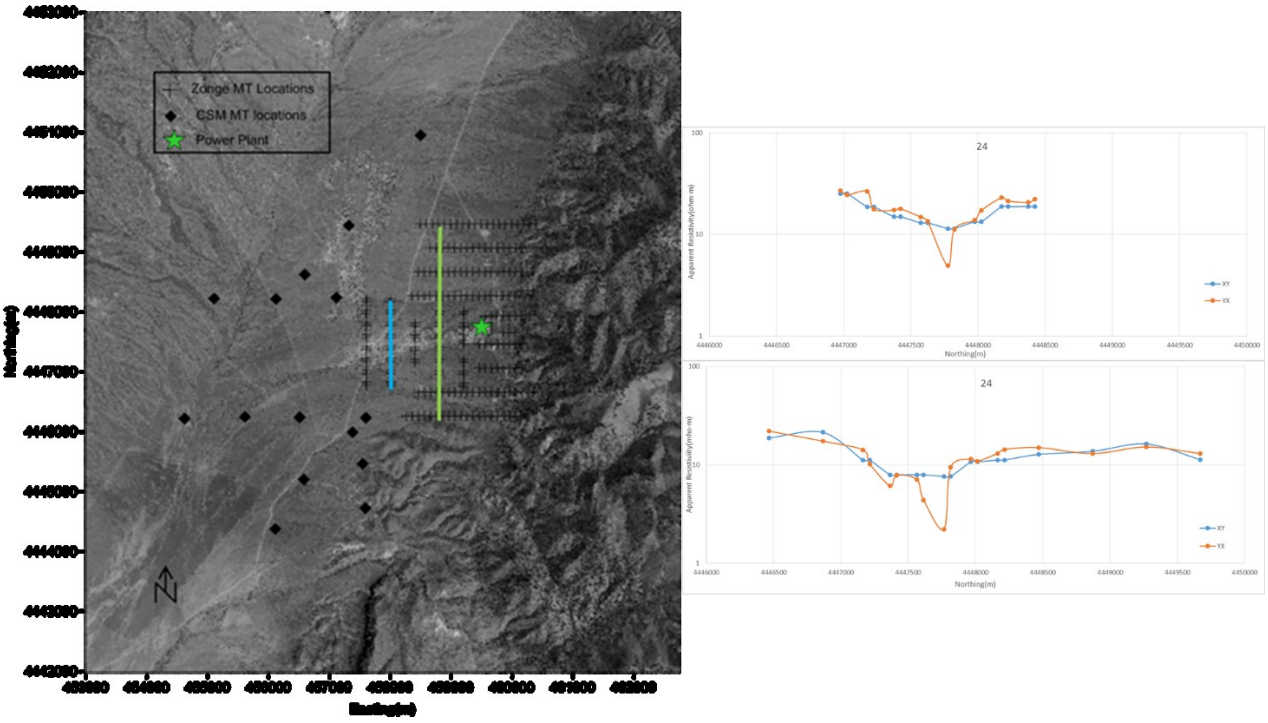

Figure 2.30. On the right hand side of the figure are two apparent resistivity profiles of yx apparent resistivity. The left hand side of the image shows the location of the two profiles, the blue line relates to the top of the two images and the green relates to the bottom profile.

2.4.3. Polar diagrams

Due to the extensive sites and range of frequencies polar diagrams for only a few sites and frequencies are presented. Figure 2.32 shows impedance polar diagrams for the 2000 and A sites at 1.6Hz. The diagrams show an increased impedance of the 2000 sites compared to site A. The minimum of the off diagonal impedance values on the 2000 sites are approximately equal to the impedance value of site A. This suggests that the increased impedance on the 2000 sites is related to a two dimensional vertical conductivity variation. The orientation of the diagrams suggests that this feature is approximately east west. Polar diagrams for the 2000 sites for lower frequencies exhibit a similar pattern while indicating a more three dimensional conductivity structure.

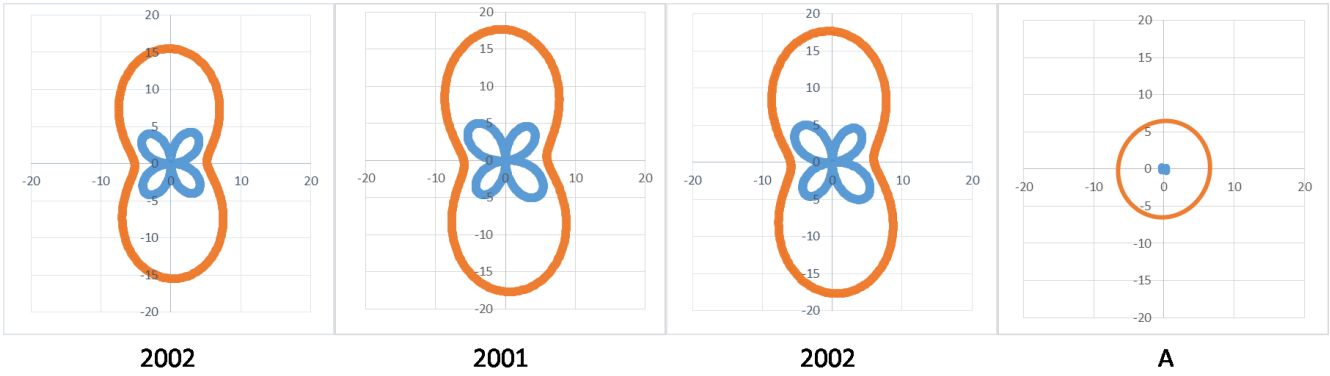

Figure 2.31. Impedance polar diagrams for sites from left to right 2002, 2001, 2000, and A. Diagrams represent impedances information at a frequency of 1.6 Hz. The red line is the Z_{xy} component (CSM convention) of the impedance tensor and the blue line is the Z_{xx} component of the impedance tensor.

Figure 2.33 shows impedance diagrams for the 1000 sites. Figure 2.33a shows the diagrams at 9.4 Hz. These diagrams suggest two dimensional structure either trending east or a series of north trending features. Due to the consistency of the Z_{xy} component, we suspect they are indicative of an east trending feature. Figure 2.33b shows impedance polar diagrams for the same sites at frequency of 0.086 Hz. At 0.086Hz there is some indication of two dimensional structure, but there are lots of three dimensional effects, shown most clearly in the Z_{xx} component. We cannot make many conclusions regarding our models from these diagrams. The best conclusion we can make is that there seems to be some shallow east west feature and a complex geoelectric structure deeper.

Figure 2.34 shows polar diagrams for sites 10 and B. The impedance diagram associated with site 10 points to a two dimensional geoelectric structure whereas the diagram for site B suggests a close to one dimensional structure. The maximum of the impedance for site 10 is approximately equal to the magnitude of the impedance at site B. This suggests site 10 is on the conductive side of a north northeast trending feature.

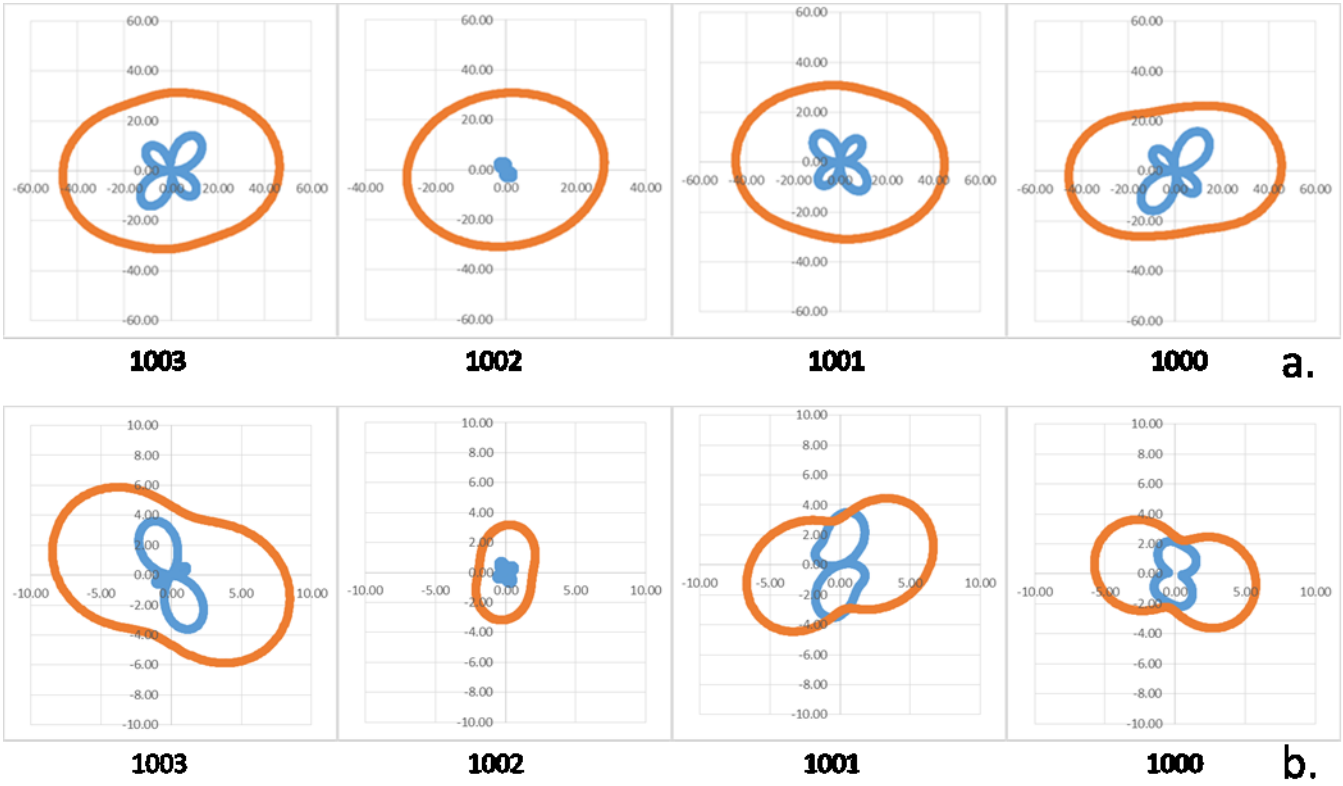

Figure 2.32. Impedance polar diagrams for sites from left to right 1003, 1002, 1001, and 1000. Diagrams in 4.9a represent impedances information at a frequency of 9.4 Hz and in 4.9 b represent impedances for 0.086 Hz. The red line is the Zxy component (CSM convention) of the tensor and the blue line is the Zxx component of the impedance tensor.

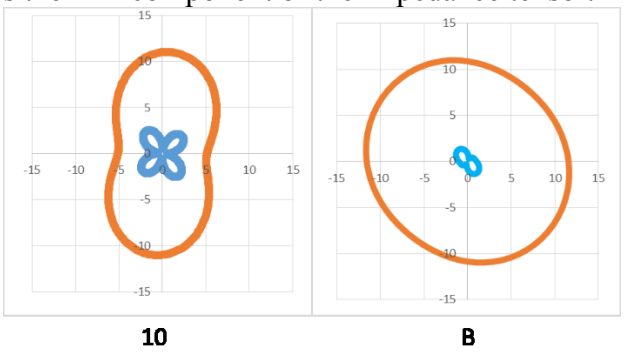

Figure 2.33. Impedance polar diagrams for sites 10 and B, diagrams are for a frequency of 4Hz. The red line is the Z_{xy} component (CSM convention) of the tensor and the blue line is the Z_{xx} component of the impedance tensor.

2.4.4. Modelling

Because the polar diagram for site 10 suggests the site is on the conductive side of a north northeast trending feature this implies site 10 is west of the Valley Fault. Some modelling might backup this observation. Figure 2.35 shows one dimensional models created using the information from sites B and 10. The starting values were chosen using background information. Resistivity values for layers in both sites were kept consistent and only the thickness of the layers was varied. The xy component was chosen to minimize effects of structures. It is clear from the two models that there is a significant amount of increased conductive material in site 10 compared to site B. Since the polar diagram suggests the conductivity contrast is not exactly north south there is some question as to whether the increased conductivity region in site 10 is the result of static shift. In order to test this site 10 apparent resistivity and phase curves were rotated according to the strike direction from the polar diagram, and the result was modelled. The rotated site modeling is shown in Figure 2.36 and shows a decrease in the depth of the suggested basin fill, but still significantly more than the site B. These results confirm that site 10 is on the west side of the Valley Fault, and that the Valley Fault has significant displacement even towards the north. This conclusion is consistent with model 2, but inconsistent with model 1.

The one dimensional modelling program allows for a series of sites across a profile to be modelled and plotted in cross section form. To further investigate the Valley Fault a number of sites were chosen for 1D inversion across an east to west transect shown by the orange line in Figure 2.37. TM mode was chosen based on bulk valley structure and should see be least effected from structures. The results of the modelling are shown in Figure 2.38. Some things that are expected can be seen, for example as towards the west there is a general increase in the thickness of the shallow units, up until the western most site. Unexpectedly, the westernmost site shows an unusual resistive layer at a fairly shallow depth. It is possible that this is a one dimensional effect, but it takes uncharacteristic resistivity values to fit this layer. Therefore the resistive shift is likely caused by two or three dimensional effects. The conductive layer beneath this anomalous resistive layer is consistent with sites to the east and suggests significantly thicker fill at this site.

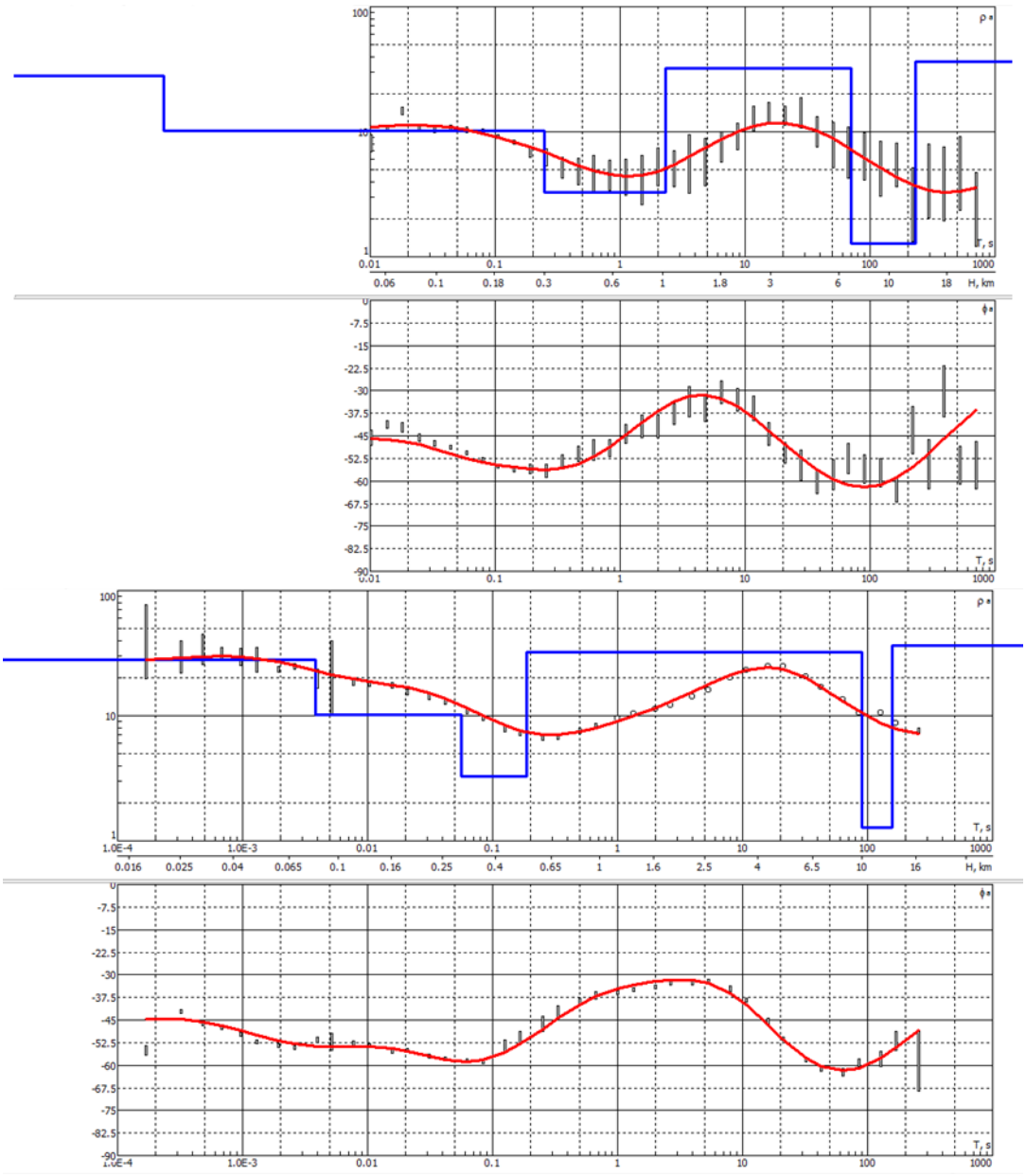

Figure 2.34. One dimensional models created using the modelling program for site 10 on top and sites B on the bottom. The blue line represents the model, the height being related to resistivity and the width being related to layer thickness. The data are plotted as the bars or circles.

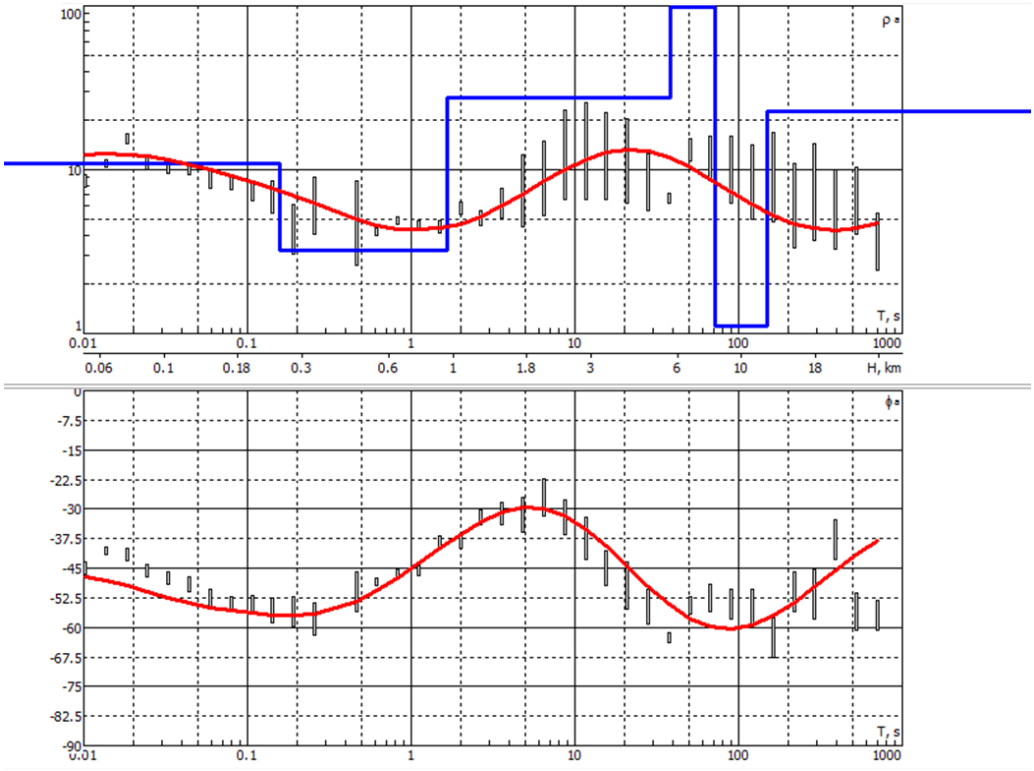

Figure 2.35. One dimensional model for site 10 xy component after rotation.

2.4.5. Conclusions

Apparent resistivity and phase curves along a north south transect perpendicular to the supposed relay ramp structure suggested by model 1, are not consistent with model 1. Apparent resistivity and phase curves for the 1000 and 2000 series of sites give little conclusive information regarding our starting models, but show this region has a complex geoelectric structure. Polar diagrams also show complex geoelectric structure for the 1000 and 2000 series, and suggest an east trending conductivity feature in the top few hundred meters. Polar diagrams from sites 10 and B suggest that the Valley Fault trends to the northeast and site 10 is on the west side of this fault. The one dimensional modelling provides more support for this last conclusion. One dimensional modelling shows an anomalous resistive region seen in the xy curves for the 2000 sites is likely related to a two or three dimensional feature. Conclusions regarding the starting models were added to Table 2.1 and summarized in Table 4.1.

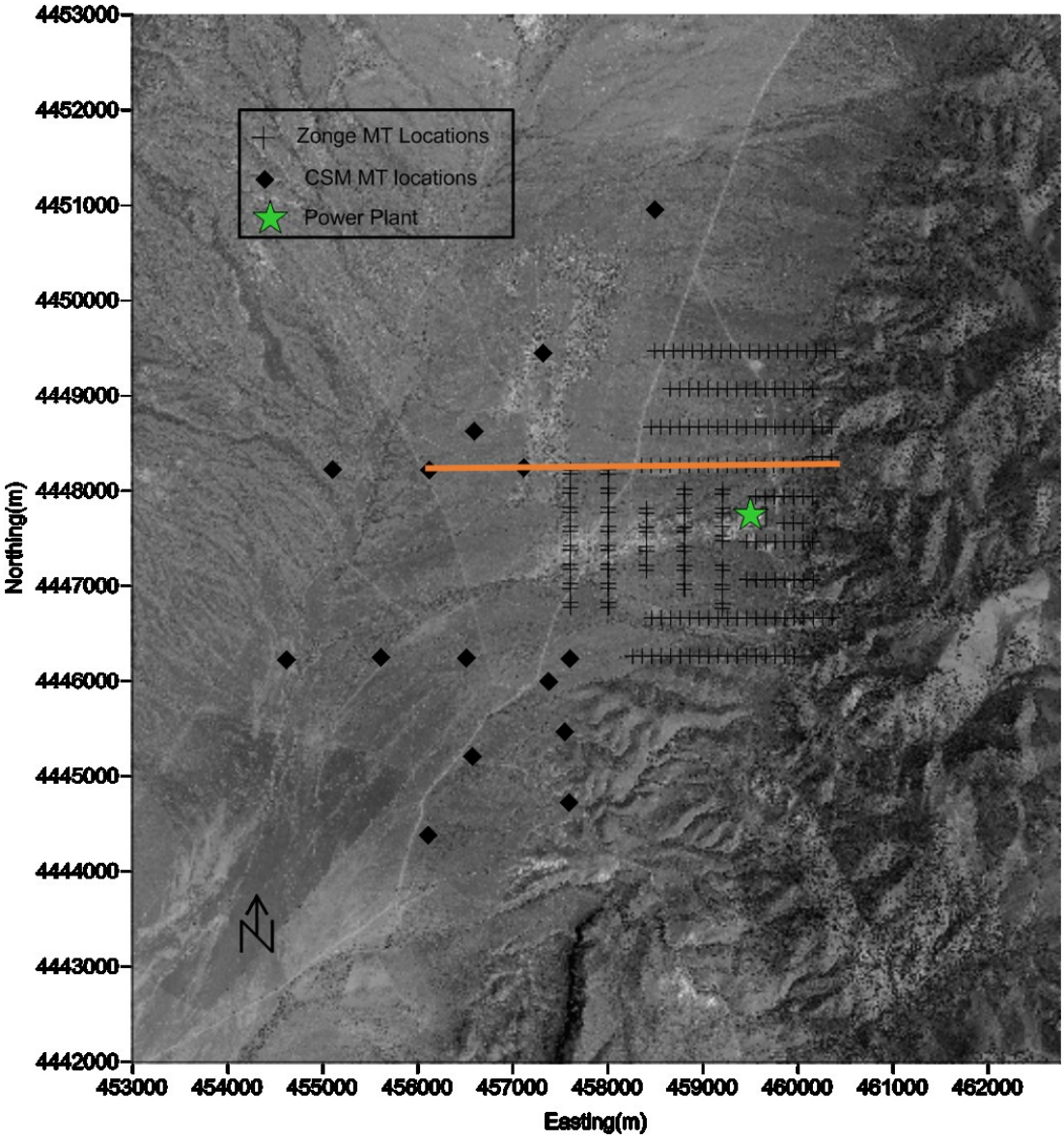

Figure 2.36. Line across which series of 1D-models.

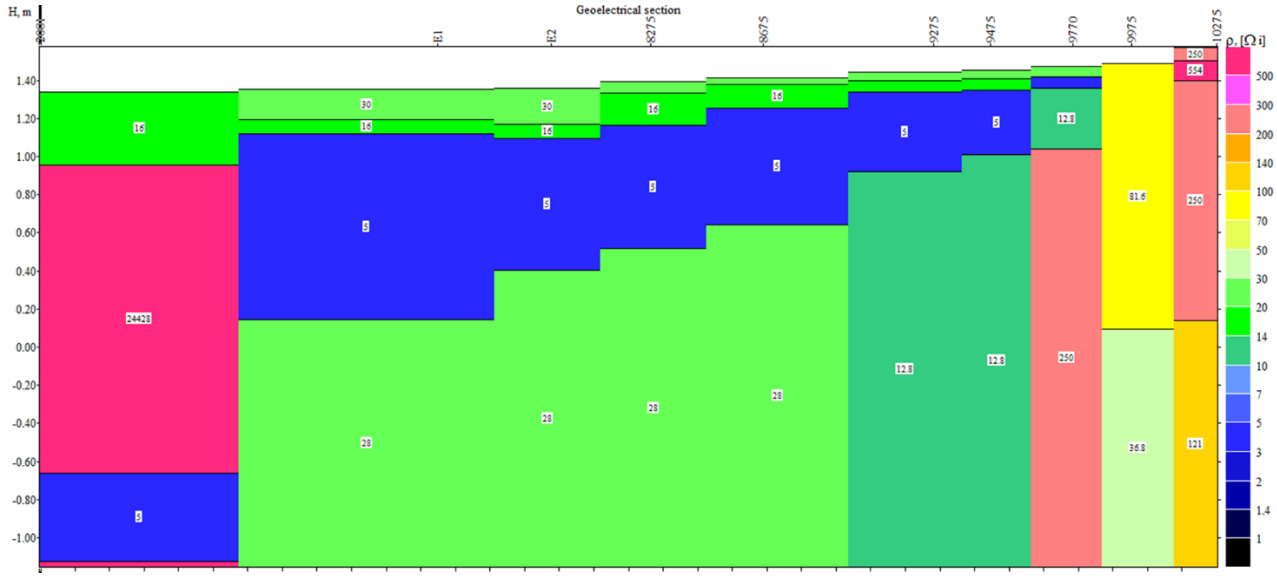

Figure 2.37. Cross section from one dimensional modelling across a transect.

Table 4-4. Table of models and their supporting data, updated with magnetotelluric data

Models	Key Elements	Supporting data	Notes	Supporting magnetotelluric data
1	Relay ramp between Fish Creek Range-front Fault and Augusta Mountain Range-front Fault	Fault map DEM	Competing against model 2	
2	Significant displacement along the Valley Fault	Fault map	Competing against model 1	One dimensional modelling of site 10 Polar diagram from site 10 One dimensional profile model
3	An east west fault, near power plant	Surface sinter deposits	Can exist in conjunction with models 1 or 2	North trending profile plotting

2.5. Integrated interpretation

A lot of information has been presented in the gravity and magnetotelluric interpretation sections. In order to combine this information in a coherent sense, we discuss what the data has concluded about each model. We also introduce a couple of interesting geophysical features discovered from the data analysis. These features might offer valuable information when creating future models.

2.5.1. Model 1

Although the topography is consistent with model 1 most of the data suggests the model is not correct. The total horizontal gradient map shows the high gradient associated with the Augusta Range-front Fault and Valley Fault are not connected as would be expected. Model 1 should show decreased gradient to the north of the Valley Fault, but this does not occur. Gravity residual maps show the similar results and verify the hypothesis that the down-dropped region is west of the Valley Fault. Gravity profile models show that displacement along the Valley Fault to the north is greater than to the south. This is opposite what would be observed if model were correct. Apparent resistivity curves for magnetotelluric data parallel to the supposed relay ramp structure do not indicate increased displacement of the more resistive material towards the , as should occur in the case of model 1. All these pieces of information suggest model 1 is not valid.

2.5.2. Model 2

High gravity gradients in the location of the Valley Fault do indicate a significant displacement along this fault. This is verified with the residual gravity maps. The gravity profile modelling also verifies significant offset along the Valley Fault and suggest this fault has much more displacement than the range-front fault. Magnetotelluric modelling of site 10 vs. site B indicates that there is significant displacement along the Valley Fault. These pieces of information suggest model 2 has validity, although in the case of Jersey Valley the data confirm a single valley fault.

2.5.3. Model 3

Both the total horizontal gradient gravity map and the gravity residual maps do suggest elevated gradient and decreased gravity associated with a feature consistent with model 3. Because the greatest variation in the gravity field comes from displacements along the north northeast trending features the gravity anomalies associated with model 3 are subdued. In order to get a better picture of this feature the residual map was trimmed to focus on the area of interest. This trimmed map is presented in Figure 2.39. The gravity low trending east west is

much clearer in this image. This low is consistent with model 3, although the exact structure is hard to determine without inversion. Magnetotelluric profiling also shows consistency with model 3 by showing an increased conductivity in the east west direction consistent with the hypothesized graben location and a pattern suggesting vertical conductivity boundaries. These pieces of information suggest model 3 is valid.

2.5.4. Other notable features

A few results of interest were observed during data analysis. The first of these is from the analysis of the magnetotelluric data in the western part of the valley, particularly along the 2000 sites. Data from these sites suggests an east west feature where no significant anomaly in gravity is observed. Figure 2.40 shows the gravity residual, and site 2000 polar diagrams. Figure 2.41 shows the gravity and magnetotelluric models corresponding to locations along the red line in Figure 2.40. For the eastern part the models a similar structure is observed between gravity and magnetotellurics. The western most site shows a resistive layer from the xy component modelling. This layer is about 400m deep and is not apparent in the gravity model. The yx component shows the same layer at about 400m is conductive. The difference between the two models suggests an east trending two dimensional feature. Due to the lack of a gravity anomaly, we believe the anomalous magnetotelluric layer is related to fluids or hydrothermally altered materials. Another interesting feature observed in the gravity data is the anomalous east west trending gravity low in the south of the survey area at a northing of about 4445000. From Figure 2.40 this low approximately aligns with the ring faults. These two items may be of interest for further investigation.

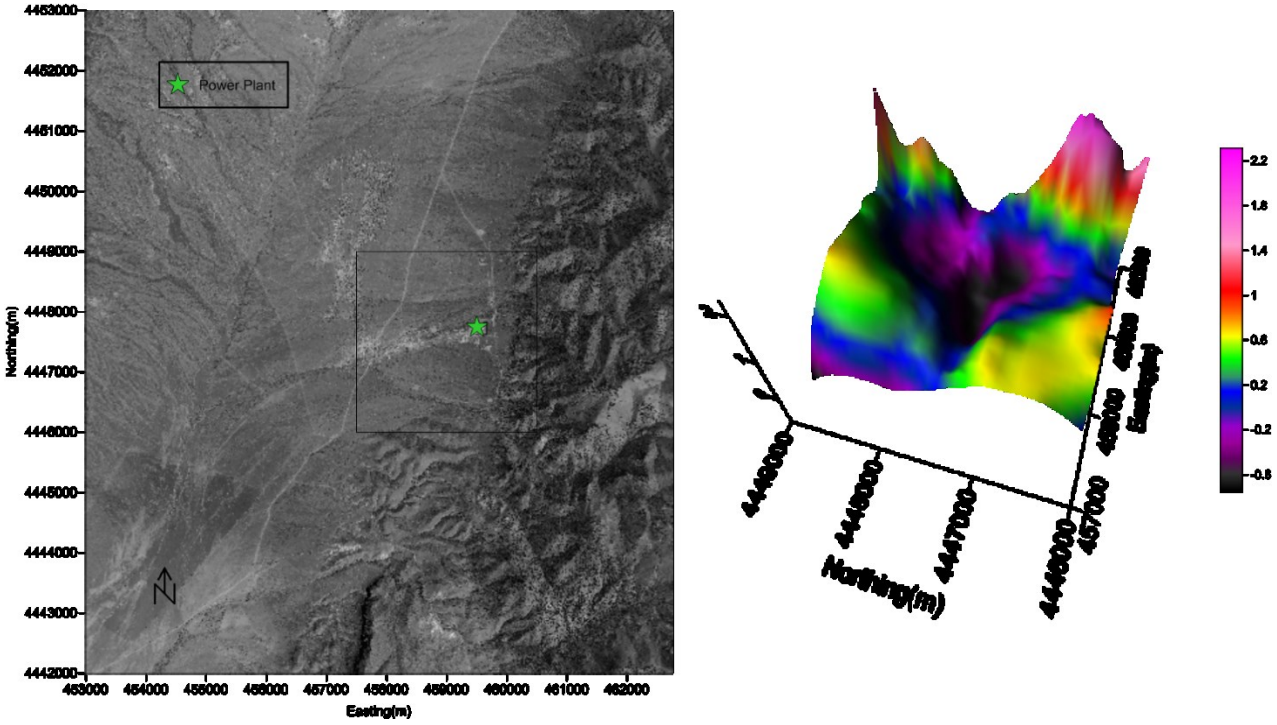

Figure 2.11. On the left hand side the rectangle indicates the area of the residual gravity plotted on the right hand side of the figure.

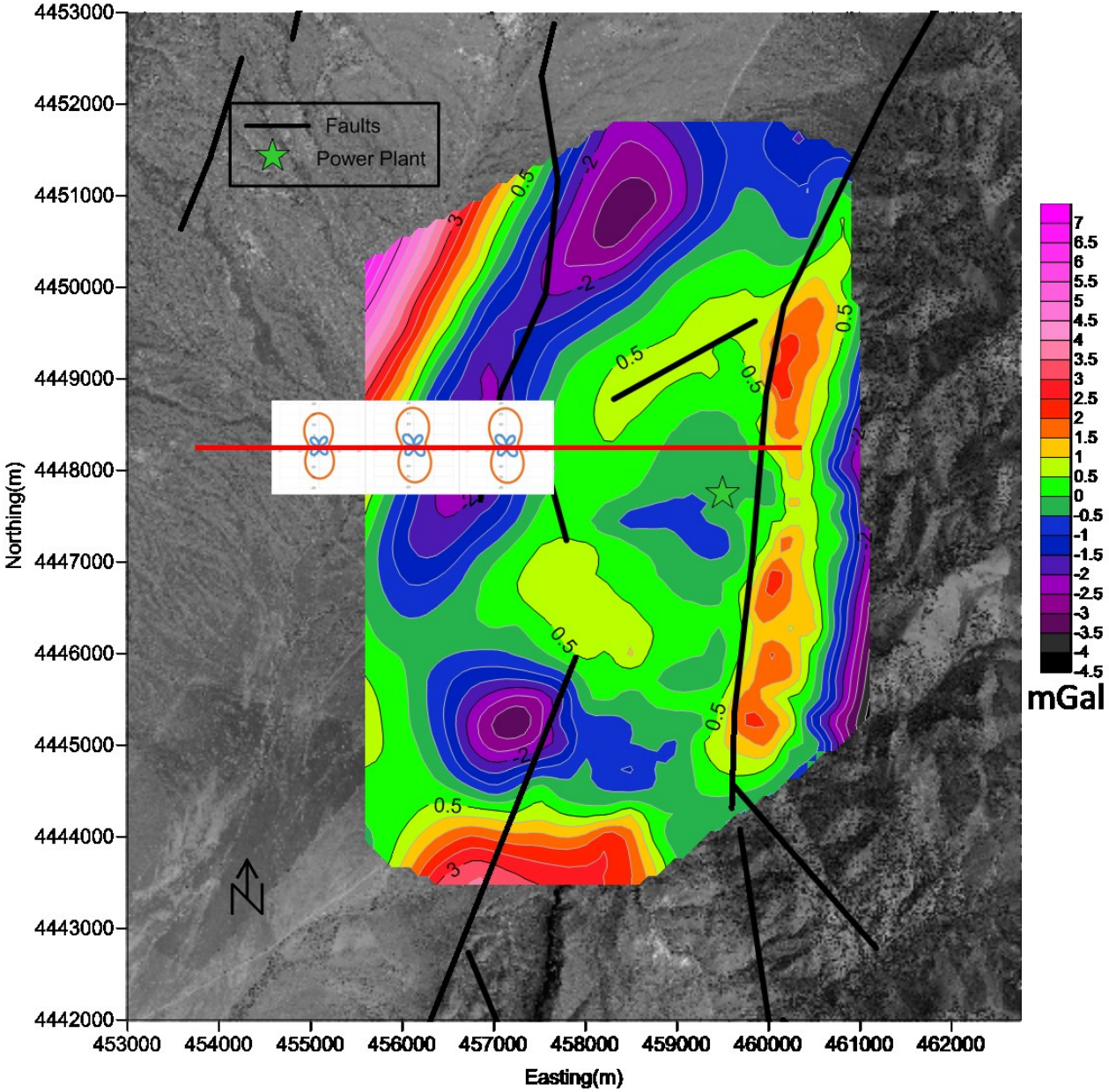

Figure 2.12. Combined residual gravity and polar diagrams for 2000 sites, faults included for interpretation purposes. The red line shows the location of the gravity model.

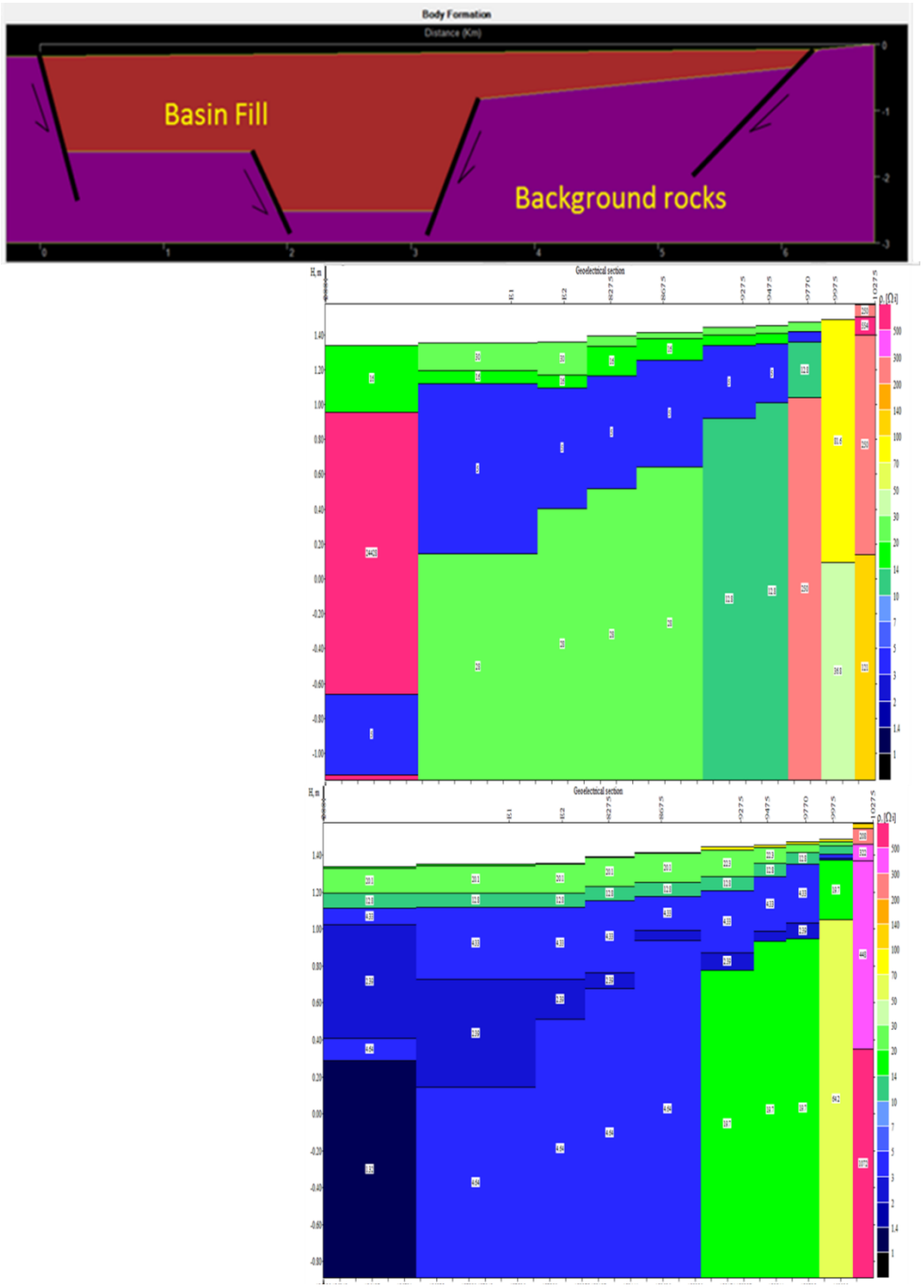

Figure 2.40. Two dimensional gravity and pseudo cross-sections from one dimensional magnetotelluric modelling. Models for location represented by the red line in Figure 2.41. Models are aligned in an east west fashion and also are scaled to similar depths. Top resistivity model is Rhoxy and bottom is Rhoyx.

Observations from both gravity and magnetotellurics suggest the Valley Fault trends more northeast than originally mapped. Figure 2.42 combines the gravity gradient data and polar diagram from site 10 and suggests a new fault trend via the dashed line for the Valley Fault. Interestingly the Fish Creek Range-front fault follows a similar trend.

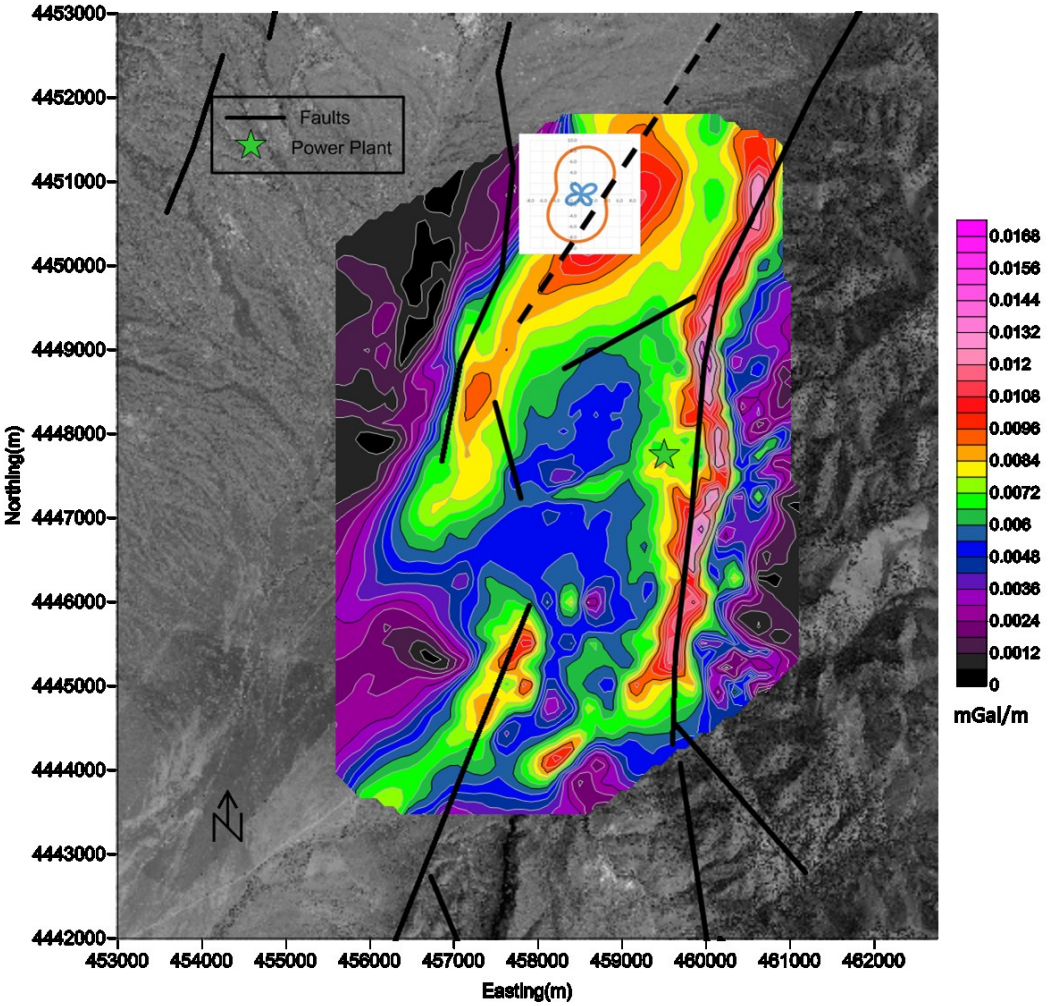

Figure 2.13. Gravity gradient map, with a site 10 polar diagram. Faults are plotted and a new fault trend for the Valley Fault is suggested as a the dashed line.

2.6. Conclusions

In this section, we summarize the results by presenting an adjusted fault map, and discuss what the results have shown about the initial structural models. we also discuss how the original objectives have been achieved.

2.6.1. Objectives

The objectives of this project as presented in section 1.5 are relisted: 1. Demonstrate the value of geophysical data in testing the models at Jersey Valley2. Show how geophysical data sets based on different physical properties can give information on the Jersey Valley models that is both complimentary and supplementary. 3. Test the currently available models at Jersey Valley.

We believe we have clearly achieved objective 1, this is discussed further in section 7.3 by showing structures from models 2 and 3 are consistent with geophysical data whereas structures from model 1 are not. The inconsistency of the data with model 1 clearly shows that information based on surface features alone may be insufficient to determine structure and the use of geophysics in determining subsurface properties is an important tool. We believe this justifies that future modelling should incorporate interpretation of geophysical data. Objective 2 was demonstrated through the use of magnetotelluric and gravity data sets. Magnetotellurics is sensitive to conductivity distribution and gravity to density distribution. Significant displacement of the Valley Fault shown through gravity maps and profile modelling was backed up by the one dimensional magnetotelluric modelling of sites 10 and B. Polar diagrams for site 10 and high gradients were consistent in remapping the Valley Fault trend. Magnetotelluric profiles perpendicular to the structure associated with model 3 support the gravity residual map. In contrast to these consistencies between the two data sets, magnetotelluric data and polar diagrams along the east trending transect from Figure 2.40 shows a clear conductivity anomaly where there is no obvious gravity anomaly. Objective 3 is clearly demonstrated in section 7.3 in which models 2 and 3 are shown to be consistent with the data, but model 1 is shown to be inconsistent with the data.

2.6.2. Interpreted fault map

Figure 2.42 shows an updated fault map based on the original map and adjusted as determined from the data. The range-front faults from the original map are consistent with the data. Based on these data, the Valley Fault trends more northeast than originally mapped. The data also suggests that two sets of east west faults exist that represent down-dropped blocks as marked in Figure 2.39. The data also suggests that a fault exists on the western side of the valley labelled as the Western Valley Fault. The structure of the valley faults, at their southern extent, is

ambiguous and deserve further investigation. This fault map should be considered an initial interpretation of the geophysical data which deserves further investigation.

2.6.3. Models

We have studied three starting models using the geophysical data sets, in particular we have examined the key structural components of these models. The results of the studies are combined and presented in Table 6.1.

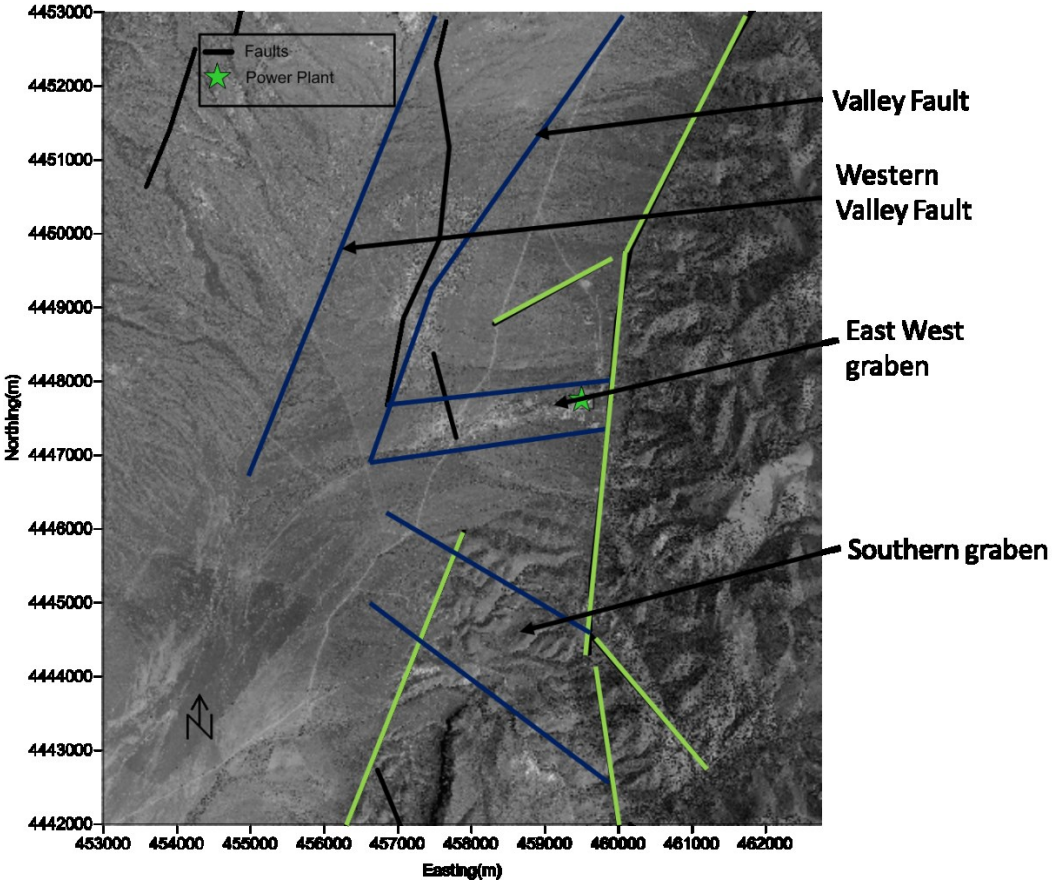

Figure 2.42. Adjusted fault map based on data, the green lines represent faults from the original fault map consistent with the data. The black lines are faults from the original fault map, and the blue lines represent hypothesized faults based on the geophysical data.

Table 6-1. Table of models and their supporting data, updated with information from both gravity and magnetotellurics.

Models	Key Elements	Supporting data	Notes	Supporting gravity data	Supporting magnetotelluric data
1	Relay ramp between Fish Creek Range-front Fault and Augusta Mountain Range-front Fault	Fault map DEM	Competing against model 2		
2	Significant displacement along the Valley Fault	Fault map	Competing against model 1	Residual gravity maps Total horizontal gradient map Profile modelling	One dimensional modelling of site 10 Polar diagram from site 10 One dimensional profile model
3	An east west fault, near the power plant	Surface sinter deposits	Can exist in conjunction with models 1 or 2	Total horizontal gradient and Residual maps	North trending profile plotting

From Table 6.1 some final comments can be made: (1) The key elements of structure from Model 1 are inconsistent with the data (2) The key elements of structure from models 2 and 3 are consistent with the data. This information only confirms some basic ideas of the models, but is of great value in the development of further models. A valuable next step would be the creation of more detailed cross sections throughout the valley and eventually a three dimensional model which can be tested against the data. Although information on structure is important, information on the fluid flow of the system is the next highly important issue to be addressed. A series of self-potential data were gathered in May 2015 in Jersey Valley. This along with the structure information are later used to help address the fluid flow.

3. Cited references

Axelsson, G., et al., The sustainability task of the international energy agency's geothermal implementing agreement. Proceedings World Geothermal Congress 2010. 2010.

Axelsson, G., and H. Franzson. "Geothermal drilling targets and well siting." Proceedings of the Short Course on Geothermal Development and Geothermal Wells, organized by UNU-GTP and LaGeo (2012).

Bahr, K., Geological noise in magnetotelluric data: a classification of distortion types. Physics of the Earth and Planetary Interiors 66.1 (1991): 24-38.

Bauer, P., The Gravity Geophysical Method, New Mexico Bereau of Geology & Mineral Resources. Web. December, 2013.

Benoit, D., Conceptual models of the Dixie Valley, Nevada geothermal field, Transactions-Geothermal Resources Council (1999): 505-512.

Berdichevsky, M. N., V. I. Dmitriev, and E. E. Pozdnjakova. On two-dimensional interpretation of magnetotelluric soundings. Geophysical Journal International 133.3 (1998): 585-606.

Berdichevsky, M. N., and V. I. Dmitriev. Models and methods of magnetotellurics. Springer Science & Business Media, 2010.

Blackwell, D. D., B. Golan, and D. Benoit. Thermal regime in the Dixie Valley geothermal system. Geothermal Resources Council Transactions 24 (2000): 223-228.

Bobatchev, A.. "IPI2win_MT - 1D magneto-telluric and frequency sounding curves interpretation." The laboratory of near-surface electrical prospecting, Web. September, 2013

Cagniard, L., Basic theory of the magneto-telluric method of geophysical prospecting. Geophysics, 18.3 (1953): 605-635.

Chave, A. D., and A. G. Jones, eds. The magnetotelluric method: Theory and practice. Cambridge University Press, 2012.

DiPippo, R.. Geothermal power plants: principles, applications, case studies and environmental impact. Butterworth-Heinemann, 2012.

Drakos, P., Spielman, P., Björnsson. Jersey Valley Exploration and Development., Trsactions – Geothermal resecrh Council(2011) Vol. 35, pp. 751-759.

Egbert, Gary D. "Robust multiple-station magnetotelluric data processing." Geophysical Journal International 130.2 (1997): 475-496.

Ellinghaus, A., PROCMT User's Guide.

Faulds, James E., et al. "Assessment of favorable structural settings of geothermal systems in the Great Basin, western USA." Geothermal Resources Council Transactions 35 (2011): 777-783.

Faulds, J. E., et al., Why is Nevada in hot water? Structural controls and tectonic model of geothermal systems in the northwestern Great Basin. Geothermal Resources Council Transactions 28 (2004): 649-654.

Fontes, S. L., et al., Processing of noisy magnetotelluric data using digital filters and additional data selection criteria. Physics of the earth and planetary interiors 52.1 (1988): 30-40.

Garcia, X., and A. G. Jones. "Decomposition of three-dimensional magnetotelluric data." Methods in Geochemistry and Geophysics 35 (2002): 235-250.

Geothermal Water Use in Nevada. Open EI. Web. September 2014

Grant, M.. Geothermal reservoir engineering. Elsevier, 2013.

Gonsior, Z.J. and Dilles, J.H., The Timing and Evolution of Cenozoic Extensional Normal Faulting and Magmatism in the Southern Tobin Range, Nevada: Geosphere (2008): Vol 4, Issue 4, p. 687-712.

Ledo, J., et al. Two-dimensional interpretation of three-dimensional magnetotelluric data: an example of limitations and resolution. Geophysical Journal International 150.1 (2002): 127-139.

Ledo, J.. 2-D versus 3-D magnetotelluric data interpretation. Surveys in Geophysics 26.5 (2005): 511-543.

Li, A.-Y., et al., Utilization of Effective Apparent Resistivity in Magnetotelluric Data Processing and Interpretation. Session 3AP: 571.

Mallick, K., and K. K. Sharma. "Computation of regional gravity anomaly—A novel approach." Proceedings of the Indian Academy of Sciences-Earth and Planetary Sciences 106.1-2 (1997): 55-59.

McKee, E. H. Fish, Creek Mountains Tuff and volcanic center, Lander County, Nevada. 1970.

Nabighian, Misac N.Lecture Mining Geophysics. Colorado School of Mines. Golden, Colorado, Fall 2012

Saemundsson, Kristján, Gudni Axelsson, and Benedikt Steingrímsson. "Geothermal systems in global perspective." ÍSOR—Iceland GeoSurvey, January (2011).

Schwering, P. C., and R. E. Karlin. "Structural Interpretation and Modeling of the Dixie Meadows Geothermal Prospect using Gravity and Magnetic Data." AGU Fall Meeting Abstracts. Vol. 1. 2012.

Shandini, Yves, and Jean Marie Tadjou. "Interpreting gravity anomalies in south Cameroon, central Africa." Earth Sciences Research Journal 16.1 (2012): 5-9.

Simpson, Fiona, and Karsten Bahr. Practical magnetotellurics. Cambridge University Press, 2005.

Talwani Ver. 2.2 for Windows. The University of Texas at El Paso. Web. December 2012.

Thurston, J. B., and R. James Brown. "The filtering characteristics of least-squares polynomial approximation for regional/residual separation." Can. Journal of Expl. Geophy, 28 (2) (1992): 71-80.

U. Matzander, M. Wilde. “ADU-07 Operating Manual”

Unsworth, M. “Theory of Magnetotellurics Over a 2-D Structure” Geophysics 424 Electromagnetic and potential field methods, University of Alberta, September 2014. Web. October 2014

Vozoff, K., Electromagnetic methods in applied geophysics. (1991): 641-711.

Vozoff, K.. "The magnetotelluric method in the exploration of sedimentary basins." Geophysics 37.1 (1972): 98-141.

4. Publications, Conference Papers, and Presentations:

Bold: PI and co-PI, underlined: students paid through the project.

Papers:

Revil A., M. Karaoulis, S. Srivastava, and S. Byrdina, Thermoelectric self-potential and resistivity data localize the burning front of underground coal fires, Geophysics, 78, 5, B259–B273, 2013.

Karaoulis M., A. Revil, A., J. Zhang, and D.D. Werkema, Time-lapse cross-gradient joint inversion of cross-well DC resistivity and seismic data: A numerical investigation, Geophysics, 77(4), D141–D157 doi: 10.1190/GEO2012-0011.1, 2012.

Karaoulis M., A. Revil, D.D., Werkema, P. Tsourlos, and B.J. Minsley, IP4DI: A software for time-lapse 2D/3D DC-resistivity and induced polarization tomography, Computers & Geosciences, 54, 164-170, 2013.

Revil A., A. Jardani, J. Hoopes, M. Karaoulis, C. Colwell, **M. Batzle**, A. Lamb, and K. van Wijk, Non-intrusive estimate of the flow rate of thermal water along tectonic faults in geothermal fields using the self-potential method, FastTIMES, 16(4), 2011.

Karaoulis M., A. Revil, B., Minsley M. Todesco, J. Zhang, and D.D. Werkema, Time-lapse gravity inversion with an active time constraint, Geophysical Journal International, 196, 748–759, doi:10.1093/gji/ggt408, 2014.

MacLennan, K., M. Karaoulis, and **A. Revil**, Complex conductivity tomography using low-frequency cross-well electromagnetic data, Geophysics, 79(1), E23-E38, doi: 10.1190/GEO2012-0531.1, 2014.

Byrdina S., D. Ramos, J. Vandemeulebrouck, P. Masias, **A. Revil**, A. Finizola, K. Gonzales Zuniga, V. Cruz, Y. Antayhua, and O. Macedo, Influence of the regional topography on the remote emplacement of hydrothermal systems with examples of Tiscani and Ubinas volcanoes, Southern Peru, Earth and Planetary Research Letters, 365, 152-164, 2013.

Soueid Ahmed, A., A. Jardani, **A. Revil**, and J.P. Dupont, SP2DINV: A 2D forward and inverse code for streaming-potential problems, Computers & Geosciences, 59, 9-16, 2013.

Karaoulis M., **A. Revil**, and D. Mao, Localization of a coal seam fire using combined self-potential and resistivity data, International Journal of Coal Geology, 128-129, 109-118, doi: 10.1016/j.coal.2014.04.011, 2014.

Zhou J., A. Revil, M. Karaoulis, D. Hale, J. Doetsch, and S. Cuttler, Image-guided inversion of electrical resistivity data, Geophysical Journal International, 197, 292-309, doi:10.1093/gji/ggu001, 2014.

Zhang J., and **A. Revil**, Cross-well 4-D resistivity tomography localizes the oil–water encroachment front during water flooding, Geophysical Journal International, 201, 343–354, doi: 10.1093/gji/ggv028, 2015.

Revil A., S. Cuttler, M. Karaoulis, J. Zhou, B. Raynolds, and **M. Batzle**, The plumbing system of the Pagosa thermal Springs, Colorado: Application of geologically-constrained geophysical inversion and data fusion, Journal of Volcanology and Geothermal Research, 299, 1-18, doi: 10.1016/j.jvolgeores.2015.04.005, 2015.

Zhang J., and **A. Revil**, 2D Joint inversion of geophysical data using petrophysical clustering and facies deformation, Geophysics, 80(5), M69-M88, doi: 10.1190GEO2015-0147.1, 2015.

Zhou J., A. Revil, and A. Jardani, Stochastic structure-constrained image-guided inversion of geophysical data, Geophysics, 81(2), E51-E63, doi: 10.1190/GEO2014-0569.1, 2016.

Presentations

A. Revil, K. Richards, and **M. Batzle**, Using geophysical techniques to characterize fluid flow in a geothermal reservoir, The Colorado Geothermal Symposium, invited talk, January 18-19th, 2010, Golden, Colorado, USA.

Lamb A.P., K. van Wijk, L. Liberty, **A. Revil**, K. Richards, and **M. Batzle**, Preliminary results for a near surface 3D seismic survey of a geothermal system in Colorado, Poster NS3-7, session NS 3 "Methodological Studies and Appications" (10/21/2010), SEG (Society of Exploration Geophycists) Annual Meeting "Imaging our Future", 17-22 October 2010, Denver, CO, USA.

A. Lamb; K. Van Wijk; L. M. Liberty; **A. Revil**; **M. L. Batzle**, GP41A-0981. Investigating the Structure of a Shallow Geothermal System in the Upper Arkansas Valley of Colorado, Using a Combination of Potential Field and Seismic Geophysical Data, GP41A. Crustal Imaging With Potential Fields: Applications to Tectonics, Hazards, and Resources III Posters, Thursday december 8th. 2011 Fall Meeting, AGU, 5-9 Dec. 2011, San Francisco, CA, USA.

Revil A., M. Batzle, and **E. Zemach**, Time-lapse Joint Inversion of Geophysical Data and its Application to Geothermal Prospecting, Geothermal Technologies Program 2012 Peer Review, 9th May 2012, Denver, CO,.

Other Products / Deliverables:

All reports should be written for public disclosure. Reports should not contain any proprietary or classified information, other information not subject to release, or any information subject to export control classification. If a report contains such information, notify DOE within the report itself.

Softwares: A resistivity inversion software has been published in Computers & Geoscience. This software is available free of charge to the community via the web site of this journal. Another software on the inversion of self-potential data is also published in the same journal with the manuscript " Soueid Ahmed, A., A. Jardani, A. Revil, and J.P. Dupont, SP2DINV: A 2D forward and inverse code for self-potential problems, Computers & Geosciences, 2012".